

DISSERTATION

SYNTHESIS, PROPERTIES, AND SUITABILITY OF VARIOUS OXYMETHYLENE ETHERS FOR
COMPRESSION IGNITION FUELS

Submitted by

Stephen P. Lucas

Department of Mechanical Engineering

In partial fulfillment of the requirements

For the Degree of Doctor of Philosophy

Colorado State University

Fort Collins, Colorado

Summer 2023

Doctoral Committee:

Advisor: Bret Windom

Thomas Foust

Kenneth Reardon

Anthony J. Marchese

Copyright by Stephen P. Lucas 2023

All Rights Reserved

ABSTRACT

SYNTHESIS, PROPERTIES, AND SUITABILITY OF VARIOUS OXYMETHYLENE ETHERS FOR COMPRESSION IGNITION FUELS

Compression ignition (CI) engines are currently the most common prime mover for medium and heavy duty vehicles; these engines contribute roughly a quarter of US greenhouse gas emissions from transportation, and even higher percentages of particulate and nitrogen oxide emissions. As a result, there have been significant efforts made to reduce these emissions, particularly through selection of low-emissions alternative fuels.

Oxymethylene ethers (OMEs) are a class of molecule, typically structured $R-O-(CH_2O)_n-R'$, which have been considered as a possible blendstock in CI fuels for the goal of soot reduction. Generally, past work has focused on methyl-terminated OMEs, $CH_3-O-(CH_2O)_n-CH_3$, which by virtue of containing no C–C bonds, produce negligible soot. These molecules show significant reductions in soot emission from engines when blended in moderate to high ratios with traditional diesels, however, they have been shown to have inferior physical properties and poor compatibility with some legacy systems. Recent theoretical work has shown that OMEs with non-methyl alkyl groups may have superior performance, albeit at the cost of increased soot formation.

In this work, a variety of OMEs with terminating alkyl groups from methyl to butyl are considered for their suitability as CI fuels. The synthesis of these extended OMEs is studied, including formation of $n=1$ OMEs from common chemical sources, and extension of the chain length to heavier molecules, via reactions over acidic ion exchange resins. Following the synthesis, the properties of these OMEs are studied with respect to their engine applicability. It is found that heavier (propyl- and butyl-terminated) OMEs have superior properties for diesel compatibility, particularly in reactivity, volatility, and water solubility. Extended-alkyl OMEs are found to have higher soot production than methyl-terminated OMEs, but remain superior to diesel soot

production on a per-unit-energy basis. A sample of a butyl-terminated OME mixture, $n=2-4$, is selected as the ideal OME blend for close compatibility with legacy diesel systems. This mixture is blended with certified diesel and tested for ASTM D975 compatibility, passing all required tests but lubricity; decreased heat of combustion is observed but not governed by the diesel standard. Fundamental combustion tests of various mid-weight OMEs are performed in a rapid compression machine, where it is shown that low-temperature chemistry causes a region of decreased dependence of ignition delay on temperature, consistent with methyl-terminated OME behavior. An isopropyl-terminated OME is observed to have low reactivity compared to other OMEs; this fuel is investigated via further rapid compression machine testing and CFR engine testing. It is found that this OME has strong negative-temperature-coefficient ignition behavior – a first for OMEs – and has reactivity lower than other OMEs, but insufficient for direct spark ignition engine testing.

ACKNOWLEDGEMENTS

I would like to thank my advisor and committee for the support and opportunity to pursue this research. Additionally, I am grateful for the work of several undergraduate interns, namely Alayna Gilbert, Justine Serdoncillo, Will McBryde, and Wyatt Wolff, whose assistance with lab work has greatly accelerated the progress of this work. Further, none of this work would have been possible without collaborators at CSU – Andrew Zdanowicz, Garrett Cole, and Jason Quinn – and other institutions: Junqing Zhu and Charles McEnally of Yale, Nicole J. Labbe of University of Colorado, and Jon Luecke, Gina Fioroni, and Martha Arellano-Treviño of the National Renewable Energy Laboratory.

The majority of this research is funded through the U.S. Department of Energy’s Office of Energy Efficiency and Renewable Energy under the Bioenergy Technologies Office, Co-Optimization of Fuels and Engines Initiative (Co-Optima) award number DE-EE0008726, with additional financial support from the Colorado Energy Research Collaboratory. Portions of this dissertation have been previously published in journals managed by Elsevier and ACS Publications; use of published work by the author in their dissertation is explicitly permitted in the journals’ reuse policies.

DEDICATION

I dedicate this work to the memory of my late grandfather, Dr. J. Arthur Keith, the first in my family to earn a doctorate degree, and whose example I strive to follow (except for that whole cut once, then measure twice, and then have to cut again thing in your woodshop - that's a bad idea). You will always be missed.

TABLE OF CONTENTS

ABSTRACT	ii
ACKNOWLEDGEMENTS	iv
DEDICATION	v
LIST OF TABLES	viii
LIST OF FIGURES	ix
Chapter 1 Introduction	1
1.1 Nomenclature	1
1.2 Motivation	3
1.3 Literature Review	5
1.3.1 Synthesis of OMEs	5
1.3.2 Physical and Chemical Properties of OMEs	9
1.3.3 Combustion and Engine Performance of OMEs	10
1.4 Objectives and Structure of Research	14
Chapter 2 Synthesis of New Extended-Alkyl and Extended-Chain OMEs	16
2.1 Synthesis of Butyl-Terminated Oxymethylene Ethers	16
2.1.1 Methods	16
2.1.2 Results and Discussion	20
2.2 Synthesis and Chain Growth of Other OMEs	33
2.2.1 Method of Production of X-1-X OMEs	33
2.2.2 Methods for Chain Growth of OMEs	37
2.2.3 Results	37
Chapter 3 Determination of Fuel-Relevant Properties of OMEs	41
3.1 Methods	41
3.1.1 Fuels Used	41
3.1.2 Testing Methods	41
3.2 Results and Discussion	45
3.2.1 Indicated Cetane Number	45
3.2.2 Lower Heating Value	47
3.2.3 Yield Sooting Index	49
3.2.4 Flash Point	52
3.2.5 Density and Viscosity	53
3.2.6 Vapor Pressure	55
3.2.7 Oxidative Stability	59
3.2.8 Water Solubility	61
3.2.9 Boiling Temperature	62
3.2.10 Material Compatibility	63
3.3 Downselected Blend and Diesel Compatibility	66
3.3.1 ASTM Diesel Standard Compatibility	66

3.3.2	Diesel-Blend Engine Compatibility	72
Chapter 4	Combustion and Engine Behavior of Various OMEs	76
4.1	Methods	76
4.1.1	Rapid Compression Machine	76
4.1.2	Cooperative Fuels Research Engine	79
4.1.3	Analysis Methods	81
4.2	Pre-Vaporized Ignition of E-1-E, E-2-E, P-1-P, and iP-1-iP	88
4.2.1	Candidate Fuels & Chemical Preparation	88
4.2.2	Results	90
4.3	iP-1-iP as a Spark Ignition Fuel	98
4.3.1	RCM Autoignition	99
4.3.2	RCM Spark Ignition	102
4.3.3	CFR Engine	107
4.3.4	Chemical Origins of iP-1-iP NTC	112
Chapter 5	Conclusions	114
5.1	Summary of Findings	114
5.2	Limitations and Areas for Future Work	118
5.3	Recommendations for OME Selection	119
References	121
Appendix A	List of Chemicals Used	139
Appendix B	Operation of the B/R Instruments Spinning Band Distillation Column	141

LIST OF TABLES

1.1	List of symbols and abbreviations	1
1.1	List of symbols and abbreviations	2
1.1	List of symbols and abbreviations	3
2.1	Properties of ion-exchange resin catalysts used in this study	19
2.2	Pathway 1 rate and equilibrium constants for tested catalysts at 60°C, where $K_{n,eq} = k_n/k_{-n}$	29
2.3	Pathway 1 rate and equilibrium constants for Amberlyst 15 at different temperatures, $K_{n,eq} = k_n/k_{-n}$	30
2.4	Pathway 2 rate and equilibrium constants for Amberlyst 15 at different temperatures, including B-2-B in analysis, $K_{n,eq} = k_n/k_{-n}$	31
2.5	Mass and molar yields of iP-1-iP production reaction at 80°C and 0.64 min ⁻¹ space velocity over Amberlyst 15 acid catalyst	36
3.1	Indicated Cetane Number of various OMEs	45
3.2	Lower Heating Value of various OMEs [MJ/kg]	48
3.3	Yield Sooting Index of various OMEs	50
3.4	YSI/LHV of various OMEs [1/(MJ/kg)]	50
3.5	Flash Point of various OMEs [°C]	52
3.6	Density at 20°C of various OMEs [g/mL]	53
3.7	Kinematic Viscosity at 40°C of various OMEs [mm ² /s]	54
3.8	Antoine equation coefficients for some OMEs [bar, K]	58
3.9	Induction times of select OMEs in Petro-Oxy test, 20 vol% in tridecane	60
3.10	Water solubility of various OMEs [g OME / kg water]	61
3.11	Boiling temperature of various OMEs [°C]	63
3.12	Properties controlled and limits under ASTM D975 [110], using ULSD 2-D as reference 67	
4.1	Flame speeds and density ratios at 15 bar TDC pressure as calculated for all tests (n/a indicates aspheric flames which could not be processed for speed).	105
4.2	Comparison of knock effects on iP-1-iP compared to iC8 at similar conditions.	105
4.3	Octane number of iP-1-iP and 85 vol% iP-1-iP / 15 vol% iPrOH (iP-1-iP/85), expected accuracy ±0.5 ON, except iP-1-iP RON, which was not a stable combustion condition and RON could not be accurately identified.	107
A.1	Chemicals used in this research	139

LIST OF FIGURES

1.1	Example OME structure for B-2-B showing general layout of OMEs.	3
1.2	M-1-M, the simplest OME	5
1.3	M-n-M, the oligomerization of M-1-M	8
2.1	Parr reactor used for this work	17
2.2	Butoxymethoxymethane – intermediate product, formed via (R2.1.1)	20
2.3	Dibutoxymethane – target product, formed via (R2.1.2) or (R2.2.2)	20
2.4	B-2-B – oligomerized product, formed via (R2.2.3)	21
2.5	Mole fraction yield of butoxymethoxymethane at 60°C and 0.5 mass % catalyst, 2 mol butanol : 1 mol dimethoxymethane	22
2.6	Mole fraction yield of dibutoxymethane at 60°C and 0.5 mass % catalyst, 2 mol butanol : 1 mol dimethoxymethane	22
2.7	Pathway 1 mole fraction yield of M-1-B with 0.5 mass % Amberlyst 15, 2 mol butanol : 1 mol dimethoxymethane	24
2.8	Pathway 1 mole fraction yield of B-1-B with 0.5 mass % Amberlyst 15, 2 mol butanol : 1 mol dimethoxymethane	24
2.9	Pathway 2 mole fraction yields of B-1-B with 0.5 mass % Amberlyst 15, 2 mol butanol : 1 mol formaldehyde (6 mol butanol : 1 mol trioxane). B-2-B was present in small (<2 mol% after 24 hours) concentrations for 80°C and 100°C tests.	26
2.10	ODE optimization of Pathway 1 kinetic parameters at 60°C using pseudo-homogeneous model, accounting for all components. Solid lines indicate P-H model, symbols with dotted lines are experimental data.	29
2.11	ODE optimization of Pathway 1 kinetic parameters at 60°C using pseudo-homogeneous model, accounting for only M-1-B and B-1-B formation in the optimization process.	30
2.12	ODE45 optimization solution to P-H model for Pathway 2 at 80°C, including B-2-B in calculations	31
2.13	Flow reactor setup	34
2.14	iP-1-iP synthesis method, as a representative of the full process required to synthesize and isolate an OME from alcohol and trioxane	35
2.15	B/R Instruments 36/100 spinning band distillation column	35
2.16	Oligomerization yield of 3 mol E-1-E : 1 mol trioxane over Amberlyst 15, 70°C, 8 mL/min	38
2.17	Oligomerization yield of 3 mol P-1-P : 1 mol trioxane over Amberlyst 15, 80°C, 8 mL/min	39
2.18	Oligomerization yield of 3 mol B-1-B : 1 mol trioxane over Amberlyst 15, 80°C, 8 mL/min	39
2.19	Typical D975 distillation curves with boiling points of some B-n-B compounds (see Chapter 3; B-4-B is estimated from trend)	40
2.20	Composition of 200-305°C cut of B-n-B oligomerization products	40
3.1	Effect of varying B-1-B blending ratio in diesel (ICN=40.7) on ICN of mixture, compared with a linear blending assumption.	47

3.2	Viscosity and density curves of M-n-M OMEs between 20°C and 100°C	55
3.3	Viscosity and density curves of E-n-E OMEs between 20°C and 100°C	56
3.4	Viscosity and density curves of P-n-P and iP-1-iP OMEs between 20°C and 100°C	56
3.5	Viscosity and density curves of B-n-B and iB-1-iB OMEs between 20°C and 100°C	57
3.6	Antoine curves of OME vapor pressure, from calculated Antoine coefficients, compared to some typical alkanes (see Table 3.8)	58
3.7	Test setup for material compatibility exposure testing	64
3.8	Percent change in mass of elastomer sample coupons after 24hr submerged exposure	65
3.9	Percent change in mass of elastomer sample coupons after 72hr submerged exposure	66
3.10	Discoloration of iP-1-iP due to NBR leaching	67
3.11	B-n-B in diesel sample kept six months for phase separation test	68
3.12	FOI Laboratories Test Reports	69
3.12	FOI Laboratories Test Reports	70
3.12	FOI Laboratories Test Reports	71
3.13	Deere 4045 4.5L Tier 3 diesel engine used in this testing	72
3.14	PM/NO _x tradeoff for OMEs vs ULSD	73
3.15	PM emissions from Deere 4.5L engine testing	73
3.16	Combustion timing of Deere 4.5L with ULSD and OMEs	74
3.17	Engine performance of Deere 4.5L with ULSD and OMEs	74
3.18	Other emissions of Deere 4.5L with ULSD and OMEs	74
4.1	RCM system schematic	78
4.2	Schlieren optical schematic	79
4.3	Representative Schlieren images of flamefront at 1, 10, and 100 frames (0.024, 0.24, and 2.4 ms) after the laser spark, from stoichiometric iP-1-iP in N ₂	80
4.4	CSU CFR Engine	81
4.5	Example algorithm for solving IDT with a low dp/dt . <i>Line A</i> : Filtered pressure trace. <i>Line B</i> : Gradient of pressure. <i>Line C</i> : Tangent to pressure at maximum gradient (primary event). <i>Line D</i> : Tangent to pressure at maximum gradient (first stage event). <i>Line E</i> : Tangent to local minimum pressure (between first and primary event). <i>Line F</i> : Tangent to local minimum pressure (between TDC and first event). <i>Line G</i> : Non-reactive pressure curve, calculated from double-exponential function fitted to normalized and scaled average of three nonreactive pressure traces for the appropriate gas mixture. <i>Point H</i> : Intersection of Line C and Line E. Defines primary ignition delay. <i>Point I</i> : Intersection of Line D and Line F. Defines first stage ignition delay. For single-stage ignition, lines D and F and point I are not calculated, and Line E occurs between TDC and primary ignition.	83
4.6	Measured flame propagation rates for a sample DIPM flame.	84
4.7	Representative Schlieren images of flamefronts where the calculator effectively and ineffectively identifies the flamefront, and where interference from piston face turbulence cannot be separated from the flame. From stoichiometric DIPM in N ₂	85
4.8	Knock indication in AHRR trace from a high temperature iP-1-iP sample SI test	86
4.9	No knock indication in AHRR trace from a high temperature iC8 sample SI test	87
4.10	OME Structures: Red greek letter indicate carbon labels. Blue numbers indicate bond dissociation energies in kcal/mol from [127–129]	89

4.11	Pressure traces for representative tests at 700K and 20 bar compressed pressure, $\Phi=1.0$, 12:1 inert:O ₂ . (note that pressure offsets have been applied to prevent overlap)	90
4.12	Calculated primary IDT of linear OMEs at 20 bar compressed pressure, $\Phi=1.0$, 12:1 inert:O ₂	91
4.13	Calculated primary IDT of E-1-E with various mechanisms of nC7 and OMEs at 20 bar compressed pressure, $\Phi=1.0$, 12:1 inert:O ₂ [44, 46, 47, 119, 131]	91
4.14	Calculated first stage IDT of linear OMEs at 20 bar compressed pressure, $\Phi=1.0$, 12:1 inert:O ₂	92
4.15	Calculated IDT of iP-1-iP at 30 bar compressed pressure, $\Phi=1.0$, 12:1 inert:O ₂ compared with P-1-P at 20 bar and simulation of iC8 via LLNL v3.0 mechanism [132]	92
4.16	IDT of iC8 and iP-1-iP at 20 bar compressed pressure, $\Phi=1.0$, 5:1 inert:O ₂ .	99
4.17	IDT of isooctane, iP-1-iP, and 50 mol% and 75 mol% iP-1-iP/iPrOH blends in 5:1 nitrogen / oxygen gas mix.	102
4.18	Sample pressure traces of isooctane, iP-1-iP, and 50 mol% and 75 mol% iP-1-iP/iPrOH blends in 5:1 nitrogen / oxygen gas mix. Noise at the base of the ignition event pressure rise is a filter artifact and is not present in the measured traces.	103
4.19	Aspheric flame from low temperature / low flame speed - 300 frames / 7.14 ms after spark	104
4.20	Comparison of unburned gas flame speeds of isooctane and iP-1-iP at engine-relevant temperatures, P = 15 bar, $\Phi = 1.0$. Square markers indicate Kelley stretch correction calculations, while circular markers indicate linear stretch correction.	104
4.21	Representative Schlieren images of flamefronts 3 ms after spark, showing flame wrinkling at various conditions.	106
4.22	iP-1-iP sample cycles from CFR tests	108
4.23	KI comparison across 200 cycles for different CFR tests	110
4.24	KI comparison across 200 cycles for different CFR tests	111

Chapter 1

Introduction

1.1 Nomenclature

Numerous shorthands, abbreviations, and symbols will be used throughout this text. A listing of these is provided in Table 1.1.

Table 1.1: List of symbols and abbreviations

Symbol / Abbreviation	Meaning
γ	Specific heat ratio
λ	Equivalence ratio
ν	Kinematic viscosity
ρ	Density
ACS	American Chemical Society
AFIDA	Advanced Fuel Ignition Delay Analyzer
ASTM	American Society for Testing and Materials
BP	Boiling Point
CFR	Cooperative Fuels Research
CI	Compression Ignition
CN	Cetane Number
Co-Optima	Co-Optimization of Fuels and Engines Initiative
CR	Compression Ratio
CSU	Colorado State University
CVCC	Constant Volume Combustion Chamber
DCN	Derived Cetane Number
DoD	United States Department of Defense
DoE	United States Department of Energy

Table 1.1: List of symbols and abbreviations

Symbol / Abbreviation	Meaning
EC	Elemental Carbon
EGAI	End Gas Autoignition
FA	Formaldehyde
FIT	Fuel Ignition Tester
FP	Flash Point
GC-FID	Gas Chromatograph - Flame Ionization Detector
GHG	Greenhouse Gas
HHV	Higher Heating Value
ICE	Internal Combustion Engine
ICN	Indicated Cetane Number
IDT	Ignition Delay Time
KI	Knock Index
LHV	Lower Heating Value
MON	Motor Octane Number
NO _x	Nitrogen Oxides
NREL	United States National Renewable Energy Laboratory
OC	Organic Carbon
OME	Oxymethylene Ether
ON	Octane Number
P-H	Pseudo-Homogeneous
PM	Particulate Matter
PRF	Primary Reference Fuel
RCM	Rapid Compression Machine
RON	Research Octane Number
SAF	Sustainable Aviation Fuel

Table 1.1: List of symbols and abbreviations

Symbol / Abbreviation	Meaning
SI	Spark Ignition
THC	Total Hydrocarbons
TXN	1,3,5-Trioxane
ULSD	Ultra-Low-Sulfur Diesel
WS	Water Solubility
YSI	Yield Sooting Index

The fuels of primary interest in this thesis are Oxymethylene Ethers (OMEs). These OMEs will be referred to using the shorthand $X-n-Y$, where X and Y are abbreviations for the terminating alkyl groups (M = methyl, E = ethyl, P = propyl, B = butyl, iP = iso-propyl, and iB = iso-butyl), and n is the number of oxymethylene units in the molecule (note that the number of oxygen atoms will be $n+1$). An example structure, for B-2-B, is provided in Figure 1.1. This shows a linear OME with symmetric end groups, however, some OMEs studies have asymmetric end groups (e.g. M-1-B) or have branched structures (e.g. iP -1- iP).

1.2 Motivation

Combustion has been a primary source of energy for humanity for thousands of years; in the past centuries, rapid advances were made allowing combustion to go from a simple heat source to a method of powering machinery and transforming thermal energy into other useful forms, e.g. mechanical work, electrical power, etc. With the advent of external combustion steam

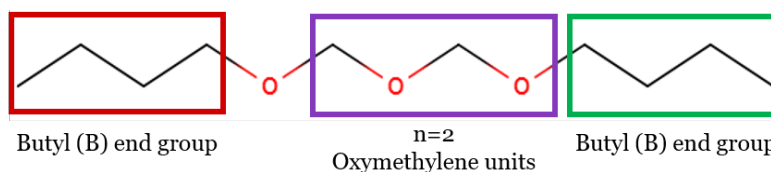


Figure 1.1: Example OME structure for B-2-B showing general layout of OMEs.

engines in the 1700s, the external combustion engine became a viable method for powering industrial facilities, kick-starting the industrial revolution. Further development occurred later [1], starting with J. J. E. Lenoir's uncompressed internal combustion engine (ICE) - the first commercially successful ICE ever designed. In 1876, a significant advancement was made with N. A. Otto's first prototype of a four-stroke engine with a compressed charge, and this concept was refined in coming years to become the spark ignition (SI) engines common across the world in gasoline vehicles and lightweight machinery. In 1892, R. Diesel patented a combustion concept which allowed major improvements in efficiency and compression ratio of ICEs by injecting fuel into a high-temperature, high-pressure air charge at the end of compression. This concept, now referred to as a compression ignition (CI) engine, took years to develop into a functional model [1], and more than a century later, is the primary powertrain for medium and heavy duty vehicles globally, as well as serving in power generation, rail, and marine applications.

CI engines are the prime mover for many medium duty vehicles, and nearly all heavy duty vehicles. For example, CI engines drive the majority of road-based freight, accounting for more than 80% of oil use in this sector, and collectively road freight alone accounts for half of global diesel fuel consumption [2]. This high fuel usage has serious environmental costs; in the US, medium and heavy duty vehicles accounted for roughly quarter of annual greenhouse gas (GHG) and half of the nitrogen oxide (NO_x) and particulate matter (PM) emissions [3]. Globally, there are a number of regulatory schemes to reduce the impact of emissions from CI engines; of major importance are the United States Tier 3 emissions standards and the European Tier 1-6/I-VI standards, which are adopted throughout Europe and India at Tier 6/VI and in many Asian and Latin American countries at other levels from 2/II to 5/V. In fact, 17 of the G-20 nations follow some level of Euro standards for emissions [4].

In support of these regulatory efforts, there have been major efforts to improve both fuels and engine systems to improve efficiency and reduce emissions. In the United States, the Department of Energy's Co-Optimization of Fuels and Engines Initiative (Co-Optima) seeks to "investigate fuels and engines as dynamic design variables that can work together to boost ef-

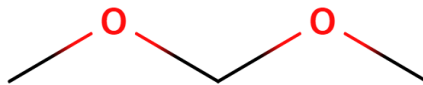


Figure 1.2: M-1-M, the simplest OME

efficiency and performance, while minimizing emissions.” Under this initiative, Colorado State partnered with the National Renewable Energy Laboratory and numerous other universities to investigate the possibilities of using upgraded versions of OMEs to significantly reduce PM emissions without the weaknesses found in prior studies of OMEs for CI fuel usage. As will be discussed in depth in Section 1.3, OMEs have been studied in detail and have seen significant interest in the past decade, however, it has been found that the most commonly studied OMEs – methyl-terminated OMEs with $n=3-6$ – there is a large loss in specific energy, as well as difficulties in fuel handling (high water solubility, seal material damage, etc.), and large variance in reactivity with varying n . We seek to remedy these challenges by determining the ideal OME characteristics to balance the PM reduction potential with improved compatibility with existing CI engines and fuel processing and handling infrastructure.

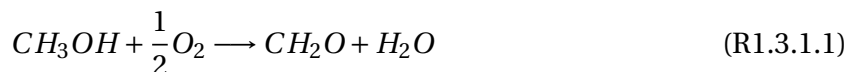
1.3 Literature Review

The literature review will be divided into three subsections concerning the synthesis process for OMEs at both the laboratory and industrial scales (Section 1.3.1), the fuel-relevant physical and chemical properties of OMEs (Section 1.3.2), and the performance of OMEs in engines and combustion processes (Section 1.3.3). This structure will mirror the results and discussion chapters to follow.

1.3.1 Synthesis of OMEs

The simplest possible oxymethylene ether is dimethoxymethane (M-1-M), shown in Figure 1.2. Several methods are discussed in the literature for synthesis of M-1-M. The primary industrial method is a two step process from methanol, first via partial oxidation of methanol

to formaldehyde, and then via acetalization of methanol with the formaldehyde from the prior process [5–7]. This is described in the reaction mechanism below from [5], where R1.3.1.4 is the overall reaction producing M-1-M:



In this reaction mechanism, the formation of the hemiformal (R1.3.1.2) can proceed in a neutral environment and monomeric formaldehyde is present in very low amounts at equilibrium, but the formation of M-1-M requires an acidic catalyst to proceed and is rate limiting [8].

As reviewed by Thavornprasert et al. [9], the first step of this process typically occurs as a gas-phase process over metallic catalysts, such as silver or iron-molybdenum oxides. For silver catalysts, formaldehyde may be produced at up to 89% yield at temperatures up to 600°C using methanol-rich feedstock; this process typically involves multiple passes, where unreacted methanol is recycled into the reaction system with a per-pass yield between 65-75%. Iron-molybdenum oxide catalysts operate at lower temperature and methanol concentration to prevent side reactions creating other ethers. These iron-moly catalysts must use methanol at less than 7% by volume, as there are explosion risks between 7-35%. At temperatures above 400°C, methanol may instead dehydrate to dimethyl ether. Also requiring multiple passes, iron-molybdenum oxide catalysts may offer up to 95% formaldehyde yield with 98% conversion of methanol. Due to the high yields, combined with longer lifetimes of up to a year, and lower contamination sensitivity, iron-molybdenum catalysts may be preferable for formaldehyde production.

After formaldehyde is produced, this is reacted again with methanol, this time in a liquid phase in an acidic environment [5, 9]. Schmitz et al. study the reaction kinetics and chemical equilibrium of these reactions in acidic environments [10, 11]. It is shown that this acetalization reaction is reversible, resulting in slow conversion and a limited theoretical maximum yield of M-1-M. Further, isolation of M-1-M can be complicated by an azeotrope of 92.2% M-1-M and 7.8% methanol [12]. The typical batch process for production of M-1-M is limited in its ability to produce high concentrations of the desired product; Oestreich et al. [8] find that the M-1-M yield is only slightly temperature dependent, and as the presence of formaldehyde in an acidic solution with M-1-M will also cause oligomerization to form M-n-M, is limited thermodynamically to approximately 16 mass%, with a total 37 mass% of all M-n-M. Multiple ion exchange resins were tested, with only minor changes in equilibrium yield of various OMEs, present primarily in M-1-M yield. Rate dependence on temperature is more significant, with a 20x reduction in time to equilibrium with an increase in reaction temperature from 40°C to 120°C. The catalytic distillation of Zhang et al. [12] allows for an improvement in conversion and prevents oligomerization due to removal of M-1-M as it is formed; thus, they observed greater than 91 mass% M-1-M in the distillate and nearly complete formaldehyde conversion for molar ratios greater than 2.2 methanol : formaldehyde.

An additional mechanism for production of M-1-M is via selective catalytic oxidation of methanol. This process requires a bifunctional catalyst that can perform the full reaction mechanism above in a single system. Thravornprasert et al. provides a detailed review of work on development of catalysts that can oxidize methanol, and in some cases dimethyl ether, to M-1-M [9]. Heteropolyacid catalysts were shown to provide moderate selectivity to M-1-M (up to 58%) with high conversion of methanol. Ruthenium oxide catalysts provided varying performance depending on the supporting oxide; silica and alumina provided the highest selectivity to M-1-M but with moderate conversion of methanol [13]. Rhenium oxides provide some of the highest observed conversion and selectivity to M-1-M at approximately 85% simultaneously, and vanadium oxides have been extremely well studied and can provide very high selectivity to M-1-M

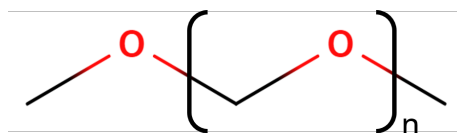


Figure 1.3: M-n-M, the oligomerization of M-1-M

(>90% in many cases), but typically with lower conversion of methanol [9]. Many of these catalysts require precious metal components; however, recent work by researchers at NREL has shown good selectivity with copper based catalysts, achieving 40% of possible thermodynamic equilibrium and high possible mass-throughput rates [14].

M-1-M has been used as a diesel additive on its own [15–25], but has some properties, particularly its cetane number, which are less than ideal for use as a diesel additive (this will be discussed in more detail in Section 1.3.2). Thus, it is necessary to oligomerize M-1-M to M-n-M (Figure 1.3).

Similar to the acetalization process, the oligomerization also occurs in the presence of an acid catalyst. As reviewed by Baranowski [26], these oligomerization reactions can be performed with both liquid and solid catalysts. Wang et al. tested various liquid acids as catalysts [27] and showed that sulfuric acid was the most successful liquid acid catalyst for producing M-n-M from trioxane and methanol (the same process as above but extended to allow oligomerization) with 64% conversion of methanol, where approximately 40% by mass of the M-n-M was $n > 2$. Similarly, ionic liquids investigated by Wu et al. [28] showed good ability to oligomerize M-1-M with trioxane and consistent conversion rates with reuse and a temperature-independent equilibrium concentration of various chain lengths. More common than liquid catalysts are various forms of solid catalysts, including ion-exchange resins, carbons, solid superacids, and zeolites [26]. The reported selectivity, across a wide range of M-1-M:CH₂O molar ratios, averages between 30 and 50%. Anomalously, Wu et al. report an exceptionally high selectivity to higher n of 88.5% using HZSM-5 zeolite catalyst with a Si/Al ratio of 580.

Burger et al. in particular provide a detailed study of the chemical kinetics underlying the M-n-M formation and oligomerization reactions [29]. Using a batch reactor, they investigate the

models which correctly predict M-n-M formation using Amberlyst 46 cation exchange resin. Using a liquid-phase, mole-fraction approach, they find that equilibrium constants of the various oligomers are equal within experimental error, but weakly temperature dependent. A pseudo-homogeneous model was fitted, but predicted faster OME formation than observed due to incomplete accounting for trioxane decomposition; an adsorption-based model which accounts for mass transfer to the catalyst accurately predicted the equilibrium and rates, but numerous assumptions were required which could not be experimentally verified. Later work from the same group by Schmitz et al. [10] shows that when accounting for the presence of hemiacetals, the pseudohomogeneous approach can accurately model OME formation.

Synthesis of higher OMEs has received less attention in literature. Lautenschütz et al. synthesize E-n-E from E-1-E and trioxane over Amberlyst 36 catalyst [30] in order to isolate and characterize these OMEs, following a similar process to that described above. No recent work has been published regarding the synthesis of P-n-P OMEs. Recent work by Arellano-Trevino synthesized a mixture of M-n-M, M-n-B, and B-n-B OMEs from trans-acetalization of an M-n-M mixture, primarily $n=3-5$, with butanol over Amberlyst 46. The resultant mixture contains a large number of oligomers, as well as formaldehyde, asymmetric OMEs, and large quantities of M-1-M. No attempt is made in this work to isolate individual OMEs. Stoichiometric ratios of butanol with M-n-M (2:1) were shown to produce larger quantities of FA and asymmetric OMEs; reactants rich in butanol showed much less FA and asymmetric OME production. Similar trans-acetalization reactions are documented by Drexler [31] where linear OMEs, E-1-E, P-1-P, and B-1-B, are reacted with a branched OME to produce more complicated asymmetric structures. These reactions are performed over a zeolite catalyst with Si/Al ratio of 25.

1.3.2 Physical and Chemical Properties of OMEs

The physical properties of many OMEs have typically been studied in the context of their direct applicability to engine usage, thus many engine studies will have small sections discussing the properties of the specific OME or mixture of OMEs used in the test. For example, Omari

discusses the CN, Reid vapor pressure, ν , and flammability limits of M-1-M in various blending ratios with traditional diesel [32].

One of the earlier attempts to systematically characterize OME properties is Burger et al. [33], wherein M-n-M is synthesized for $n=1-4$. They measure melting and boiling temperatures, viscosity, density, and CN. They find that, in comparison to typical diesel, only M-4-M has boiling temperature within the diesel range, no M-n-M have diesel-comparable viscosity, and all M-n-M have higher density, where the density and viscosity both rise with higher n . M-1-M is found to have a CN of 29, below diesel requirements, but M-2-M, M-3-M, and M-4-M have CN 63, 70, and 90 respectively, all above the typical diesel CN. It is found that while dimethyl ether (in our nomenclature, this would be M-0-M) cannot be mixed with diesel due to requirements of storage under pressure; however, there is not a miscibility gap for $n>1$. Low flash points, which are a safety concern for combustible liquids like diesel, are found for $n<3$, thus Burger concludes on the basis of the tested properties that M-3-M and M-4-M are the most suitable methyl-terminated OMEs for diesel blending.

The definitive work so far considering properties of OMEs is the work of Lautenschütz [30], who characterizes M-1-M - M-5-M and E-0-E - E-4-E in oxygen mass percent, refractive index, density, melting and boiling points, autoignition and flash points, CN, lubricity, viscosity, and surface tension. Comparable CN is found for M-n-M to Burger's past work, further, CN for E-n-E is shown to be above diesel minimum standards for all n (corrigendum to [30]). Several of the tested OMEs have unacceptably low flash points and viscosities, and poor lubricity. Some heavier OMEs, in agreement with Burger's work, have acceptable volatility, and most OMEs have higher density than typical diesel, which helps to offset the reduction in heating value due to oxygen content.

1.3.3 Combustion and Engine Performance of OMEs

Interest in OMEs as diesel additives for soot reduction reaches back several decades. In the late 1990s and early 2000s, most research focused on M-1-M as the additive of choice [15, 16, 34,

35]. Maricq [34] tested M-1-M blended 17% and 30% by volume in diesel in a 1.8L turbodiesel passenger car equipped with an oxidation catalyst exhaust treatment system, which is operated on a chassis dynamometer following the then-current Federal Test Procedure drive cycle. Approximately 40% reduction in particulate mass reduction was found for the lower blend ratio, and no clear further reduction was found for the higher blending ratio. The effect on NO_x emission of M-1-M emission was negligible. FA emissions were estimated as 50% higher for M-1-M than for diesel. Kocis [15] tests M-1-M blended 5% and 10% in an optically-accessible single diesel cylinder engine. M-1-M blends had longer ignition delays and higher peak burn rates. Addition of M-1-M produced small reductions in CO₂ and NO_x emissions, but negligible effects on CO emissions. Lower CO₂ emissions are in line with their predictions due to lower carbon density per unit energy in the fuel, and the reductions in NO_x are attributed to longer ignition delays. Vertin tests M-1-M in diesel in ratios from 5% to 30% by volume in a 5.88L Cummins 6 cylinder turbodiesel with fixed injection timing. It is found that addition of M-1-M increases total hydrocarbon emissions (THC), CO, and (in contrast to Kocis et al.) CO₂, while reducing NO_x emissions by up to 10% and PM emissions by up to 35%, where the PM emissions reductions were not linear with blending ratio. Further, they note that the low flash point of M-1-M makes M-1-M/diesel blends unsuitable as drop-in fuels due to safety issues. Finally, Ball et al. [16] test M-1-M in a 2.2L Daimler-Chrysler turbodiesel with high compression ratio and variable EGR. Individual injection timing of each cylinder is possible with this engine. They find lower PM emissions for a 15% blend of M-1-M, however, similar PM reductions are also found for Fischer-Tropsch synthetic diesel. Later work continues to study M-1-M [20, 25], and along with continuing to show the emissions characteristics, it is shown that M-1-M may increase the thermal efficiency of CI engine operation.

More recently, focus has turned to the usage of n>1 OMEs, since (as discussed in the Properties section, and in some of the works testing M-1-M) certain M-1-M properties such as flash point and CN are less than ideal for CI engine usage. Omari [32] test various M-n-M blended 35% in diesel and neat in a single-cylinder research engine. They find that at low loads, M-n-

M neat or blended will increase efficiency, however, at high load, the effect is minimized and neat OME shows less thermal efficiency. The effect of varying n on PM emissions at a given blending ratio was negligible, while neat M-n-M had essentially zero PM emissions, and all M-n-M blends significantly reduced PM with respect to diesel at any given load point. Varying chain length also has negligible effect on FA, THC, and CO emissions, while the presence of OME in general will decrease CO and THC while increasing FA. Pélerin tests M-n-M in a MAN heavy-duty D20 6 cylinder engine [36]. As with Omari, M-n-M shows improved efficiency and negligible effect of n on most emissions categories (although it is noted that M-(3-6)-M has significantly higher FA emissions than M-1-M), and reduces soot, CO, and NO_x.

Only one study has been published on the usage of non-methyl OMEs in engines; Lehrheuer et al. [37] test E-1-E not as a CI fuel but rather for a gasoline engine under the Gasoline Controlled Auto-Ignition method. In a single-cylinder research engine, low internal recirculation is required to ignite E-1-E in this engine compared to RON 95 gasoline, as would be expected of a fuel with moderate CN. Slightly higher efficiency is found compared to gasoline, and NO_x emissions vary depending on recirculation percentage. They conclude that blending with high-octane fuels may be necessary to use E-1-E effectively in these types of engines.

Additionally, only one study has considered any use of OMEs in a spark-ignited environment. Langhorst et al. [38] blended M-1-M (and also dimethyl carbonate) with gasoline for testing in an optically accessible CVCC. M-1-M and dimethyl carbonate are used as oxygenated molecules primarily to probe the effectiveness of diagnostic methods rather than as intentional proposals of engine-appropriate fuels, however, it is found that in spark and corona ignition in this CVCC, there is little difference in OH emission for low (up to 10 vol%) M-1-M blending, but high (50 vol%) blends produce significantly lower detectable OH, and the ignition occurs measurably later post-spark. However, spark ignition produced highly variable OH emission, while corona ignition yielded far more stable combustion. Langhorst makes no recommendations with respect to the suitability of M-1-M/gasoline blends for actual engine use.

Chemical kinetic mechanisms for OME combustion have been developed primarily for M- n -M OMEs, usually with n up to 3, and most work focusing on M-1-M. As early as 2001, Daly et al. develop a mechanism for M-1-M high-temperature reactions based upon jet-stirred reactor combustion [39]. Among their conclusions, it is found that H_2 is a major product (unusual for combustion), significant formaldehyde is present, and some light hydrocarbons were also present. They use a mechanism containing methane, ethane, propane, propene, propyne, ethylene, and acetylene as a basis for development of the M-1-M mechanism, with analogies to dimethyl and diethyl ethers for rate constants of C-O bond scissions, and ethane and propane for H-abstractions. The mechanism provides reasonable matching with experimental data. Later work by Dias et al. [40] builds upon this work and begins development of a mechanism including E-1-E reactions, which are modeled by analogy to M-1-M reactions.

More recently, attempts have been made to expand the mechanisms to M-2-M and M-3-M, and more detailed M-1-M and E-1-E mechanisms. Sun [41] and He [42] both expand M- n -M mechanisms up to $n=3$, and Cai expands this up to $n=4$. Sun finds that, contrary to common behavior of hydrocarbons, secondary C-H bonds (on CH_2 groups) are higher energy than primary (CH_3) bonds due to the proximity of oxygen molecules; further, it is found that longer OME chain lengths reduce the strength of bonds at any given position. Laminar flame [41] and rapid compression machine (RCM) [42] compositions are well modeled by the new mechanisms; it is found once again that high concentrations of CO and H_2 exist in M- n -M combustion products. Cai et al builds upon the work by He and Sun by providing additional validation via shock tube of M-2-M ignition, which was not studied directly in the prior work. Using shock tube ignition of M-1-M – M-4-M, Cai builds a M- n -M mechanism validated on the shock tube ignition using M-1-M rates and reaction classes as rules for an automatic mechanism generator. The rates, however, are extrapolated from M-1-M rather than being directly calculated for M-2-M and higher. De Ras. et al. studied the detailed chemistry of specifically M-2-M in a pyrolysis reactor and rapid compression machine [43, 44], and performed quantum chemical calculations to more accurately develop rates. De Ras finds that C-O bond scission is the most likely

initial step, followed by exothermic formation of stable species rather than radicals, while the second most likely step is the radical formation step due to formation of an unstable intermediate that rapidly decomposes to methyl and formyl radicals. This initiating step allows for the subsequent H-abstraction and O₂ addition that is the defining feature of hydrocarbon ignition. The most recent work in this area is by Shrestha et al. [45], which publishes a new mechanism incorporating their own calculations with the work of Cai and De Ras, and provides excellent accuracy for flame speeds and ignition delays for up to $n=3$, while the work of Cai has superior speciation measurements for jet-stirred reactor measurements.

Li et al. develop a detailed E-1-E mechanism [46]. Of particular note is the observation that the location of H abstraction has significant effects on the ability to form ROO structures leading to rapid reaction cascades - in particular, central H sites on CH₂O groups are unlikely to isomerize at low temperatures and will inhibit ignition. Comparison of the model results with RCM and shock tube tests provides good agreement, however, simulation results at very lean and very rich conditions show strange behavior of IDT with respect to $1000/T$, with unexplained inflection points that are not present at conditions closer to stoichiometric. Simultaneously, Jacobs et al. perform a detailed analysis of E-1-E kinetics, including shock tube, RCM, laminar flow reactor, spherical bomb, and counterflow flame tests to validate their model development [47]. Similar conclusions to Li are found, wherein the specific location of the initial H abstraction from the E-1-E molecule has a strong effect on whether a transition to OOQOOH and radical branching occurs, or whether instead the radical scissions to double-bonded species; specifically, the central carbon is lower probability for OOQOOH cascading, and the first carbon in the ethyl group is the highest probability.

1.4 Objectives and Structure of Research

This research is part of a larger cooperative effort between Colorado State University, University of Colorado, Yale University, and the National Renewable Energy Laboratory to develop and identify OMEs which are the best balance of soot reduction, engine performance, and com-

patibility with current diesels. As part of this cooperation, the goal of this work is to provide the synthesis work for partner institutions to supply their research, as well as to do independent characterization of properties and combustion characteristics of many possible OME candidates. New and unique contributions to the literature on alternative fuels include synthesis of previously untested OME fuels, property characterization and engine testing of these, and fundamental combustion studies of some new OMEs to contribute to fuel selection and mechanism development.

The first phase of the project consisted primarily of investigating the synthesis of these new OMEs, using several different methods. This synthesis continues through the duration of the research. After synthesis is complete, throughout the second phase, fuel property characterization tests are performed to narrow the field of candidates for engine testing. In support of chemical kinetics work being performed at the University of Colorado, some pre-vaporized autoignition testing of a subset of the OMEs has been performed. Simultaneously, engine testing candidates were downselected, and further synthesis is performed to produce sufficient quantities for engine testing. A recommended OME/diesel blend is created and sent to an external laboratory for characterization of compatibility with diesel under the ASTM D975 standard. Finally, the final phase of research involves investigation of iP-1-iP, a very low-reactivity OME which has never been studied for combustion purposes and is considered under the SI rather than CI application.

Chapter 2

Synthesis of New Extended-Alkyl and Extended-Chain OMEs

2.1 Synthesis of Butyl-Terminated Oxymethylene Ethers

The content of this section is being prepared for submission to the Fuel Processing Technology journal.

2.1.1 Methods

Experimental Setup

All synthesis experiments for this section were conducted in a 300 mL Parr 4651 stirred autoclave reactor. Reactants were purchased from Millipore Sigma and Fisher Scientific. M-1-M, n-butanol, and s-trioxane were used as reactants with purity >99%, as purchased from either Sigma Aldrich or Fisher Scientific. Bio-derived isobutanol was acquired from Gevo with purity 98.7%, balance isopentanol. Reactions were performed at stoichiometric conditions for the respective reactions, with 0.5 mass% catalyst. The idealized stoichiometry is presented below. As will be discussed later, the equilibrium products included other components.



All reactions were performed under 5 bar N₂, with the reactor being filled and purged 3 times prior to final pressurization. The reactor was then heated to the target temperature and maintained under constant stirring at 600 rpm for the duration of the experiment (except during sample removal).

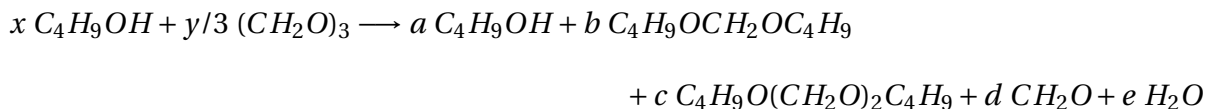


Figure 2.1: Parr reactor used for this work

Analytical Methods

Liquid samples were primarily analyzed in a HP 5890 Series II gas chromatograph equipped with a flame ionization detector (GC-FID) and a Restek Rtx-Wax 0.25 μ m x 0.25 mm x 30 m column with helium carrier gas at 50:1 split ratio. The device was operated at 200°C inlet and detector temperature with a temperature profile of 1 minute hold at 60°C, followed by 20°C ramp to 200°C and held at that temperature for 7 minutes. For reactions with H₂O products, water content was measured using Karl Fischer titration in a Metrohm 831 KF titrator with Hydranal Coulomat AG reagent. In one case, discussed in Section 2.1.2, gas chromatography-mass spectroscopy was used to identify an unknown peak in the GC-FID chromatogram; this device used a 0.25 μ m x 0.25 mm x 30 m VF5-MS column, operating under the same temperature ramp as the GC-FID, where dichloromethane was used as a solvent in 100:1 volume ratio to the synthesis sample.

In Pathway 2, formaldehyde and water cannot be accurately quantified with GC-FID. As a result, we determined the mole fractions of these components algebraically, given the known fractions of B-1-B, butanol, and B-2-B (when present), and verified by comparison of calculated water content with measured water content via Karl Fischer titration. Insufficient thermodynamic data exists for the B-1-B and B-2-B products to perform a free-energy minimization equilibrium calculation, so this method was used instead. The fractions are determined as follows and then normalized to sum to 1:



a, b, c = known from GC – FID

$$x = a + 2b + 2c, \quad y = x/2, \quad d = y - b - 2c, \quad e = b + c$$

Catalyst Properties

Four commercially available cation exchange resins were examined in this study: Amberlyst 15 (Millipore Sigma), Amberlyst 46 (Sigma Aldrich), Amberlite IRC 120H (Fisher Scientific) and Dowex G26 (Millipore Sigma). The properties of these catalysts are described in Table 2.1 below. Properties are drawn from the manufacturer, or, where applicable, the cited literature where a more detailed characterization was performed. The total exchange capacity refers to the number of sites capable of supporting ion exchange reaction, typically defined as milliequivalents of exchangeable ion per dry gram of polymer [48].

Table 2.1: Properties of ion-exchange resin catalysts used in this study

		Amberlyst 15	Amberlyst 46	DOWEX G26	Amberlite IR120
Type		Macroreticular	Macroreticular	Gel	Gel
Surface Area	[m ² /g]	45.8	75.0	not specified	<0.10
Total Exchange Capacity	[mequiv/g]	4.6	0.87	2.05	2.77
Moisture Holding Capacity	[% H ₂ O]	50	26 – 36	45 – 52	46
True Density	Skeletal [g/ml]	1.51	not specified	1.22	1.39
Porosity	[ml/ml]	0.32	not specified	not specified	0.02
Reference		[49–51]		[52]	[49, 51]



Figure 2.2: Butoxymethoxymethane – intermediate product, formed via (R2.1.1)

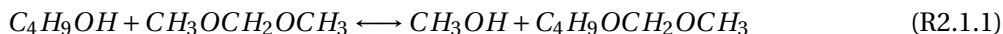


Figure 2.3: Dibutoxymethane – target product, formed via (R2.1.2) or (R2.2.2)

2.1.2 Results and Discussion

Reaction Pathways

In evaluating Pathway 1 for this synthesis, we must consider the production of both the final product, dibutoxymethane, as well as an intermediate, butoxymethoxymethane (see Figure 2.2, Figure 2.3). This intermediate molecule is formed when only one of the methyl groups on the original OME, dimethoxymethane, is replaced by the butyl group from the alcohol. Dibutoxymethane is then formed when a butoxymethoxymethane has its remaining methyl group exchanged as well. This two-step reaction is described below in (R2.1.1) and (R2.1.2), producing dibutoxymethane, butoxymethoxymethane, and methanol.

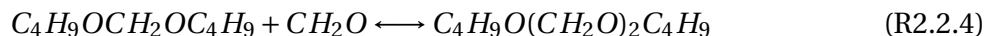
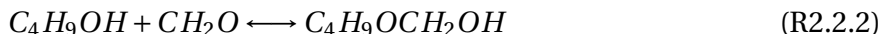


Pathway 2 did not produce any measurable intermediates in the same way as Pathway 1; however, it is expected that the acetalization proceeds through a hemiacetal which is fully consumed. This reaction is presented as a four-step process of trioxane decomposition followed by acetalization producing both water as a byproduct, and under certain conditions, a small amount of a chain-extended molecule, butoxy-(methoxy)₂butane (Figure 2.4).





Figure 2.4: B-2-B – oligomerized product, formed via (R2.2.3)



Effectiveness of Various Catalysts in Pathway 1 Synthesis

For the first experiment, to select the preferred catalyst for further experimentation, we consider the effects of four different ion exchange resins as described above in Table 2.1 on the Pathway 1 synthesis route. The results of this reaction for the different catalysts were compared with reaction conditions of 60°C and 0.5 mass % catalyst with stoichiometric butanol and dimethoxymethane (2:1), as shown in Figure 2.5 and Figure 2.6. We find that, for this reaction, Amberlyst 15 was the most effective catalyst, producing 18 mole % butoxymethoxymethane and 10 mole % dibutoxymethane. Amberlyst 46 and Amberlite IRC 120 had somewhat lower yields, and the DOWEX G26 was the least effective in this conversion.

We attribute the differing performance of these catalysts to the morphology of the beads and the total exchange capacity. Amberlyst 15 and 46 are both considered macroreticular resins and have high porosity, leading to very high available surface area for reaction in comparison to the Amberlite 120 and DOWEX G26, both of which are gel resins. It has been shown that alcohols are more effectively adsorbed to macroreticular resins than to gel resins [53]. Additionally, total exchange capacity, a measure of available ion exchange sites, is highest for Amberlyst 15 [54]. Together, these contribute to Amberlyst 15's high performance in this reaction. Amberlyst 46, it may be noted, was the second-best performing catalyst despite its lower total exchange capacity; this catalyst is only surface sulfonated [55], contributing to the lower exchange capacity (i.e., only the outermost surface of the resin has sulfonated groups, rather than having sulfonated

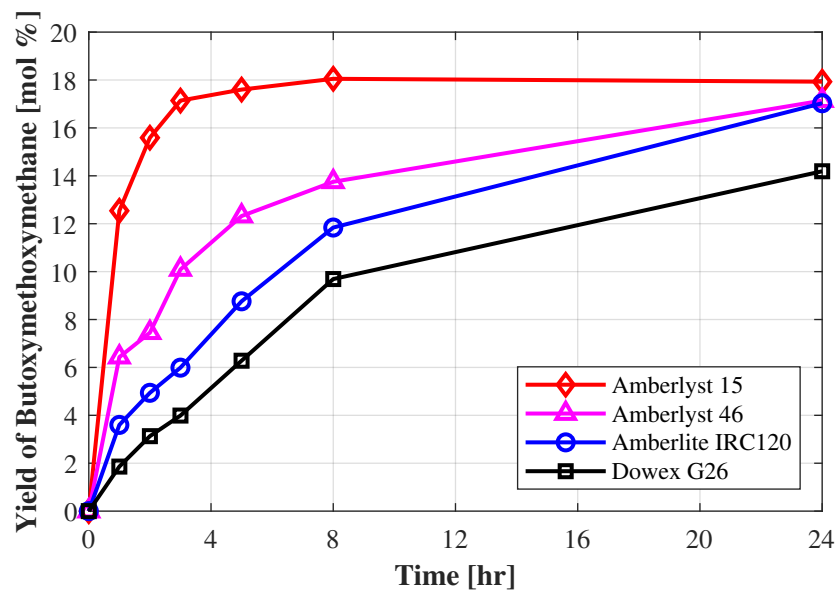


Figure 2.5: Mole fraction yield of butoxymethoxymethane at 60°C and 0.5 mass % catalyst, 2 mol butanol : 1 mol dimethoxymethane

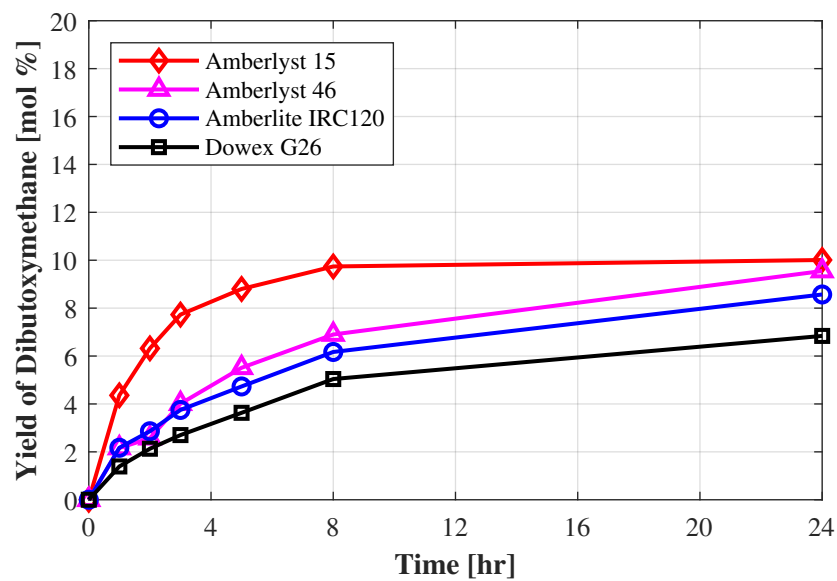


Figure 2.6: Mole fraction yield of dibutoxymethane at 60°C and 0.5 mass % catalyst, 2 mol butanol : 1 mol dimethoxymethane

groups present through the entire structure), but the high surface area helps to counteract this flaw. The gel resin structure of Amberlite 120 and DOWEX G26 do not have discrete pores and have some of the acid sites embedded within the resin, reducing mass transfer to the active sites. These results thus suggest that the reaction is strongly affected by mass transfer effects in addition to chemical kinetics.

Effect of Temperature on Pathway 1 Reactions

Having determined that Amberlyst 15 is the most effective catalyst for production of dibutoxymethane, we proceed with investigation of the temperature effect on the Pathway 1 reactions. We continued to use stoichiometric reactant ratio and 0.5 mass% catalyst. Three temperature conditions were tested – 40°C, 60°C, and 80°C. As shown below in Figure 2.7 and Figure 2.8, the production rate of both products was highly temperature dependent, while the equilibrium composition appeared to be independent of temperature.

$$y = a \frac{t}{b + t} \quad (\text{Eq. 2.1})$$

A saturation growth model (see (Eq. 2.1)) well describes the change over time of the desired products, and is used for comparison of time constants and to estimate equilibrium for reactions which do not reach equilibrium in the 24 hours measurement period, where y is the mole fraction, a is the asymptotic equilibrium, and b is a rate modifier. In the 40°C case, dibutoxymethoxymethane reached the equilibrium fraction, albeit at a slower rate, but dibutoxymethane did not reach equilibrium in the measured time (24 hours). The time constants τ to reach $1 - 1/e * a$ at 40°C, 60°C, and 80°C, are 8.57 hours, 2.40 hours, and 9.64 minutes, respectively. The dibutoxymethane yield in the first hour roughly doubled for every 20°C increase in temperature. The 80°C reaction had comparable yield of products to the lower temperatures, however, it is established that higher temperatures promote hydrolysis of dimethoxymethane to methanol and formaldehyde [56], and we observed higher methanol concentrations at 80°C than 60°C despite the comparable target product yields.

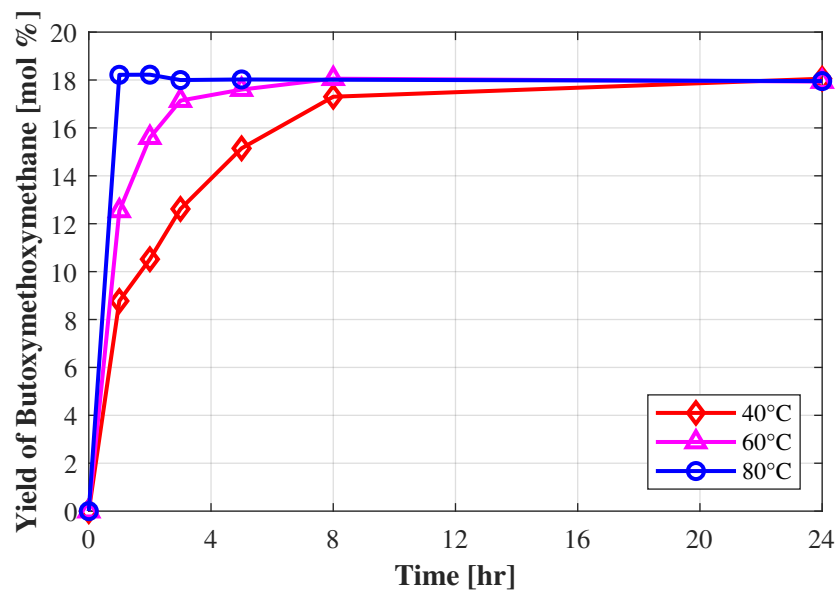


Figure 2.7: Pathway 1 mole fraction yield of M-1-B with 0.5 mass % Amberlyst 15, 2 mol butanol : 1 mol dimethoxymethane

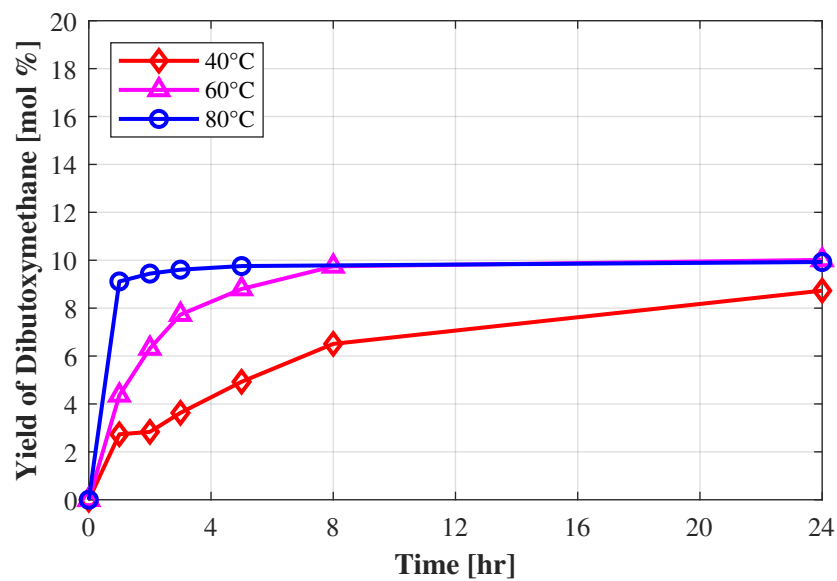


Figure 2.8: Pathway 1 mole fraction yield of B-1-B with 0.5 mass % Amberlyst 15, 2 mol butanol : 1 mol dimethoxymethane

Effect of Temperature on Pathway 2 Reactions

Again using Amberlyst 15 as the preferred catalyst, we applied these reaction conditions to the Pathway 2 synthesis method. Unlike Pathway 1, where all reactants and products can be measured with GC-FID techniques, for Pathway 2, formaldehyde and water cannot be accurately quantified with GC-FID. As a result, we determined the mole fractions of these components algebraically, given the known fractions of B-1-B, butanol, and B-2-B (when present).

These calculations were verified by testing the water content by mass at the end of the reactions with Karl-Fischer titration. It was found that at 60°C, the water mass fraction was 92% of what was predicted from Eqs. 1-5, and for the 80°C and 100°C cases, the water mass fractions was 84% and 72% of the prediction respectively. As there will be some water loss to evaporation, and some consumption of H and OH radicals may occur as terminating groups in the formation of paraformaldehydes or methanediol [57] from unreacted formaldehyde is to be expected (which is not predicted in the above equations), and for the higher temperature cases some water precipitated out of solution into a separate phase at the bottom of the container due to higher dibutoxymethane concentration (and thus lower water solubility [58]), we consider this result to be reasonable. Additionally, as the higher temperature cases will more rapidly depolymerize trioxane [59], there will be additional time and concentration of formaldehyde for formation of these possible OH consumers. Further work may be warranted to determine the exact forms of the unreacted formaldehyde, which may lend greater accuracy to the calculation of water content.

Of the prior three reaction conditions – 40°C, 60°C, and 80°C – only the latter two were successful for this case. In stoichiometric proportions, 2:1 molar ratio of butanol to formaldehyde (in our case, specifically 6:1 butanol to trioxane), the trioxane will dissolve fully at elevated temperatures, but at room temperature some trioxane will remain solid. It was observed that all samples until the 24 hour sample at the 40°C condition had trioxane crystallizing out of solution once the sample cooled to room temperature, which both posed a risk of damage to the GC-FID instrument if solids formed in the injector, and indicated that there was very little con-

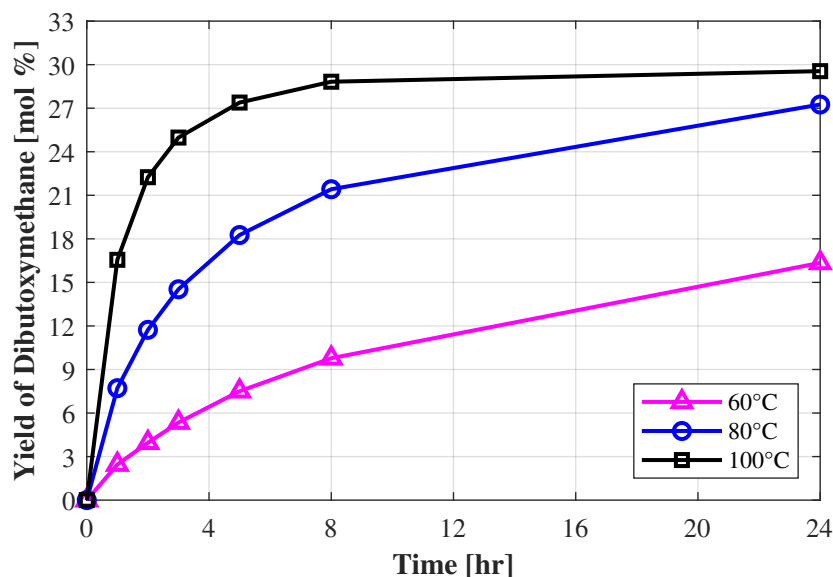


Figure 2.9: Pathway 2 mole fraction yields of B-1-B with 0.5 mass % Amberlyst 15, 2 mol butanol : 1 mol formaldehyde (6 mol butanol : 1 mol trioxane). B-2-B was present in small (<2 mol% after 24 hours) concentrations for 80°C and 100°C tests.

version of trioxane. Even after 24 hours, some solidified, unreacted trioxane was observed on the interior of the reactor vessel. Thus, this condition was discarded as being unsuitable, and a higher temperature third case, 100°C, was added. The reactions at 60°C, 80°C, and 100°C were much more successful, showing no apparent crystallization of trioxane at any point, and are presented in Figure 2.9.

It may be immediately observed from Figure 2.9 that this reaction proceeds differently than Pathway 1; the different temperatures produced significantly different yields at 24 hours, rather than simply accelerating the reaction to a temperature-independent equilibrium – an apparent equilibrium of 29.5% by mole of dibutoxymethane was reached only for the highest temperature case. Saturation growth models fitted to these indicate that the 60°C case may approach a lower equilibrium dibutoxymethane yield of 23% while the 80°C and 100°C both approach an equilibrium of approximately 31% for extended time. The time constant for 60°C to the lower equilibrium was 17.6 hours, while the higher temperature cases, 80°C and 100°C, had shorter time constants, 5.62 hours and 1.43 hours respectively, acknowledging that the asymptotic equilibrium value here is an estimate from (Eq. 2.1).

Pathway 2 was a significant improvement in yield of the desired product (dibutoxymethane), with the 80°C case producing more than twice the yield by mole of its Pathway 1 equivalent. In addition, we observed that the oligomerized product, B-2-B, was produced in small but measurable quantities at later stages of the 80°C reaction, up to about 1%, and at all stages in the 100°C case up to 1.6%, while the 60°C reaction produced negligible amounts of this product, even at 24 hours. As this reaction did produce water as a byproduct, and contained some amount of unreacted formaldehydes, industrial applications may require additional processing steps to be viable, however, from the standpoint of yield of desired product (specifically B-1-B), Pathway 2 was the clearly superior method, yielding higher equilibrium mole fraction of B-1-B at the cost of slower reaction times.

Kinetic Modeling of B-1-B Formation

The pseudo-homogeneous (P-H) kinetic model of reaction is an assumption wherein a heterogeneous mixture of liquid reactant with a solid catalyst is treated as a single phase, liquid mixture, and thus assumes that the active sites of the solid catalyst are unaffected by any boundary layer interactions between liquid reactant and solid catalyst surface [60]. P-H models have been used in literature for liquid-phase reactions using solid acid catalysts [29, 60, 61] for OMEs and other compounds, however, for OMEs, this application has been primarily the synthesis of methyl-terminated OMEs, wherein acetalization and chain extension occur simultaneously from the same reactants; further, end-group exchange of OMEs using alcohols and M-1-M has been studied by Arellano-Treviño et al. [62] and Drexler et al. [31], however, neither of these studies consider kinetic models of the reaction, presenting only the results and considering fuel properties. Here, the P-H model is applied to both Pathway 1 and Pathway 2 reactions for formation of B-1-B, and the applicability and effectiveness of the P-H model is considered. For Pathway 2, the hemiacetal is not measured in the final product, and so is treated with the steady-state assumption; additionally, the dissolution of trioxane is neglected in the rates and CH_2O is assumed.

Pathway 1 Reaction Rate Equations ((R2.1.1) and (R2.1.2)):

$$\begin{aligned}\frac{d[MeOH]}{dt} &= \frac{m_{catalyst}}{m_{reactant}} \left(k_1[BuOH][M1M] - k_{-1}[M1B][MeOH] \right. \\ &\quad \left. + k_2[BuOH][M1B] - k_{-2}[B1B][MeOH] \right) \\ \frac{d[BuOH]}{dt} &= \frac{m_{catalyst}}{m_{reactant}} \left(-k_1[BuOH][M1M] + k_{-1}[M1B][MeOH] \right. \\ &\quad \left. - k_2[BuOH][M1B] + k_{-2}[B1B][MeOH] \right) \\ \frac{d[M1M]}{dt} &= \frac{m_{catalyst}}{m_{reactant}} \left(-k_1[BuOH][M1M] + k_{-1}[M1B][MeOH] \right) \\ \frac{d[M1B]}{dt} &= \frac{m_{catalyst}}{m_{reactant}} \left(k_1[BuOH][M1M] - k_{-1}[M1B][MeOH] \right. \\ &\quad \left. - k_2[BuOH][M1B] + k_{-2}[B1B][MeOH] \right) \\ \frac{d[B1B]}{dt} &= \frac{m_{catalyst}}{m_{reactant}} \left(k_2[BuOH][M1B] - k_{-2}[B1B][MeOH] \right)\end{aligned}$$

Pathway 2 Reaction Rate Equations ((R2.2.2)-(R2.2.4)):

$$\begin{aligned}\frac{d[BuOH]}{dt} &= \frac{m_{catalyst}}{m_{reactant}} \left(-k_1[BuOH][CH_2O] + k_{-1}[BHA] \right. \\ &\quad \left. - k_2[BuOH][BHA] + k_{-2}[B1B][H_2O] \right) \\ \frac{d[CH_2O]}{dt} &= \frac{m_{catalyst}}{m_{reactant}} \left(-k_1[BuOH][CH_2O] + k_{-1}[BHA] \right. \\ &\quad \left. - k_3[B1B][CH_2O] + k_{-3}[B2B] \right) \\ \frac{d[H_2O]}{dt} &= \frac{m_{catalyst}}{m_{reactant}} \left(k_2[BuOH][BHA] - k_{-2}[B1B][H_2O] \right) \\ \frac{d[B1B]}{dt} &= \frac{m_{catalyst}}{m_{reactant}} \left(k_2[BuOH][BHA] - k_{-2}[B1B][H_2O] \right. \\ &\quad \left. - k_3[B1B][CH_2O] + k_{-3}[B2B] \right) \\ \frac{d[B2B]}{dt} &= \frac{m_{catalyst}}{m_{reactant}} \left(k_3[B1B][CH_2O] - k_{-3}[B2B] \right) \\ [BHA] &= \frac{k_1[BuOH][CH_2O] + k_{-2}[B1B][H_2O]}{k_{-1} + k_2[BuOH]}\end{aligned}$$

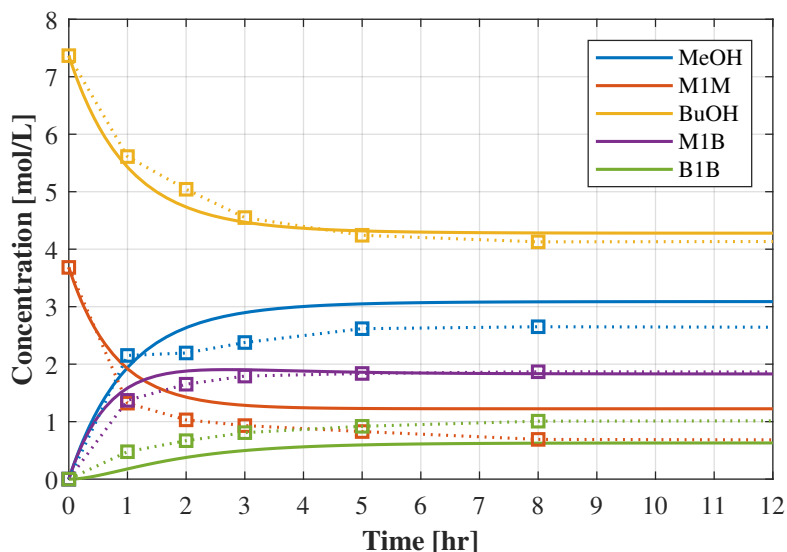


Figure 2.10: ODE optimization of Pathway 1 kinetic parameters at 60°C using pseudo-homogeneous model, accounting for all components. Solid lines indicate P-H model, symbols with dotted lines are experimental data.

Table 2.2: Pathway 1 rate and equilibrium constants for tested catalysts at 60°C, where $K_{n,eq} = k_n/k_{-n}$

Method	Catalyst	k_1	k_2	$K_{1,eq}$	$K_{2,eq}$
Optimize All	Amberlyst 15	0.379	0.106	1.08	0.248
	Amberlyst 46	0.0769	0.0229	0.231	0.231
	Dowex G26	0.0702	0.0172	0.834	0.184
	Amberlite IRC120	0.0488	0.0166	0.826	0.161
Optimize M-1-B and B-1-B	Amberlyst 15	0.363	0.251	2.40	0.560
	Amberlyst 46	0.0895	0.111	1.98	0.544
	Dowex G26	0.0899	0.232	1.62	0.407
	Amberlite IRC120	0.0603	0.196	1.62	0.402

The equations for optimization of rate constants are shown above for both pathways, where BHA refers to the butyl hemiacetal steady-state intermediate. The measured mole fractions are converted in MATLAB to molarity and the reaction rate constants are solved via optimization of the ODE45 method, using a least-squares difference method between the measured values and optimized ODE solutions.

For Pathway 1 reactions (see Figure 2.10 and Figure 2.11), the P-H model does not appear to accurately capture the reaction behaviors. When optimized for a general least-squares difference target, good prediction of BuOH and M-1-B is observed, however, the model under-

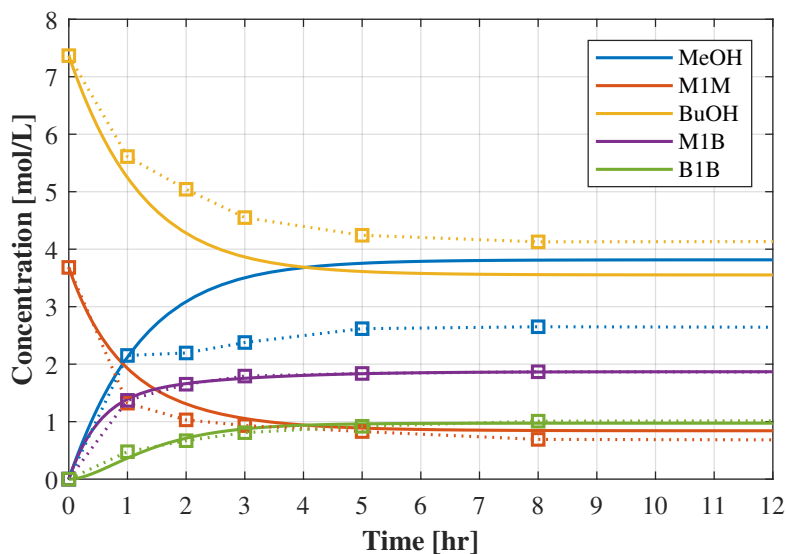


Figure 2.11: ODE optimization of Pathway 1 kinetic parameters at 60°C using pseudo-homogeneous model, accounting for only M-1-B and B-1-B formation in the optimization process.

Table 2.3: Pathway 1 rate and equilibrium constants for Amberlyst 15 at different temperatures, $K_{n,eq} = k_n/k_{-n}$

Method	Temp. [K]	k_1	k_2	$K_{1,eq}$	$K_{2,eq}$
Optimize All	313	0.123	0.0100	0.703	0.515
	333	0.379	0.106	1.08	0.248
	353	0.871	0.209	1.16	0.263
Optimize M-1-B and B-1-B	313	0.135	0.106	1.54	0.359
	333	0.363	0.251	2.39	0.560
	353	1.54	0.792	2.50	0.592

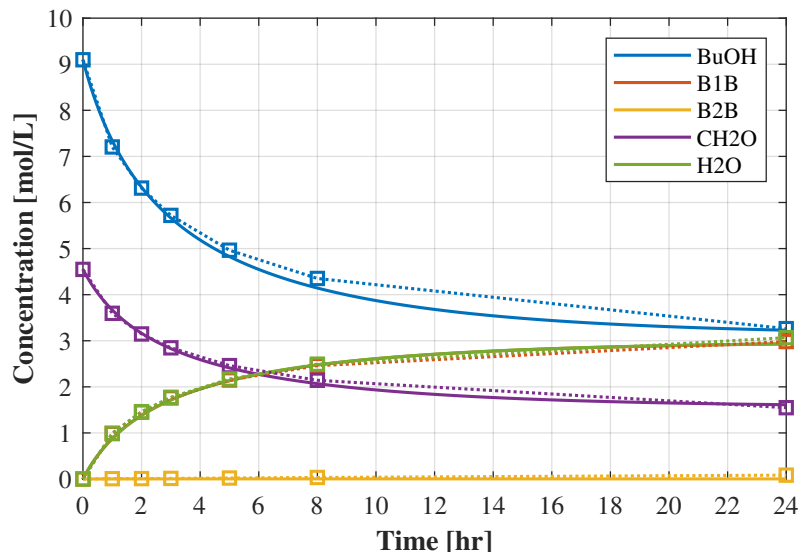


Figure 2.12: ODE45 optimization solution to P-H model for Pathway 2 at 80°C, including B-2-B in calculations

Table 2.4: Pathway 2 rate and equilibrium constants for Amberlyst 15 at different temperatures, including B-2-B in analysis, $K_{n,eq} = k_n/k_{-n}$

Temp. [K]	k_1	k_2	k_3	$K_{1,eq}$	$K_{2,eq}$	$K_{3,eq}$
333	11.2	7.00e-4	0.0708	3.25	0.0184	3.95e-4
353	42.9	1.90e-4	0.0455	57.1	0.0104	1.58e-3
373	7.66	5.64e-4	0.0134	76.6	0.0138	0.0275

predicts B-1-B formation (and subsequently, M-1-M consumption). MeOH is, unexpectedly, over-predicted despite the under-prediction of B-1-B formation; M-1-B and B-1-B should be formed concurrently with MeOH. Targeting the optimization to correctly predict M-1-B and B-1-B yields good results for these two specifically, however, MeOH formation is massively over-predicted and BuOH consumption under-predicted. From this, it appears that the proposed two-step P-H mechanism does not fully capture the reaction scheme. Not only are initial rates not accurate, product concentrations are not accurately calculated; this indicates that other reactions, particularly MeOH formation, may be occurring which are not captured in the proposed reaction scheme. Further detailed study would be required to determine the correct reaction scheme and modeling method.

As is consistent with past literature, the P-H method effectively models the Pathway 2 reactions, which are the standard acetalization reactions modeled in methyl-terminated OME reactions. The chain extension reaction appears to be primarily relevant at higher temperatures; at 60°C, negligible B-2-B is measured, while at 80°C and above, small but non-negligible B-2-B production is observed.

Biofuel Possibilities for Butyl-Terminated Ethers

Desire to reduce CO₂ emissions has driven attempts to find alternative, non-combustion powertrains for many vehicle types. As reviewed by Kluschke et al. [63], even in an optimistic scenario for alternative powertrains for heavy duty vehicles, combustion engines remain relevant, occupying approximately 40% of market share by 2050, and biofuels for these engine systems are an option studied in a number of the reviewed articles and the most competitive option in at least one. Biofuels are an attempt to approximate a “net zero” or “carbon neutral cycle” approach, wherein all carbon emitted into the environment is both reused for future energy, and is itself sourced from carbon in the environment. An “ideal” net zero fuel would emit no more carbon into the atmosphere (as CO₂ or otherwise) than is contained in the source material (e.g. biomass) for the fuel, so that upon combustion, the CO₂ produced can then be reabsorbed by plant matter and later turned into more biofuel [64] without changing the total amount of carbon in the atmosphere.

Bio-derived n-butanol is a well-studied process, but hindered by low throughput due to poisoning of the fermentation species by the produced butanol [65, 66]. Further, it is established that sulfur and nitrogen compounds, which are commonly found in bio-derived feedstocks, may have a negative effect on catalytic activity by poisoning active sites [67, 68]. Thus, we acquired a sample of iso-butanol from Gevo Inc. with a bio-derived source, specifically from #2 yellow dent corn, as a proof-of-concept for synthesis of an extended-alkyl OME from a known bio-source. Following the Pathway 2 reaction process at 80°C with stoichiometric reactants and 0.5 mass% Amberlyst 15, a similar yield curve was found. A curve-fit suggests a slightly lower equilibrium of 29 mol% iB-1-iB. An additional peak is found in the chromatogram in addition

to expected peaks from the iB-1-iB and iB-2-iB; GC-MS lookup was unable to accurately identify this compound, but we tentatively propose that it may be the acetalization of iso-pentanol, present at 1.3% in the provided sample, to a new iso-pentyl-terminated oxymethylene ether.

2.2 Synthesis and Chain Growth of Other OMEs

The synthesis of B-1-B was investigated directly as it was identified early on as a likely candidate for diesel substitution; structure-property relations indicated a high likelihood of ideal properties [58]. However, other OMEs were investigated in the course of this study, many of which needed to be synthesized in-house. M-n-M is commercially available and a supply was provided by Oak Ridge National Laboratory for this study; additionally, E-1-E – B-1-B are easily acquired from Fisher, Sigma, or other chemical providers. However, the branched (iP and iB) OMEs, and extended-chain / extended-alkyl OMEs were not commercially available. These were synthesized in-house; the processes for doing so are discussed here in this section. Several of the conclusions from the detailed study of B-1-B were applied here, most particularly the catalyst and pathway selection. For (relatively) large-scale production, a flow reactor was used rather than the batch reactor discussed above; additionally, once the methods were established as effective, measurements were taken merely for quality control purposes rather than scientific characterization, so much of the discussion in this section will be less detailed.

2.2.1 Method of Production of X-1-X OMEs

For property and engine testing, larger quantities of fuel were required. P-1-P and B-1-B could be acquired by the barrel and tested as is, or extended to longer chains as described in the following section. iB-1-iB was tested only for properties, and little was required. Thus for the general description of the production of other OMEs, iP-1-iP is used as the example, as multi-liter-scale production was required for engine testing. A flow reactor was assembled for this task (depicted in Figure 2.13). The flow reactor was built in house, consisting of an Eldex piston pump and a 3/4 inch stainless reactor tube in a split tube furnace. The reservoir, tubing,



Figure 2.13: Flow reactor setup

and pump piston housing were heat-traced to prevent crystallization of trioxane in the system. The reactor itself was filled with 15g Amberlyst 15 catalyst, in 3 layers separated by glass wool (this makes the system easier to clean and replace catalyst, and should not have any effect on the reactions), as the B-1-B testing indicated that of the four tested catalysts, this was superior for OME production. Figure 2.14 demonstrates the full process, using iP-1-iP as a representative OME.

Production of OMEs for testing was performed using the Pathway 2 methods as described in reactions R2.2.1-R2.2.3. The ratio of trioxane to alcohol was kept at the stoichiometric value, with reactants being prepared by mass (for trioxane) and volume (for the alcohol) in 1 L batches to be added to the reactant vessel as needed. Using iP-1-iP as an example, this synthesis produces a mixture of iP-1-iP, water, and unreacted iPrOH and trioxane. For the conditions selected (80 °C in a flow reactor with 15 g Amberlyst 15 catalyst, approximately 0.64 min^{-1} space velocity), the product mixture is described in Table 2.5. While the mass fractions are dependent on the alkyl groups, the mole fractions provided in this table are reasonably representative of the synthesis in the flow reactor with other alcohols. The hemiacetal is not observed and is expected to

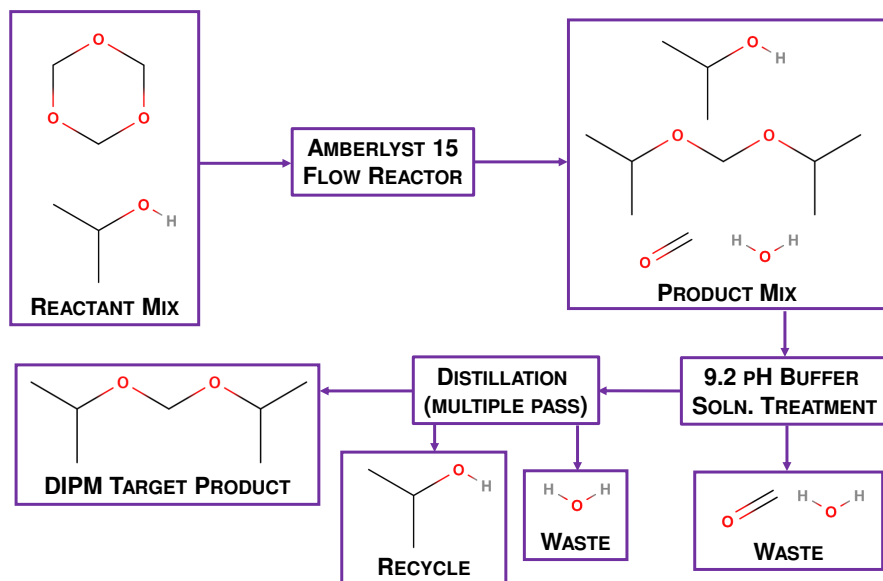


Figure 2.14: iP-1-iP synthesis method, as a representative of the full process required to synthesize and isolate an OME from alcohol and trioxane



Figure 2.15: B/R Instruments 36/100 spinning band distillation column

Table 2.5: Mass and molar yields of iP-1-iP production reaction at 80°C and 0.64 min⁻¹ space velocity over Amberlyst 15 acid catalyst

Component	CH₂O	H₂O	i-C₃H₇OH	C₃H₇OCH₂OC₃H₇
Mass %	11.2	5.2	45.1	38.3
Mole %	22.0	17.0	44.0	17.0

be consumed completely in the reaction. As a GC/FID was used for quantification, where concentrations are calculated using the effective carbon number method [69], only iPrOH and iP-1-iP could be observed; the remaining components were calculated via stoichiometry. Extended oxymethylene chains can be formed in acidic environments with a formaldehyde source given sufficient time to reach equilibrium [8], however, negligible chain growth is observed at these conditions.

The presence of unreacted formaldehyde and/or trioxane or paraformaldehydes, as well as water and unreacted alcohol, requires additional treatment steps for the fuel to be ready for later use. Before separation, the product mixture was treated with a buffer solution. Collaborators at NREL provided the specifications for this buffer solution; its purpose is to simultaneously neutralize the acidity of the product mix (pH = 5 as measured via test strips) and dissolve out water and formaldehyde from the mixture. The buffer solution consists of 1 L of purified (ASTM Type II or better) water mixed with 0.764 g sodium bicarbonate and 0.095 g sodium carbonate. This is mixed 1:1 by volume with the product mixture for several minutes (the products are to a greater or lesser extent immiscible in water, so vigorous shaking by hand was found to be more effective than stirrers or other mechanical methods) and then placed into a separation funnel to split into phases. As will be highlighted later, nearly all OMEs other than heavy M-n-M are lighter than water, so the lower phase is the water phase and is removed and disposed of. In cases where the alcohol is completely miscible in water, this buffer solution treatment also serves to extract a large portion of the alcohol. Specifically for iP-1-iP, the affinity of iPrOH for dissolving in water was much higher than in iP-1-iP, and so after just two buffer solution treatments, the amount of iPrOH was found to be an order of magnitude lower than the product mix directly out of the reactor. This treatment is performed a total of three times; fewer than

three tended to leave enough paraformaldehyde and/or trioxane to foul the distillation column. Following the buffer solution treatment, purification was performed in a B/R Instruments spinning band distillation column, operated typically under vacuum with a Teflon band providing 200 maximum theoretical plates, per manufacturer specifications. For very high temperature distillations (>225°C), a stainless steel band with 36 theoretical plates was required. Using atmospheric equivalent temperature methods, the cut temperatures under vacuum were selected and the column performed automatic cut separation. A more detailed description of the operation of this system is provided in Appendix B.

2.2.2 Methods for Chain Growth of OMEs

Chain growth of the OMEs is performed in the flow reactor over Amberlyst 15 catalyst, determined above to be best catalyst for use with OMEs, using trioxane as a formaldehyde source. All oligomerization reactions were performed at a 1:1 mol ratio of X-1-X basic OME to formaldehyde (3:1 OME:trioxane). When possible, the reactor was held at 80°C +/- 3°C, although for E-n-E oligomerization the temperature was lowered to 70°C to ensure that temperature fluctuations would not result in the mixture boiling in the feed tube due to the low boiling temperature of E-1-E. Reaction R3 shows the general process, using B-n-B as an example.



2.2.3 Results

Under these conditions, the mixtures were able to achieve an equilibrium yield of various chain lengths as described below. Testing with B-n-B indicates that the time on catalyst is long enough that changes in flow rate did not significantly affect yield; the only observed change with lower flow rates (longer time on catalyst) was an increase in the production of the associated alcohol due to decomposition of X-1-X to X-OH, which was observed to be present in low quantities at all flow rates. At a nominal flow rate of 8 mL/min, the yields are as shown in Figure 2.16 and Figure 2.18. The mean MW of the E-n-E mixture is 120.2 g/mol, with 10.2 mol%

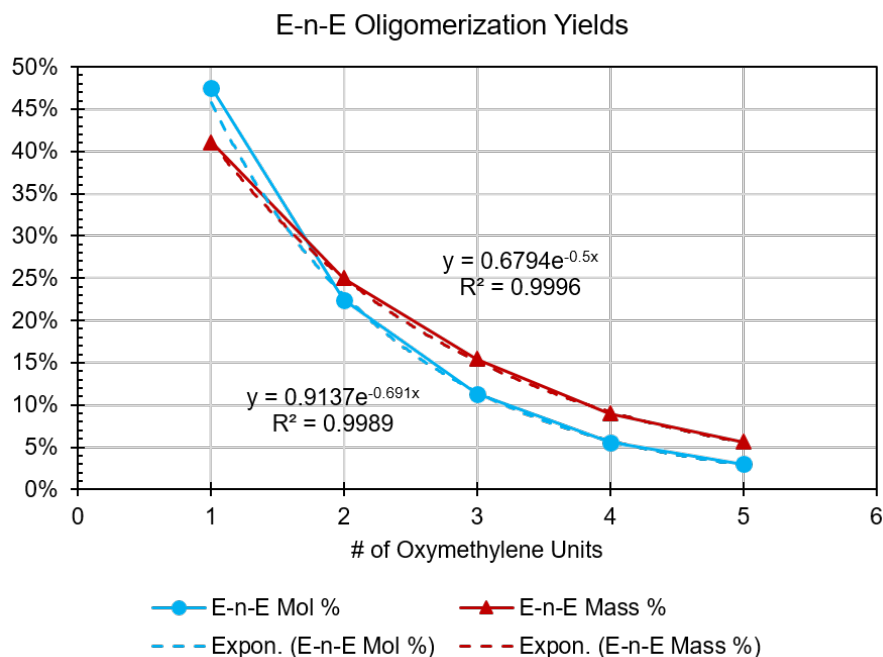


Figure 2.16: Oligomerization yield of 3 mol E-1-E : 1 mol trioxane over Amberlyst 15, 70°C, 8 mL/min

/ 3.9 mass% of ethanol. This indicates a mean oligomerization length of E-1.63-E. For P-n-P, the mean MW is 147.8 g/mol with 5.5 mol% / 3.7 mass% propanol, and a mean oligomer length of P-1.65-P. For B-n-B, the mean MW is 177.2 g/mol with 6.8 mol% / 2.8 mass% butanol, and a mean oligomer length of B-1.70-B.

For engine testing and blending with diesel, a 200°C - 305°C distillation cut has been identified as the desired blendstock; this cut has superior properties and the volatility better matches the typical distillation curve of diesel (Figure 2.19). The composition of this cut is provided below in Figure 2.20. Negligible butanol remains in this distillation cut. Approximately 95% by mass of this cut lies between 220-300°C boiling temperatures, appropriate for diesel.

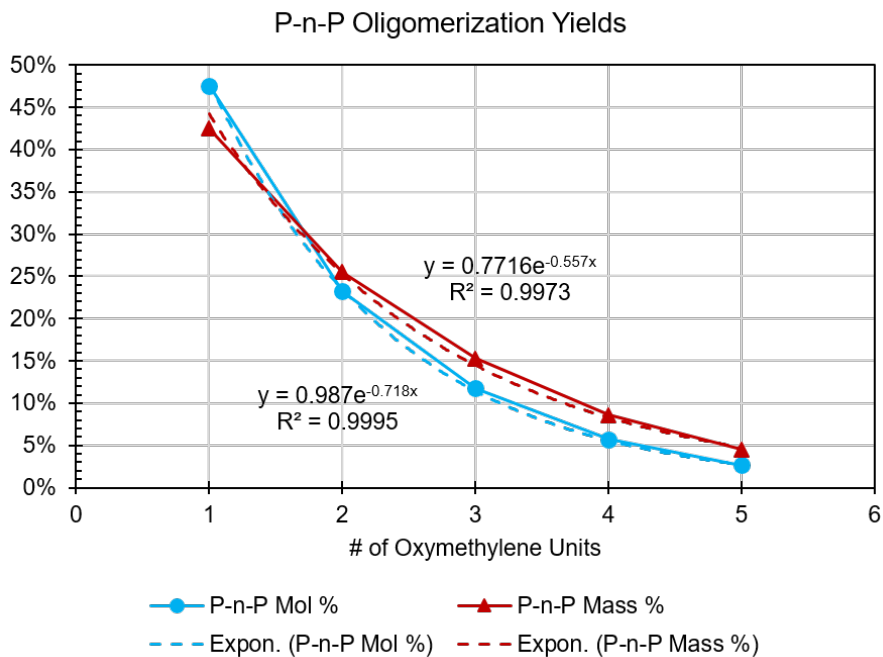


Figure 2.17: Oligomerization yield of 3 mol P-1-P : 1 mol trioxane over Amberlyst 15, 80°C, 8 mL/min

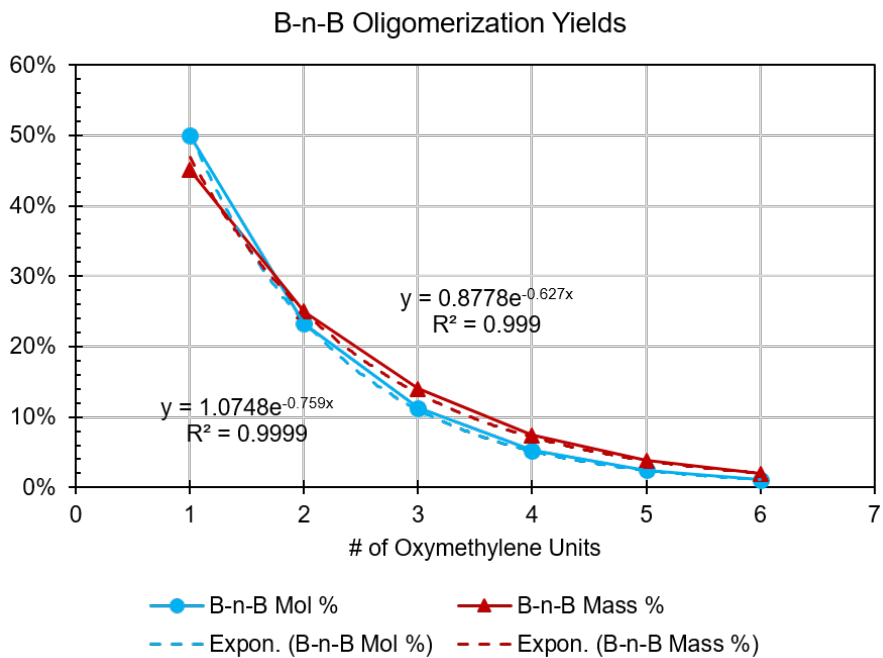


Figure 2.18: Oligomerization yield of 3 mol B-1-B : 1 mol trioxane over Amberlyst 15, 80°C, 8 mL/min

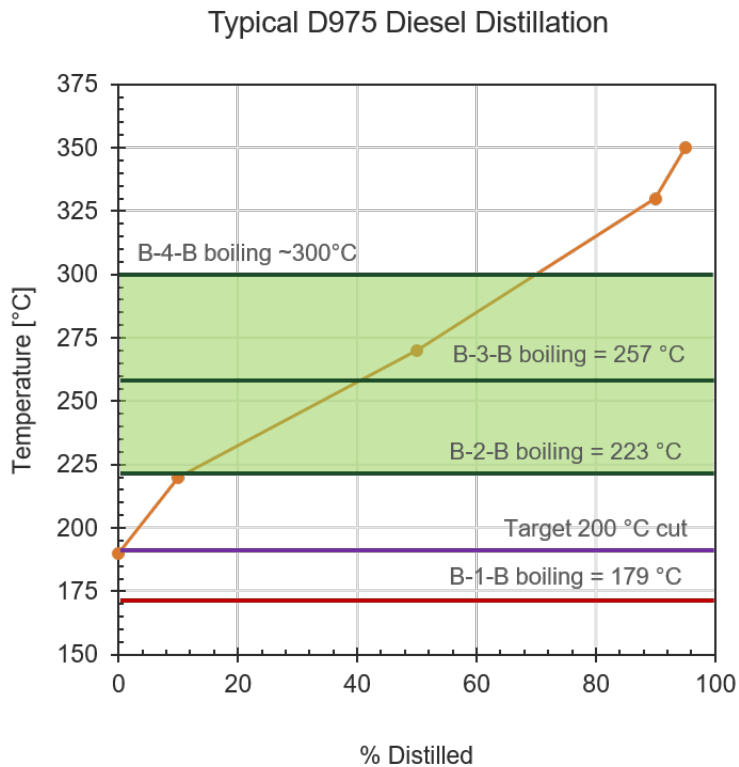


Figure 2.19: Typical D975 distillation curves with boiling points of some B-n-B compounds (see Chapter 3; B-4-B is estimated from trend)

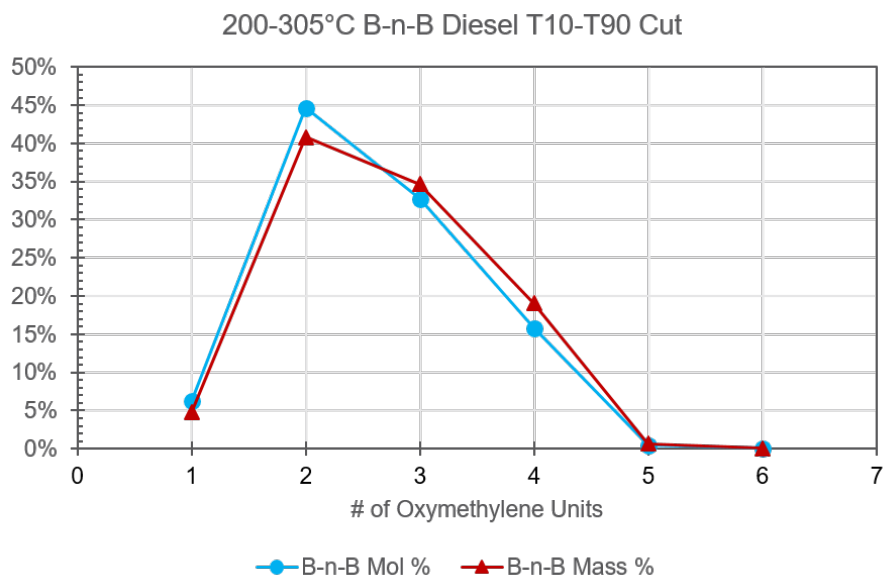


Figure 2.20: Composition of 200-305°C cut of B-n-B oligomerization products

Chapter 3

Determination of Fuel-Relevant Properties of OMEs

Much of the content of this section has been published in the ACS Energy & Fuels journal as “Fuel Properties of Oxymethylene Ethers with Terminating Groups from Methyl to Butyl”, DOI: 10. 1021/acs.energyfuels.2c01414. Reprinted with permission from *Energy Fuels*. Copyright 2022 American Chemical Society.

3.1 Methods

3.1.1 Fuels Used

The OMEs tested in this study are a combination of commercially available, and synthesized in-house. All methyl-terminated OMEs were acquired commercially. M-1-M was purchased from Fisher Scientific and Sigma Aldrich, purity >98%. M-2-M was purchased from AstaTech Inc., purity >97%. M-3-M through M-5-M were acquired as a mixture from ASG Analytik-Service GmbH, and was distilled in-house to purity >95%. E-1-E was purchased from Fisher Scientific and Sigma Aldrich, purity >98%. P-1-P was provided as a sample without charge by Lambiotte & Cie, purity >97%. B-1-B was purchased from Fisher Scientific and Sigma Aldrich, purity >98%. E-2-E, E-3-E, P-2-P, P-3-P, B-2-B, and B-3-B were synthesized via oligomerization of the appropriate X-1-X with trioxane, as described above in Section 2.2.2 and distilled to purity >95%. iP-1-iP and iB-1-iB were synthesized from trioxane and the appropriate iso-alcohol over Amberlyst 15 catalyst as described in Section 2.2.1 and distilled to purity >95%.

3.1.2 Testing Methods

For this segment of the study, several properties were measured for the matrix of OME variations. For some properties, ASTM standard methods were available, however, a number did not have ASTM standard methods available, or the available methods were not designed to handle the range of values encountered in the testing. As much as possible, each test was attempted

to be performed on all of the desired molecules; however, due to limited quantities of some of the more difficult molecules to isolate, some tests were performed only on a subset in order to show the likely trends.

For the ASTM standard methods, the following tests were performed:

- Indicated Cetane Number (ICN), ASTM D8183 [70]. This method is certified in the range of $35 < ICN < 85$, and while it can measure results outside this range, the accuracy is not guaranteed in the standard. Work by Abel et al. has shown that this method has good agreement with other CN measurement standards in normal diesel ranges, and that only for extremely high or low reactivity fuels do the several common methods start to diverge [71]. These tests were performed in a Seta Analytics Advanced Fuel Ignition Delay Analyzer (AFIDA).
- Lower Heating Value (LHV), ASTM D240 [72]. Note that this method directly measures the higher heating value; LHV can be calculated via stoichiometry and the known heat of vaporization of water. These tests were performed in an IKA C200 calorimeter.
- Flash Point (FP), ASTM D93A [73]. These tests were performed in an Anton-Paar PMA4 closed-cup flash point tester. This method was not able to process flash points below ambient conditions, and so some lighter OMEs could not be safely tested.
- Density and Viscosity (ρ and ν), ASTM D7042 [74]. Measurements were conducted over a range of temperatures from 20-100°C where possible. These tests were performed in an Anton-Paar SVM-3000 viscometer.
- Vapor Pressure, ASTM D6378 [75]. From this data, a curve-fit was applied to calculate Antoine equation coefficients. These tests were performed in a Grabner Instruments VPXpert-L vapor pressure tester.
- Oxidative Stability, ASTM D7545 [76]. These tests were performed in a Petrotest PetroOXY device as 20 vol.% blends in tridecane to simulate likely blending conditions.

For non-ASTM test methods, the following tests were performed:

- Yield Sooting Index (YSI)
- Water Solubility (WS)
- Boiling Point (BP)
- Seal material compatibility

YSI characterizes the sooting propensity of a fuel based on the amount of soot formed when the test compound is doped into the fuel of a methane/air nonpremixed flame [77, 78]. The raw soot concentrations are rescaled relative to two endpoint species to produce an index analogous to an octane number or a cetane number. For the B-n-B OMEs, the standard methodology was used: dopant mole fraction = 1000 ppm, upper endpoint = toluene (YSI \equiv 170.9), and lower endpoint = *n*-heptane (YSI \equiv 36.0) [79]. However, these parameters were changed for the other OMEs to accommodate their very low sooting tendencies [80]. In particular, the dopant mole fraction was raised to 3000 ppm to increase the absolute soot concentrations, *n*-heptane was switched to the upper endpoint, and water (YSI \equiv 0.0) was adopted as the lower endpoint to minimize extrapolation of the measured YSIs outside of the endpoint range.

Water solubility was measured in a HP 5890 Series II gas chromatograph with a flame ionization detector (GC-FID) in a 30 m Restek Rtx-Wax column, 0.25 mm diameter with 0.25 μ m film. As water cannot be accurately measured in a GC-FID device, a relative response ratio (RRR) method was used. The target OME was blended with 99% ethanol (*n*-propanol was used for the iP-1-iP case due to simultaneous elution of ethanol and iP-1-iP) at known masses after drying over MS4Å molecular sieves, and the responses recorded:

$$RRR = \frac{area_{ethanol}/mass_{ethanol}}{area_{OME}/mass_{OME}} \quad (3.1)$$

From here, the OMEs were blended with Type I deionized water in individual vials (five samples per OME), shaken vigorously, and left to diffuse to equilibrium for 72 hours. The water

layer was extracted, added to clean vials and the mass recorded, then a known mass of ethanol added. This mixture was tested in the GC-FID, and from the known mass of ethanol and measured response areas, the mass of OME can be calculated. From here, the mass of water is the remainder of the measured mass of OME/water blend, and water solubility in g/g is calculated:

$$mass_{OME} = RRR * \frac{area_{OME}}{area_{ethanol} / mass_{ethanol}} \quad (3.2)$$

This method provides good coefficient of variance (CoV, <5% for most samples), but the very low solubility of butyl-terminated OMEs resulted in higher CoV (approximately 15%) as the samples used masses of OME and ethanol only one order of magnitude higher than the resolution of the balance used. This method was verified with n-pentanol to within 2% of literature values (22.1 g/L vs 22.5 g/L [81]).

Boiling points were not measured directly, but calculated from reduced pressure boiling points during purification. The reduced pressures were converted to atmospheric equivalents using the Atmospheric Equivalent Temperature calculation described in ASTM D1160 [82].

Material compatibility was tested on small (approximately 1 mm x 10 mm x 25 mm) coupons of the selected materials submerged in the OME fuels. Four representative materials were tested – silicone rubber, nitrile rubber (NBR), and fluoroelastomer (FKM), which represent a number of common flexible seal materials, and poly-ether ether ketone (PEEK), a hard polymer sometimes used as a valve seat material. Polytetrafluoroethylene (PTFE) is one of the most common chemical-resistant hard sealing and valve seat materials, but it has been shown in literature to be resistant to OMEs [36] and so PEEK was selected as an interesting alternate material. Two coupons of each material had the mass taken before immersion, then at 24, 48, 72, and 144 hours of exposure to test for fuel absorption, and then again after drying in a fume hood for 24 and 48 hours to test for any permanent damage. When possible, the OME sample was unchanged, but some of the volatile OMEs required replenishing during the measurements to ensure the samples remained fully submerged.

3.2 Results and Discussion

3.2.1 Indicated Cetane Number

ICN was measured as the average of two tests due to the larger quantity of fuel required (approximately 40 mL per test). For all fuels, 2000 ppm of Infineum R655, a lubricity additive, was mixed with the fuel to ensure proper injector operation. Tests with P-1-P and B-1-B without the lubricity additive showed negligible (<0.3) change in ICN due to this additive. The values are presented in Table 3.1. On-road diesel fuels in the US are typically ICN>40, with Texas requiring ICN>48 and California requiring ICN>53. The EU requires ICN>51.

Table 3.1: Indicated Cetane Number of various OMEs

End Group	Number of CH ₂ O Units				
	1	2	3	4	5
Methyl	25.6	56.1	64.0	71.1	85.2
Ethyl	41.1	60.3	59.4		
Propyl	53.2	59.3	66.1		
Butyl	76.3	76.9	76.0		
iso-Propyl	11.2				
iso-Butyl	53.2				
Typical Diesel	>40				

Based upon these criteria, it is found that M-2-M and longer methyl OMEs, and all ethyl, propyl (except iP-1-iP), and butyl OMEs meet the minimum US requirements, and for maximum compatibility, M-2-M and higher, E-2-E and E-3-E, and all propyl (except iP-1-iP) and butyl OMEs are the best candidates. Larger alkyl groups are less sensitive to the length of the oxymethylene chain on ICN, up to the point where the ICN of butyl-terminated OMEs appears entirely independent of the number of oxymethylene units. The kinetics of extended-alkyl OMEs are a new frontier in combustion chemistry; some recent works by Kroger et al.[83], Jacobs et al. [47], and Li et al. [46] have considered the kinetics of E-1-E, but no detailed chem-

ical studies of larger extended-alkyl OMEs have been published. In a later section, this work considers ignition behavior of E-1-E, E-2-E, P-1-P, and iP-1-iP in a rapid compression machine, wherein it is hypothesized that the additional sites available for RO₂ pathways on the longer alkyl groups such as propyl have significant effects on ignition, which may cause the decreased effect of chain length as alkyl groups are extended. Understanding the full causes of these ignition behaviors will require significant future study in fundamental theory and experiments.

Of particular note are the behaviors of the iso-OMEs, iP-1-iP and iB-1-iB. These have significantly lower ICN than their linear counterparts P-1-P and B-1-B, by 79% and 30% respectively. This is not an entirely unexpected result; for example, *n*-octane has a CN of approximately 65 (depending on the exact measurement method), while its branched counterpart iso-octane has CN approximately 17 [84]. While detailed chemical mechanisms have not been developed for any propyl- or butyl-terminated OMEs, work on methyl- and ethyl-terminated OMEs indicates that RO₂ chemistry remains an important step in the ignition of these fuels [46, 47, 83], and thus similar effects on inhibition of RO₂ pathways via branched structures are to be expected. While ICN cannot be directly converted to either form of octane number (RON or MON), it is clear that many fuels with high octane numbers have low cetane numbers; the ICN of iP-1-iP is similar to that of iso-octane, and this may warrant investigation of iP-1-iP as a potential gasoline, rather than diesel, additive.

In the corrigendum to their 2016 analysis of M-n-M and E-n-E OMEs, Lautenschütz et al. review cetane numbers, also using an AFIDA device [30]. We find lower ICN for all comparable OMEs than Lautenschütz, with an average difference of 13% lower ICN; the least difference is in the E-2-E measurement (4.5% lower) and the highest in M-2-M (21% lower). Drexler et. al. [31] tested E-1-E, P-1-P, and B-1-B in an AFIDA; we find similar results to this work, where the highest difference is a 3.2% higher ICN for P-1-P. In either case, the conclusions are similar – most OMEs other than M-1-M, and in some jurisdictions E-1-E, meet diesel requirements for reactivity.

In the literature, neat OMEs as well as OMEs blended with diesel fuel have been tested [32]. Here ICNs were measured for a representative high-ICN OME, B-1-B, blended volumetrically with a certified diesel, ICN=40.7, in increments of 10 volume % (Figure 3.1). Due to the similar densities of B-1-B and diesel, this is essentially equivalent to a mass ratio blend as well. It is observed that the ICN of the mixture is nonlinear with volumetric blending; the presence of B-1-B shows an antagonistic effect on mixture ICN resulting in a lower ICN than would be predicted by linear blending rules; this is in agreement with existing literature on ether blending effects in distillate fuels [85]. The maximum deviation from the linear blending rule is 6.3%, indicating that while the presence of the ether has some negative effect, it is insufficient to overcome the ICN benefit of the high-reactivity OME.

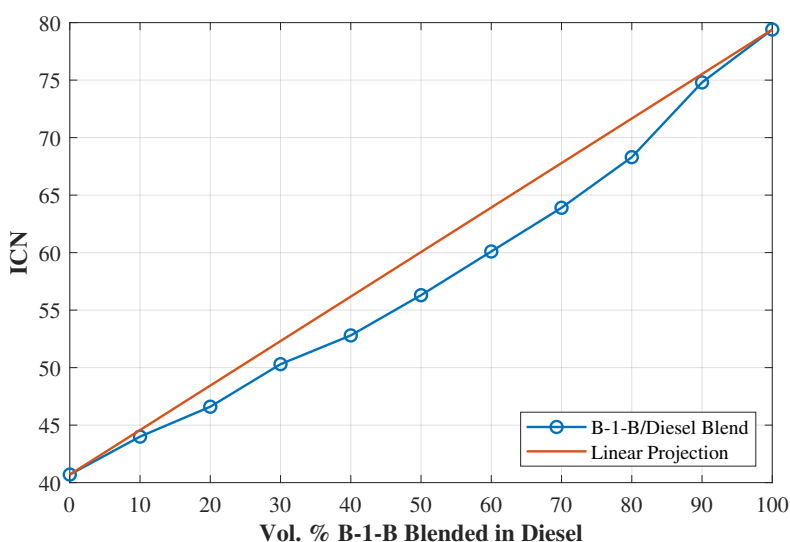


Figure 3.1: Effect of varying B-1-B blending ratio in diesel (ICN=40.7) on ICN of mixture, compared with a linear blending assumption.

3.2.2 Lower Heating Value

LHV was not measured directly; the calorimeter used (IKA C200) combusts a known mass fuel sample in an oxygen environment and measures the change in temperature of a water bath to determine energy released. As the water formed from combustion will condense when

cooled, this method measures the higher heating value (HHV). For engine operation, LHV is the more applicable measurement as the combustion chamber is maintained at high temperature with very short dwell times, so under typical operation none of the latent heat of the water vapor will be released. Thus, HHV is converted to LHV via the assumption of complete combustion and subtraction of the latent heat of the produced water mass; the results of this analysis are presented in Table 3.2.

$$LHV = HHV - m_{H_2O}(\Delta h_{vap}) \quad (3.3)$$

ASTM D975 and EN590 diesel standards do not specify a minimum acceptable value for LHV or HHV of diesel; however, typical diesels have $LHV > 42$ MJ/kg [86], and while biodiesel LHV will depend in part on the oxygen content, some traditional biodiesels have been found to have LHV between 37 and 40 MJ/kg [86, 87]. Synthetic diesels from processes such as Fischer-Tropsch or hydrotreatment of bio-oils may have much higher LHVs, up to 49 MJ/kg [88]. The high oxygen content of OMEs results in significantly lower LHVs than traditional diesels, a weakness noted in prior work [30]. OMEs with extended alkyl groups reduce the oxygen:carbon ratio and thus should produce higher LHVs, and one would further expect longer oxymethylene chain OMEs to produce lower LHV than their shorter counterparts.

Table 3.2: Lower Heating Value of various OMEs [MJ/kg]

End Group	Number of CH ₂ O Units				
	1	2	3	4	5
Methyl	23.2	21.0	20.0	19.3	18.8
Ethyl	28.8	25.9	24.1		
Propyl	32.0	29.0	27.0		
Butyl	34.1	31.2	29.2		
Isopropyl	31.4				
Isobutyl	33.7				

These results are consistent with expectations; higher alkyl groups produce higher LHV, and longer oxymethylene chains produce lower LHV. There is a diminishing effect on the reduction in LHV per oxymethylene unit as the ratio of oxygen:carbon approaches unity with longer chains. The iso-OMEs diverge again from their linear counterparts, but only slightly. This is also consistent with alkane behavior, where LHV of branched molecules is slightly reduced in comparison to linear variants [89]. The reported values here for M-n-M, E-n-E, P-1-P, and B-1-B are in good agreement with literature, [30, 31, 90, 91] with a maximum difference of 4.9% higher LHV reported here for E-1-E compared to measurements from Drexler et al. [31] In our data, an average coefficient of variance (CoV) of 1.2% is found, with M-1-M showing the highest CoV of 4.6%.

None of the tested OMEs show what could be considered “high” LHV; even the highest tested value, for B-1-B, is still approximately 3 MJ/kg less than many typical biodiesels [86]. For maximizing energy content, we recommend usage of OMEs with as long of terminating alkyl groups as other requirements may permit.

3.2.3 Yield Sooting Index

Smoke point measurements by Tan et al. [92] show that methyl-terminated OMEs, which contain no carbon-carbon bonds, have negligible sooting tendencies compared to conventional diesel fuel. In contrast, extended alkyl OMEs do contain carbon-carbon bonds, so they would be expected to have higher sooting tendencies, which diminishes one of the most important attributes of OMEs as alternative diesel fuels. One of the main objectives of this work is to quantify the trade-off between sooting tendency and the desirable properties of extended alkyl OMEs (e.g., higher LHV, lower water solubility). The smoke points of the OMEs are outside the measurement limits of the ASTM D1322 standard and cannot be determined directly

[93]. However, the YSI approach used in this study has a much wider dynamic range and values could be measured for all the neat OMEs.

Table 3.3: Yield Sooting Index of various OMEs

End Group	Number of CH ₂ O Units				
	1	2	3	4	5
Methyl	6.6	5.2	0.5	-2.5	-4.8
Ethyl	15.5	13.8	11.9		
Propyl	30.8	25.5	21.3		
Butyl	46.0	42.7	37.8		
Isopropyl	38.4				
Isobutyl	52.2				
Typical Diesel	>200				

Table 3.4: YSI/LHV of various OMEs [1/(MJ/kg)]

End Group	Number of CH ₂ O Units				
	1	2	3	4	5
Methyl	0.284	0.248	0.025	-0.130	-0.255
Ethyl	0.538	0.533	0.494		
Propyl	0.963	0.879	0.789		
Butyl	1.35	1.37	1.29		
Isopropyl	1.22				
Isobutyl	1.55				
Typical Diesel	~4.8				

Table 3.3 lists the measured YSIs and Table 3.4 lists the ratios of the YSIs to the LHV's reported in the prior section. YSI uncertainty is +/- 7%. YSI quantifies the amount of soot formed per mole of fuel, whereas YSI/LHV indicates the amount of soot produced per unit of fuel energy,

which is the more engine-relevant quantity. The YSIs demonstrate that all the OMEs significantly reduce soot compared to diesel fuel: the sootiest OME, iB-1-iB, decreases it by a factor of 3.8 while the least sooty OMEs, M-4-M and M-5-M, decrease it by an effectively infinite ratio since they have negative YSIs. These negative YSIs are discussed in more detail elsewhere [80]; in short, they occur because M-4-M and M-5-M produce virtually no soot and instead decompose to large quantities of formaldehyde (CH_2O), which suppresses soot formation from the methane background fuel in the YSI flames to a total soot fraction below that observed in the zero YSI case. The results in Table 3.4 show that the reductions in YSI/LHV are smaller, but still significant. For example, whereas iB-1-iB reduces YSI by a factor of 3.8, it reduces YSI/LHV by a factor of 3.1. This observation demonstrates that the OMEs reduce soot even when accounting for the larger amount of fuel required to produce a given amount of energy.

The root of the improvements in soot per unit energy stem from the reduction in C–C bonds and replacement with C–O bonds. The Hydrogen Abstraction Carbon Addition mechanism (HACA) is the commonly accepted mechanism by which soot is formed in flames [94], and is defined by decomposition of hydrocarbons down to acetylene or other alkynes, followed by formation of aromatics and growth to polycyclics with acetylene addition. After polycyclic aromatics grow sufficiently large, they then begin to agglomerate into particles. Traditional methyl-terminated OMEs prevent this process almost entirely by removing all C–C bonds, preventing the formation of acetylenes.

In his dissertation, Zhu discusses the measurements and simulations of M-1-M, and notes that the negative YSIs are indeed an artifact of dilution; M-1-M will produce methyl radicals, some amount of which will recombine to form ethane and permit the HACA process. The formaldehyde in the products is unlikely to further decompose to methylene due to the strong C=O double bond, and is unlikely to contribute to soot production, leaving only methyl radical recombination as the soot source in M-n-M flames [95]. Larger end groups will provide some additional C–C bonds for HACA soot formation, however, C–O bonds still contain energy for combustion while preventing this mechanism as discussed above. Zhu provides basic mecha-

nisms for several of the non-methyl OMEs, many of which include ethylene, propylene, or other C=C double-bonded decomposition products which are intermediates for acetylene and soot production [95].

3.2.4 Flash Point

Flash point (FP) is an important factor in the safety of handling fuels; while gasolines typically have FP well below ambient and are treated as flammable liquids, diesel fuels typically have FP $>52^{\circ}\text{C}$ ($>55^{\circ}\text{C}$ in the EU) and are classified as combustible liquids [96]. As documented by Härtl et al. and Lautenschütz et al. [30, 90], smaller OMEs such as M-1-M and E-1-E have FP below or close to this requirement, but the most commonly studied OMEs (M-3-M and higher) will meet this requirement.

Table 3.5: Flash Point of various OMEs [$^{\circ}\text{C}$]

End Group	Number of CH ₂ O Units				
	1	2	3	4	5
Methyl	<20 ^a	<20 ^a	56.4	85.6	116
Ethyl	<20 ^a	35.5	69.4		
Propyl	31.7	66.5	91.0		
Butyl	58.6	89.6	114		
Isopropyl	21.3				
Isobutyl	49.4				
Typical Diesel	>52				

^aFlash point too low to safely test in PMA4

As shown in Table 3.5, FP appears to be a significant weakness in compatibility of OMEs with diesel; about half (M-3-M and higher, E-3-E, P-2-P and higher, and B-1-B and higher) meet this requirement, while others do not. Our measurements have an average coefficient of variance (CoV) of 0.98%, with B-1-B showing the highest CoV of 1.8%, for five tests performed for each

fuel. The reported values for M-n-M and E-n-E are in good agreement with Lautenschütz’s work, with a maximum deviation of <1% higher for M-3-M [30]. We also find comparable FP to Drexler et al. [31] for P-1-P and B-1-B, with <1% difference. Some of these fuels had FP too low to safely test in the PMA4 device, which is not natively equipped to test FP below ambient temperatures, and while some cooling of the test cup is possible, a different device with native cooling capability may be required for testing of low-FP OMEs; we note that Lautenschütz et al. report FP values for M-1-M and E-1-E of -32°C and -5°C respectively [30] and Deutsch et al. report a FP of 16°C for M-2-M [91], below the safe testing limits of the methods used here.

3.2.5 Density and Viscosity

Physical properties of the liquid fuel will have significant effects on the behavior of the spray in the fuel injector for a CI engine; the influential work of Lefebvre on sprays indicate that ρ and ν are of high importance for spray development [97]. The effect of biodiesels on the performance of CI engine injectors has been a matter of concern due to typically higher ρ and ν ; as reviewed by Algayyim et al., many studies have been conducted which find that typical biodiesels produce sprays with greater penetration and larger diameter droplets, hindering evaporation due to lower area:volume ratios [98]. Further, some work suggests that larger droplets may increase soot formation [99]. CI engines are designed around combustion of a particular ideal fuel spray, so rather than preferring some minimum (e.g. YSI) or maximum (e.g. LHV), the ideal OME for diesel blending will match as closely as possible to typical diesel values. We present density of the OMEs at 20°C in Table 3.6, and the viscosity at 40°C in Table 3.7 below.

Table 3.6: Density at 20°C of various OMEs [g/mL]

End Group	Number of CH ₂ O Units				
	1	2	3	4	5
Methyl	0.860	0.992	1.03	1.07	1.10
Ethyl	0.829	0.912	0.971		
Propyl	0.834	0.900	0.948		

Butyl	0.837	0.888	0.931
Isopropyl	0.818		
Isobutyl	0.824		
Typical Diesel	0.84-0.87		

Table 3.7: Kinematic Viscosity at 40°C of various OMEs [mm²/s]

End Group	Number of CH ₂ O Units				
	1	2	3	4	5
Methyl	n/a ^b	0.617	0.876	1.32	1.98
Ethyl	0.346	0.652	0.963		
Propyl	0.644	0.949	1.39		
Butyl	0.945	1.32	1.85		
Isopropyl	0.515				
Isobutyl	0.904				
Typical Diesel	2.0-3.2				

^bAt lab ambient pressure (84 kPa), M-1-M will boil at approximately 37°C, so no density or viscosity at 40°C can be measured without a device to maintain the viscometer above ambient pressure

None of the OMEs tested match perfectly with typical diesel for ρ except M-1-M; however, all of the n=1 and n=2 OMEs are very close to diesel and may be good substitutes in this respect. Longer oxymethylene chains produce higher ρ due to higher oxygen content, which helps offset some LHV losses by allowing for more fuel mass per unit volume. Only two tested OMEs, M-5-M and B-3-B, even approached the ν values typically seen in diesels, with most being less than half that of the minimum diesel ν . The average CoV for ρ and ν measurements was less than 0.1% for 3 tests per fuel.

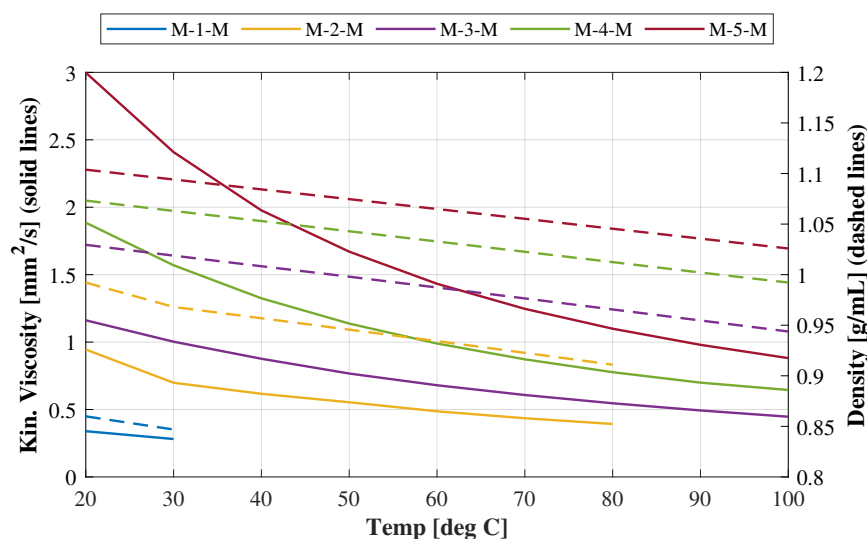


Figure 3.2: Viscosity and density curves of M-n-M OMEs between 20°C and 100°C

In comparison with literature, we find nearly identical ρ measurements to Lautenschütz [30] and Drexler [31], with the largest observed difference as a 1.5% higher ρ for M-2-M[30]. For ν , Lautenschütz et al. measure ν at 25 °C and Drexler et al. measure at 20 °C, while Deutsch et al. measure at 40 °C, as reported in Table 3.7 above. We find good agreement with Deutsch et al. for all values except M-2-M, where we observe a 9.2% higher ν . A temperature sweep was performed for ρ and ν (Figs. 3.2-3.5) with a step of 10°C, so to compare with Lautenschütz et al. we take an average of our 20°C and 30°C values. Acknowledging that ν is nonlinear with temperature, and thus some small error is to be expected from this approximation, we nonetheless find good agreement except for M-1-M and E-1-E, where we observed significantly (16% and 19% respectively) lower ν than Lautenschütz et al. For E-1-E, P-1-P, and B-1-B, we find a 15% lower ν for E-1-E than Drexler et al. [31], but find good agreement (within 5%) for the remaining fuels.

3.2.6 Vapor Pressure

A subset of the OMEs were tested for vapor pressure, however, due to high fuel volume requirements not all were tested. The tested OMEs were M-1-M, M-3-M, M-4-M, M-5-M, E-1-E, P-1-P, and B-1-B. Antoine equation (Eq. 3.4) parameters were calculated for these OMEs and

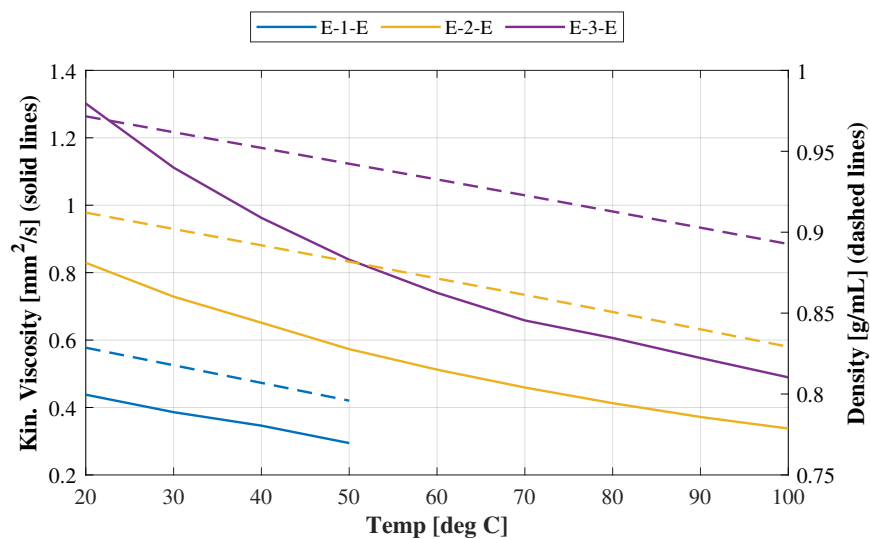


Figure 3.3: Viscosity and density curves of E-n-E OMEs between 20°C and 100°C

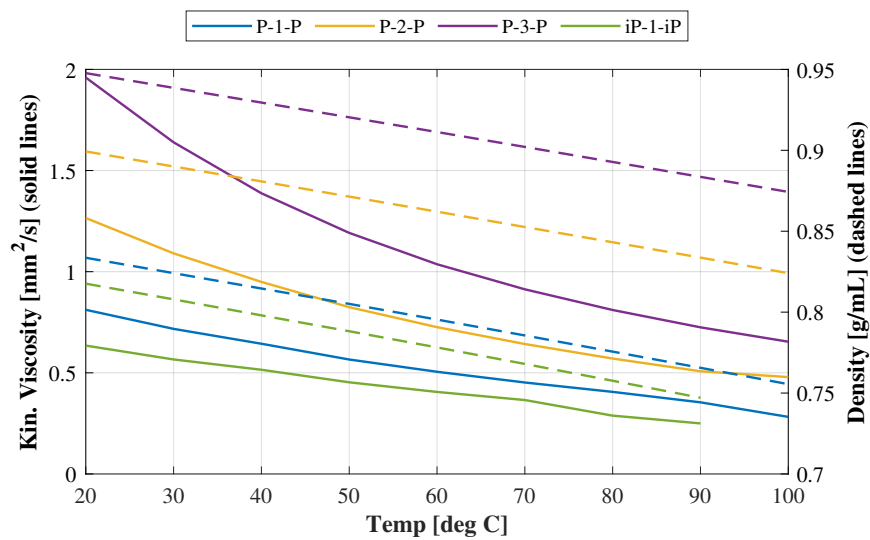


Figure 3.4: Viscosity and density curves of P-n-P and iP-1-iP OMEs between 20°C and 100°C

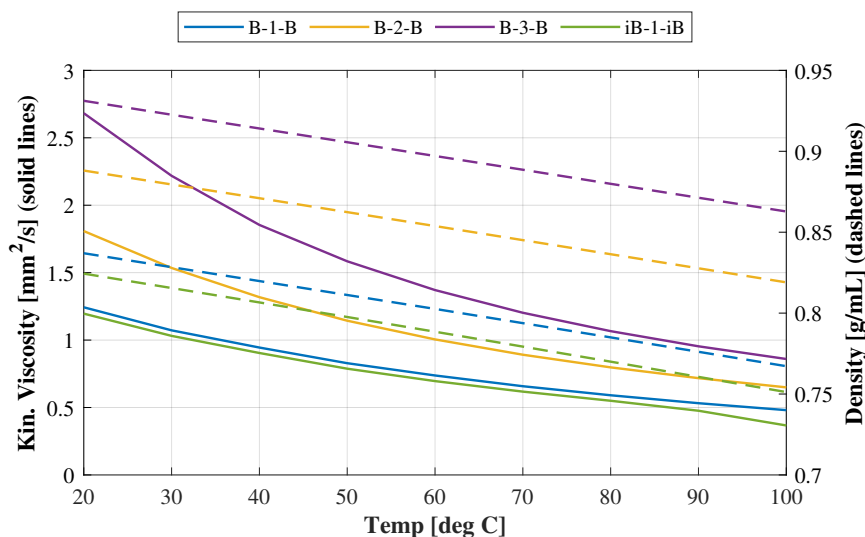


Figure 3.5: Viscosity and density curves of B-n-B and iB-1-iB OMEs between 20°C and 100°C

are presented below; M-1-M and E-1-E have Antoine coefficients provided in the NIST Web-book [100, 101] and produce curves within 5% of our calculated values. The average CoV for five tests per fuel was 5.5%, driven primarily by exceptionally high CoV (29%) for M-5-M (the average CoV for the other tests, excluding M-5-M, was a more reasonable 1.8%). Generally, CoV increased with decreasing volatility. Due to limits of the testing device and the fuels, different temperature ranges were tested, up to either just below the boiling temperature or the device maximum temperature (120°C), and starting at 0°C or a temperature providing above 5 mbar vapor pressure (to prevent damage to the machine due to low vacuum). Coefficients are reported in Table 3.8 as calculated from the curve fit, but we note that the measured values from which these are produced are accurate to 3 significant figures and calculated values from these should be treated as such.

$$\log_{10}(P_{vap}) = A - \frac{B}{C + T} \quad (3.4)$$

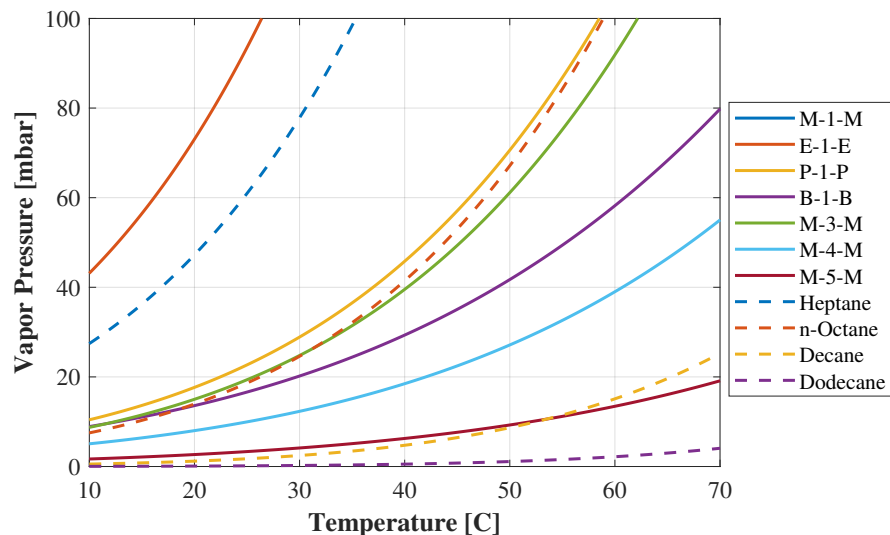


Figure 3.6: Antoine curves of OME vapor pressure, from calculated Antoine coefficients, compared to some typical alkanes (see Table 3.8)

Table 3.8: Antoine equation coefficients for some OMEs [bar, K]

Fuel	Temp Range	A	B	C
	Tested [°C]			
M-1-M	0-35	3.881	991.89	-59.23
E-1-E	0-80	3.995	1201.2	-59.07
P-1-P	20-120	4.762	1920.2	1.598
B-1-B	30-120	3.911	1882.5	32.66
M-3-M	20-120	4.246	1629.4	-24.69
M-4-M	30-120	4.309	2130.2	39.43
M-5-M	50-120	4.142	2301.4	49.54

The vapor pressure of diesel will vary with the various volatile components, so several common alkanes are shown on the plot below (Figure 3.6) using Antoine parameters from NIST [102–104] to provide a point of reference.

3.2.7 Oxidative Stability

The most common test for oxidative stability of biodiesels is the Rancimat test (EN 15751). This test was attempted for oxidative stability, however, the nature of the method caused significant difficulties and was determined to be ineffective for testing OMEs. First and most relevant, the Rancimat test is by nature an open-system test. The oxidation is accelerated by pumping air through a heated fuel sample, and the volatiles (nominally acids) are collected in water, with changes in the conductivity of the water indicating the presence of acids formed from auto-oxidation. As a result of heating to the test temperature of 110°C and simultaneously enforcing a gas flow, many of the OMEs will rapidly vaporize or even boil and be lost – further, as will be discussed in a later section, the water solubility of many OMEs is very high and vapors will contaminate the measuring water. The second problem is the nature of the test, which uses conductivity change of a water sample as a proxy for oxidation. This has been shown to work well for fatty-acid methyl ester biofuels [105], but it was not clear prior to the tests whether the auto-oxidation products of an OME will necessarily ionize or otherwise change the conductivity of the measuring water.

As a result of these difficulties, a different test was used. The Petro-Oxy testing device is often used for gasoline and gasoline additives [106], which makes it more suitable for the OMEs, some which have been shown to have higher volatility. Additionally, it is a closed-system measurement, preventing the vapor losses seen in some initial failed attempts to use the Rancimat method. The Petro-Oxy device subjects a small (5 mL) sample of the fuel to 140 °C under 7 bar of oxygen, and measures the induction time as defined by the time to a 10% reduction from the maximum pressure of the test [76]. Some past work has applied this method to biodiesels in comparison with the Rancimat method and determined minimum equivalent Petro-Oxy induction times [107], proposing that the 8 hour Rancimat induction time required for European biodiesel is comparable to 27 minutes in a Petro-Oxy device, and the US standard of 3 hours is comparable to 17 minutes of Petro-Oxy testing, where longer induction times are indicative of higher oxidative stability. Due to limited equipment availability, only a subset of OMEs were

tested in this device, focusing primarily on larger alkyl groups (E-1-E, P-1-P, P-2-P, B-1-B, B-2-B, B-3-B, iP-1-iP, and iB-1-iB). These were blended at 20 vol% in tridecane to simulate common blending ratios in diesel and allow for higher resolution due to lower concentrations of OME. The induction times for the tests are presented in Table 3.9. GC-MS testing was performed on the oxidized sample to determine the products of the auto-oxidation reaction. Common products included alkyl esters, carboxylic acids, and alcohols. The presence of carboxylic acids indicates that Rancimat tests may be effective for heavier OMEs which can survive the heated open system environment without significant vapor loss.

Table 3.9: Induction times of select OMEs in Petro-Oxy test, 20 vol% in tridecane

End Group	Number of CH ₂ O Units		
	1	2	3
Ethyl	228 min		
Propyl	86 min	91 min	
Butyl	106 min	152 min	174 min
Isopropyl	38 min		
Isobutyl	88 min		
Tridecane	154 min		

A trend is observed with the oxymethylene chain length; longer chains lead to improved stability. However, no clear trend can be seen for alkyl groups – E-1-E is more stable than any of the propyl or butyl OMEs, however, all of the butyl OMEs are more stable than the propyl ones. The iso-alkyl OMEs do show significantly reduced stability in comparison to their linear counterparts. The mechanisms by which this is occurring are unclear and warrant further investigation. All of the tested OMEs, in 20% blends, exceed the biodiesel oxidative stability standards, but it is unclear whether these fuels will exhibit stability issues when tested neat. Single tests were performed for each fuel, and so we refer to the ASTM standard, section 14.1.5,[76] where

the reproducibility R of this method can be calculated as $R = 0.0863X + 1.3772$, to estimate an average R of 10% of the measured values.

3.2.8 Water Solubility

Water interaction with fuels is important for a number of reasons, but most importantly, there are environmental and combustion concerns. A fuel which is highly soluble in water poses risks in case of spillage; it will be significantly harder to separate from water sources due to lack of distinct phases, and there is a risk of fuel becoming dissolved into groundwater in high concentrations and being spread from the spill site. Further, a fuel which can carry high concentrations of water dissolved in the fuel itself, while less of an environmental concern, poses risks to engine and fuel system operation and can reduce the effective LHV of the fuel.

Table 3.10: Water solubility of various OMEs [g OME / kg water]

End Group	Number of CH ₂ O Units				
	1	2	3	4	5
Methyl	481	469	394	338	283
Ethyl	56.0	60.7	52.3		
Propyl	3.16	3.72	3.23		
Butyl	0.215	0.189	0.251		
Isopropyl	9.76				
Isobutyl	6.62				
Typical Diesel	<0.1				

As shown in Table 3.10, the effect of additional oxymethylene units on the water solubility is negligible compared to the alkyl group effect, where increasing the alkyl group by one carbon per side reduces water solubility by roughly an order of magnitude each time. The mean CoV of these data is 6.9%, with B-3-B having the highest CoV at 19%. All of the B-n-B fuels exhibited high CoV due to measurable amounts of the fuels being only one order of magnitude greater

the resolution of the balance used. Of the various properties tested, this one makes one of the strongest cases for the suitability of extended-alkyl (particularly butyl) OMEs for diesel blending. One anomaly is the behavior of iB-1-iB – while iP-1-iP is slightly higher than P-1-P, but within the same order of magnitude, iB-1-iB is an order of magnitude higher in water solubility than B-1-B. This result was sufficiently surprising that the entire series of iB-1-iB was retested with fresh samples, and the same result was found. It is currently unclear what the chemical basis for this significant difference is, and more investigation is warranted.

3.2.9 Boiling Temperature

Boiling temperatures were measured as a necessary result of the distillation process for purification. Distillation was generally performed under vacuum (150 torr, 100 torr, or 30 torr, depending on the lightest component) except for when M-1-M was expected to be present. The equivalent temperature at standard conditions (AET) was calculated using the procedure in ASTM D1160 Appendix A7[82], assuming a K factor of 12 (this value is recommended in the standard unless another value can be clearly established) and using units of torr and °C. A pressure correction A is first calculated from the distillation pressure P , a temperature correction Δt from K and the pressure P , and then the AET calculated from A , T , and Δt :

$$\Delta t = -1.4(K - 12) \log_{10} \left(\frac{760}{P} \right) \quad (3.5)$$

$$A = \frac{5.994295 - 0.972546 \log_{10} P}{2663.129 - 95.76 \log_{10} P} \quad (3.6)$$

$$AET = \frac{748.1A}{(T + 273.15)^{-1} + 0.3861A - 0.00051606} - 273.15 + \Delta t \quad (3.7)$$

The most likely source of error in these measurements is not from average boiling temperatures observed at reduced pressure, which were typically within +/- 1°C, but rather the uncertainty of the K factor. This is recommended in the standard as 12, but differing behavior of

OMEs from typical distillate fuels may require a different K value. As an example, a +/-2 difference in K produces (at 30 and 150 torr reduced pressures, respectively) +/-3.93°C and +/-1.97°C differences (where higher K leads to lower calculated temperature).

Table 3.11: Boiling temperature of various OMEs [°C]

End Group	Number of CH ₂ O Units				
	1	2	3	4	5
Methyl	42	112	161	207	243
Ethyl	88	142	186		
Propyl	141	184	223		
Butyl	179	223	257		
Isopropyl	119				
Isobutyl	164				
Typical Diesel (T10)	200				

The 10% distillation and 50% distillation temperatures (T10 and T50) of diesel fuel vary based on the specific blend but are often around 200°C and 250°C, respectively [86]. From the data in Table 3.11, it is clear that most of the tested OMEs are more volatile than even the low distillation components of a diesel; the only OMEs tested with boiling temperatures above T10 are M-4-M, M-5-M, P-3-P, B-2-B, and B-3-B, and only one tested OME (B-3-B) has a boiling temperature comparable to diesel T50. Consequently, diesels with OME components may experience preferential vaporization effects; effects of this on the combustion characteristics of diesel sprays is worthy of investigation.

3.2.10 Material Compatibility

Due to high required volumes of fuel for the material compatibility, this testing was performed only on a subset of OMEs with n=1. The effect of various chain lengths of M-n-M has been documented in literature [36, 108, 109], so this work focuses on the end group effect. Ad-

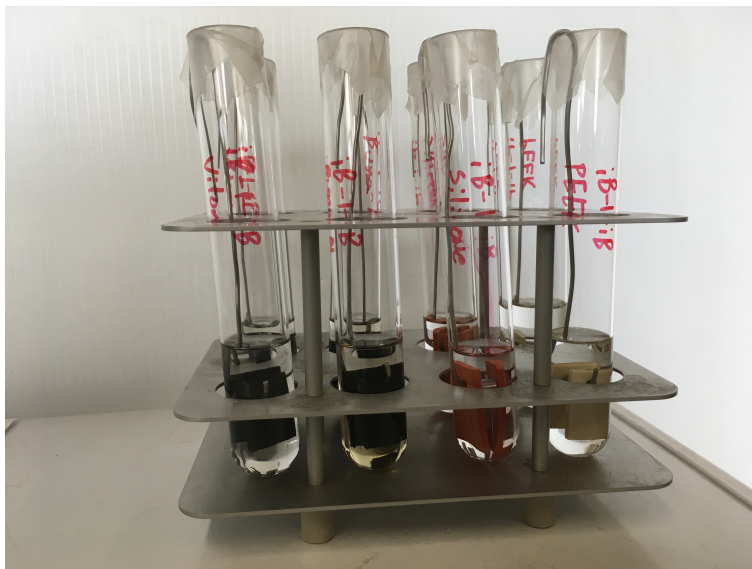


Figure 3.7: Test setup for material compatibility exposure testing

ditionally, there is a wide range of possible sealant materials, and varying properties within categories of material, so it will be necessary for any engine development programs to do in-depth testing of the specifically selected materials. Thus, we present these data as being informative, but not necessarily generalized.

The results of the material compatibility tests are provided in Figure 3.8 and Figure 3.9, where the results are shown as mass increase due to fuel absorption (i.e. a 50% change represents the material absorbing a mass of fuel equal to 50% of the original material), and thus the desired result is to minimize this effect. The largest change in mass (due to fuel absorption) occurred in the first 24 hours (Fig. 3.8), and equilibrium was reached by 72 hours (Fig. 3.9) for all fuels and materials. For most, the change from the first measurement to equilibrium was negligible; only FKM and NBR in M-1-M, silicone in E-1-E, and FKM in iP-1-iP had significant (>5% by mass) changes after 24 hours. These measurements are an average of 2 samples, where the average deviation from the mean is 1.6%, with iP-1-iP having the widest variation at 5.5%.

The largest change in mass (due to fuel absorption) occurred in the first 24 hours, and equilibrium was reached by 72 hours for all fuels and materials. For most, the change from the first measurement to equilibrium was negligible; only FKM and NBR in M-1-M, silicone in E-1-E,

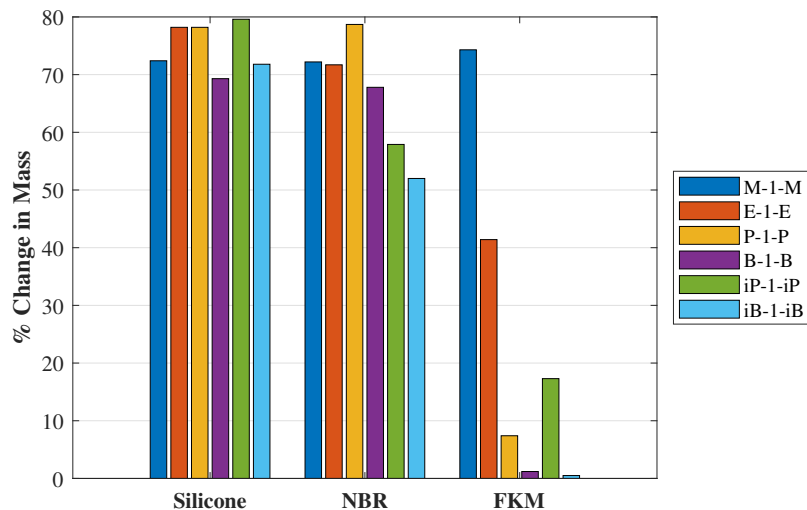


Figure 3.8: Percent change in mass of elastomer sample coupons after 24hr submerged exposure

and FKM in iP-1-iP had significant (>5% by mass) changes after 24 hours. In the plots below, the PEEK samples are not shown for the simple reason that they proved to be highly resistant and did not absorb any fuel for the entire duration of the test.

One of the most important takeaways is the suitability of PEEK as a hard sealing or handling material for OMEs; no absorption was observed for any of the tested OMEs at any duration of exposure. For the elastomers, FKM was the only one which was suitable for use with OMEs, and only for the extended alkyl OMEs - it has worse performance for M-1-M, but shows significant reductions in mass of fuel absorbed as the alkyl group is lengthened. Additionally, it is noted that the common trend observed in most other properties regarding the iso-OMEs, namely that they have somewhat inferior properties to their linear counterparts, is reversed here - iP-1-iP and iB-1-iB had less absorption than P-1-P and B-1-B for NBR and FKM samples, and essentially comparable effects on silicone.

An effect that is difficult to quantify is leaching into the fuels. No apparent change was observed for PEEK, silicone, or FKM, but the NBR sample caused discoloration of all of the OMEs. An example is shown in Figure 3.10. Anecdotally, similar discoloration was observed

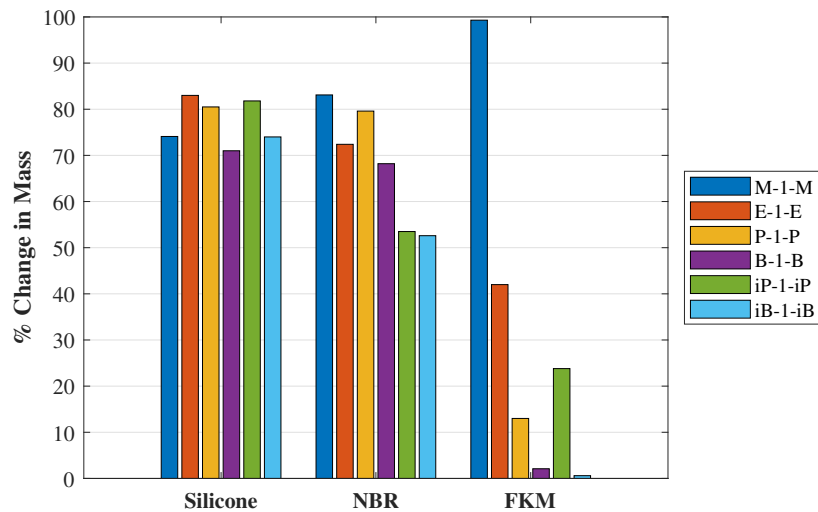


Figure 3.9: Percent change in mass of elastomer sample coupons after 72hr submerged exposure

when a nitrile rubber stopper was used for a flask storing B-1-B, so we believe that this may not simply be a flaw with the specific lot of NBR used in this testing.

3.3 Downselected Blend and Diesel Compatibility

3.3.1 ASTM Diesel Standard Compatibility

One of the major goals of the overarching DoE project is the selection of a blend of OMEs which can reduce the soot production of diesel engines in legacy systems. In order to achieve this goal, we must downselect from the variety of OMEs tested for the best compatibility with current diesel standards, as described by ASTM D975. Table 3.12 describes the properties governed under this standard; each of these is measured using its own ASTM standard.

Considering the properties measured above, and the boiling range described in Section 2.2, we select a 200°C - 305°C distillation cut of B-n-B as the most appropriate for diesel blending. A sample of this was prepared and sent to an external laboratory – FOI Laboratories in Vancouver, WA – for certification under ASTM D975. All properties except lubricity and flash point passed in the initial report, however, a retest of flash point was requested and passed on the second attempt. Equipment failure is suspected in the first test, as the reported flash point was lower



Figure 3.10: Discoloration of iP-1-iP due to NBR leaching

Table 3.12: Properties controlled and limits under ASTM D975 [110], using ULSD 2-D as reference

Property	Governing Standard	Limit Range
Flash Point	D93	>52°C
Water and Sediment	D2709	<0.05 vol%
Distillation Temp., 90% Recovered	D86	282°C - 338°C
Kinematic Viscosity	D445	1.9-41 mm ² /s
Ash Mass Percent	D482	<0.01 mass%
Sulfur ppm	D5453 or D2622	15
Copper Strip Corrosion	D130	No. 3
Cetane Number	D613	>40
Aromaticity, Vol. Percent	D1319	<35 vol%
Cloud Point	D2500	No specified
Carbon Residue	D524	<0.35 mass%
Lubricity	D6079 or D7688	<520 μm
Conductivity	D2624 or D4308	>25 pS/m

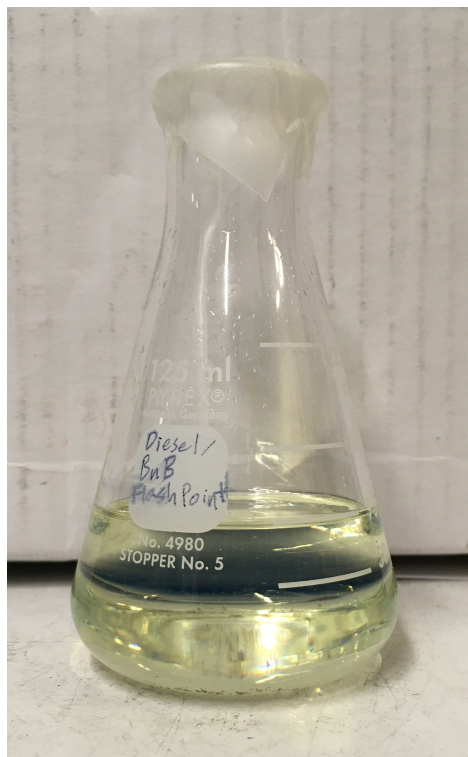


Figure 3.11: B-n-B in diesel sample kept six months for phase separation test

than the flash point of either the certification diesel or the lowest OME component. Lubricity of OMEs, as well as viscosity, is of concern, but may be remedied with lubricity additives. A small sample was kept in a flask for six months to check for phase separation or other miscibility problems. No separation was observed (Figure 3.11). Some sediment is observed in the bottom of the flask, however, this is expected to stem from the diesel rather than OME components, as no sediment was found in the OME-only sample used to make this blend.



Stephen Lucas
 Colorado State: Chemical
 Energy Conversion Lab
 430 N. College Ave.
 Fort Collins, CO 80524
 USA
 509-220-6228
 Sample ID:
 Purchase Order:
 Work Order:
 Package:

ASTM D975 - Full

Sample Taken From:
 Type of Fuel: Diesel
 Sample Collection Date:
 Date Received: July 12, 2022
 Date Released: August 11, 2022
 Component Make:
 Component Model:
 Serial Number:
 Quantity in Tank:
 Tank Capacity:

Test	Limit	Method	Result
Acid Number	report mg KOH/gm max	ASTM D974-08	.04
API Gravity by Hydrometer	report	ASTM D1298-99	31
Ash Content	0.01% wt max	ASTM D482	<.01
Carbon Residue	report % (m/m)	ASTM D189	0.10
Cetane Number	report	ASTM D613	50.6
Cloud Point	report °C	ASTM D2500-99	-21
Conductivity	25 pS/m minimum	ASTM D2624	841
Copper Strip Corrosion	3 maximum	ASTM D130-04	1a
Distillation, 90%	282 - 338 °C	ASTM D86/D2887	305
Flash Point	52 °C minimum	ASTM D93-10	42
ICP Metals-Aluminum(Al)	report in ppm	HL-1158	0
ICP Metals-Antimony(Sb)	report in ppm	HL-1158	0
ICP Metals-Barium(Ba)	report in ppm	HL-1158	0
ICP Metals-Boron(B)	report in ppm	HL-1158	1
ICP Metals-Calcium(Ca)	report in ppm	HL-1158	1
ICP Metals-Chromium(Cr)	report in ppm	HL-1158	0
ICP Metals-Colbalt(Co)	report in ppm	HL-1158	56
ICP Metals-Copper(Cu)	report in ppm	HL-1158	0
ICP Metals-Iron(Fe)	report in ppm	HL-1158	0
ICP Metals-Lead(Pb)	report in ppm	HL-1158	0
ICP Metals-Magnesium(Mg)	report in ppm	HL-1158	0
ICP Metals-Molybdenum(Mo)	report in ppm	HL-1158	1
ICP Metals-Nickel(Ni)	report in ppm	HL-1158	2
ICP Metals-Phosphorus(P)	report in ppm	HL-1158	1
ICP Metals-Potassium(K)	report in ppm	HL-1158	0
ICP Metals-Silicon(Si)	report in ppm	HL-1158	0
ICP Metals-Silver(Ag)	report in ppm	HL-1158	0
ICP Metals-Sodium(Na)	report in ppm	HL-1158	0
ICP Metals-Tin(Sn)	report in ppm	HL-1158	0
ICP Metals-Titanium(Ti)	report in ppm	HL-1158	0

(a) FOI Laboratories ASTM D975 Test Report, page 1

Figure 3.12: FOI Laboratories Test Reports

ICP Metals-Vanadium(V)	report in ppm	HL-1158	0
ICP Metals-Zinc(Zn)	report in ppm	HL-1158	1
Lubricity, HFRR @ 60°C	520 um maximum (micron)	ASTM D6079	700
Oxidation Stability	minimum 6 hours	ASTM D7545	25.8
Pour Point	report °C	ASTM D97	-49
Sulfur	report ppm	ASTM D5453-09	4
Viscosity @ 40°C	1.3 - 4.1 cst	ASTM D445	2.2
Water and Sediment	0.05 maximum (% volume)	ASTM D2709	0.001

Comments:

Gas aroma present.

Low Flash Point: A low flash point fuel can be a fire hazard, subject to flashing and possible continued ignition and explosion. A low flash point can also indicate contamination with low flash fuels such as gasoline and or Kerosene.

These results are submitted pursuant to our terms, conditions and limitations and laboratory pricing policy. No responsibility is assumed for the manner in which these results are used or interpreted.

8014 NE 13th Ave., Vancouver, WA 98665

(b) FOI Laboratories ASTM D975 Test Report, page 2

Figure 3.12: FOI Laboratories Test Reports



Certificate of Analysis
Laboratory Number: 102620225

Stephen Lucas
Colorado State: Chemical
Energy Conversion Lab
430 N. College Ave.
Fort Collins, CO 80524
USA
509-220-6228
Sample ID:
Purchase Order:
Work Order:
Package:

Sample Taken From:
Type of Fuel: Unknown
Sample Collection Date:
Date Received: October 26, 2022
Date Released: November 8, 2022
Component Make:
Component Model:
Serial Number:
Quantity in Tank:
Tank Capacity:

Test	Limit	Method	Result
Flash Point	report °C	ASTM D93-10	77

Comments:

These results are submitted pursuant to our terms, conditions and limitations and laboratory pricing policy. No responsibility is assumed for the manner in which these results are used or interpreted.

8014 NE 13th Ave., Vancouver, WA 98665

(c) FOI Laboratories Flash Point Retest

Figure 3.12: FOI Laboratories Test Reports



Figure 3.13: Deere 4045 4.5L Tier 3 diesel engine used in this testing

3.3.2 Diesel-Blend Engine Compatibility

To verify the compatibility of the selected blend, and other possible candidates such as P-n-P, engine testing was performed using a Deere 4.5L diesel engine. Various performance and emissions characteristics were compared using the default engine maps, which verified true drop-in performance. Optimization of engine mapping to these new fuels is an area where this work could be further extended.

For the engine testing, a highly instrumented 4.5L Deere 4045 Tier 3 off-road compression ignition engine was used. Monitored variables include high-speed in-cylinder pressure, intake and exhaust temperature and pressure, fuel consumption, 5-gas and FTIR exhaust composition, and exhaust PM capture (the stock particulate filter is removed for this testing). The exhaust composition analysis measures CO and CO₂, O₂, NO_x, and total hydrocarbon emission. Exhaust PM capture was performed on parallel filters, allowing gravimetric analysis of PM_{2.5} and organic carbon / elemental carbon fractions. During testing, the engine is operated at steady state on diesel to reach operating temperature, then the fuel is switched, conditions stabilized, and then operated for 15 minutes on the test fuel.

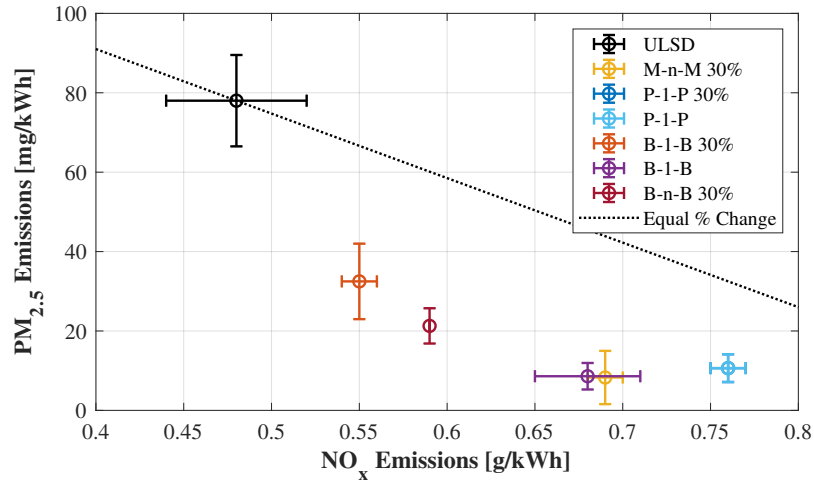


Figure 3.14: PM/NO_x tradeoff for OMEs vs ULSD

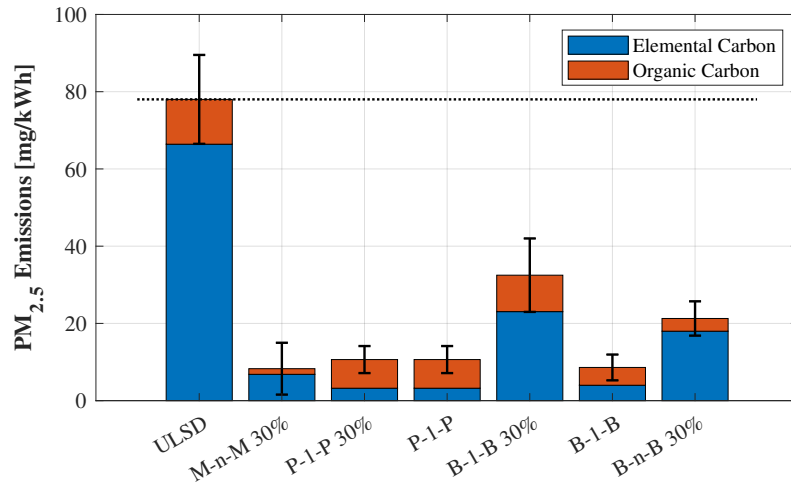


Figure 3.15: PM emissions from Deere 4.5L engine testing

Test fuels for this testing include standard ULSD diesel, P-1-P and B-1-B both neat and blended 30% in ULSD, and M-n-M and B-n-B blended 30% in ULSD, where the M-n-M composition in mol% is 48.1, 29.7, 16.6, and 5.6 for M-3-M through M-6-M, and the B-n-B composition in mol% is 7.7, 36.9, 29.7, 16.4, 5.1, and 4.1 for B-1-B through B-6-B respectively. The engine was operated at 1700 RPM and 325 N-m.

Combustion behaviors were qualitatively similar for the different fuels, with a fast initial burn followed by a second, larger heat release peak for the diffusion burn. CA10 and CA50 (the crank angle timing of 10% and 50% fuel energy burned) remained similar across the different

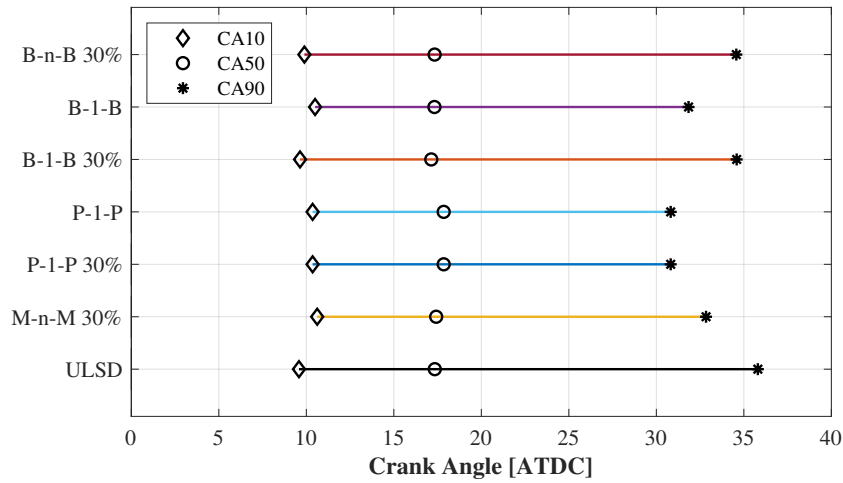
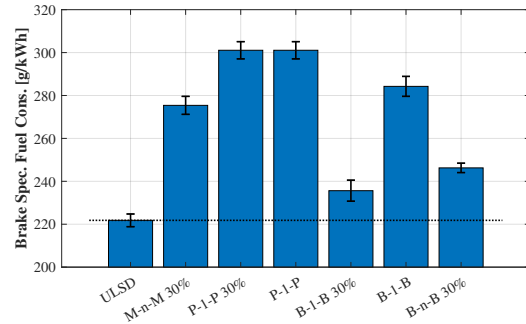
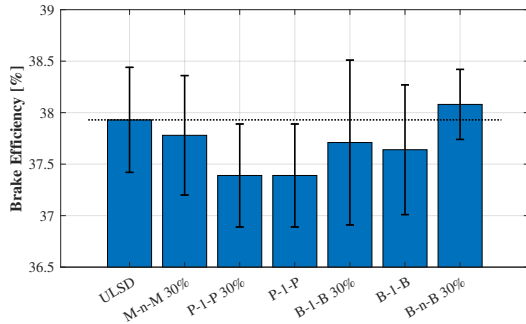
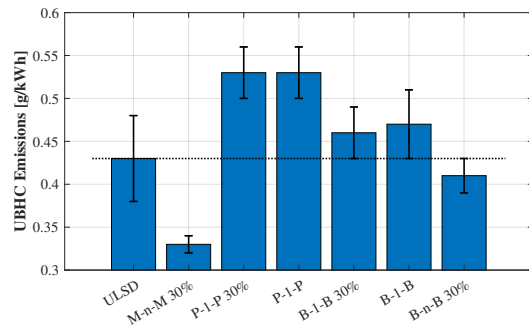
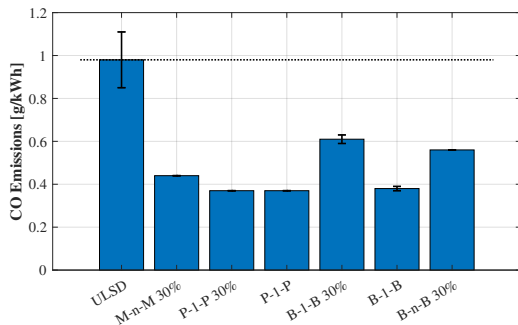


Figure 3.16: Combustion timing of Deere 4.5L with ULSD and OMEs



(a) Brake efficiency of Deere 4.5L with ULSD and OMEs **(b)** Brake-specific fuel consumption of Deere 4.5L with ULSD and OMEs

Figure 3.17: Engine performance of Deere 4.5L with ULSD and OMEs



(a) CO emissions of Deere 4.5L with ULSD and OMEs **(b)** Unburned hydrocarbon emissions of Deere 4.5L with ULSD and OMEs

Figure 3.18: Other emissions of Deere 4.5L with ULSD and OMEs

fuels, with the end of combustion (defined by CA90) delayed in tandem with the decreased LHV of the OMEs. Brake efficiency remained the same within experimental error, while brake-specific fuel consumption increased in tandem with decreasing LHV. In terms of emissions, a significant decrease in PM_{2.5} emissions is found with all OMEs and OME-blended fuels, while the organic carbon fraction of the PM increased for the neat OMEs. CO emissions for all OME and OME-blended fuels decreased compared to the baseline USLD, indicating improved combustion efficiency. Consistent with literature observation of increased CH₂O emissions from M-n-M, all OME blends displayed higher CH₂O emissions than ULSD. Total hydrocarbon emissions varied, with neat P-1-P and 30% M-n-M showing significant higher and lower emissions, respectively, while the other OME fuels had insignificant differences in hydrocarbon emissions.

Chapter 4

Combustion and Engine Behavior of Various OMEs

In this chapter, the combustion behaviors of some of the new OMEs is tested. The primary testing involves autoignition testing of some of the lighter OMEs (E-1-E, E-2-E, P-1-P, and iP-1-iP) in a rapid compression machine (RCM); additionally, iP-1-iP is tested via spark ignition in the RCM. Spark-ignited engine testing is performed on iP-1-iP in a Cooperative Fuels Research engine.

4.1 Methods

4.1.1 Rapid Compression Machine

The CSU Rapid Compression Machine was the focus of the majority of the combustion experiments. RCMs are a common device for testing of fundamental combustion behaviors; along with shock tubes, they are often used for measurement of prevaporized IDT to characterize fuels and provide data for kinetic model development. Sung and Curran [111], and recently Goldsborough et al. [112] provide excellent reviews of the uses of these machines. In summary, RCMs operate via rapid compression of a gas and fuel mixture to simulate the stroke of a reciprocating engine, or more generally to quickly create high-temperature conditions for combustion. Ideally, RCMs could be treated as true isentropic devices, however, heat losses to the walls prevent true isentropic behavior. As pressure can be more easily measured than temperature at high rates, the temperature is typically calculated as an integral over the actual pressure trace, incorporating changes in specific heat ratio γ [111]. This is referred to as the adiabatic core hypothesis and assumes that while heat losses occur at the wall, the core of the gas mixture at compression can be evaluated as the isentropic compression of the pressure-based compression ratio (as opposed to the geometric, volume-based compression ratio). Modern RCMs

typically use pistons with creviced faces to reduce vortices around the perimeter of the piston (“roll-up vortices”), which improves the accuracy of the adiabatic core hypothesis [41].

In addition to the heat loss to the walls, an additional facility effect which can have significant effect on IDT measurement accuracy is the presence of reactions during the compression stroke. Shock tubes have extremely rapid heating, with the gas being heated and compressed through the extremely thin shock wave which travels at greater than sonic speed, effectively eliminating this facility effect, however, RCMs are capable of lower compressed pressures and thus continue to be of interest despite this flaw [113]. As opposed to the near-instantaneous shock heating effect, the heating in the RCM happens on millisecond ranges; e.g. the CSU shock tube compression stroke is approximately 18 ms in duration. Particularly at higher temperatures or for more reactive fuels, a significant portion of the reaction can occur during the compression stroke so that IDT is not effectively measured from piston top-dead-center (TDC). Mittal et al. show this using dimethyl ether as a test fuel [114], wherein including the compression stroke in the model allowed more accurate prediction, indicating the presence of significant reaction during the stroke.

The CSU machine is a dual-piston, pneumatically-driven, hydraulically-locked device with multiple available chambers for different purposes. The geometric compression ratio of this device is approximately 11.4 in the chamber used for autoignition; the chamber for flame speed has larger dead volume from windows and has a geometric compression ratio of approximately 10.7. Creviced pistons are used to minimize roll-up vortex effects on the gas core. Pressures and temperatures are controlled via initial settings (fill pressure and sleeve temperature via heat tape) and variation of γ of the gas mixture by changing composition of the inert mixture between CO_2 , N_2 , and Ar. Monitored low-speed variables are initial pressure and initial sleeve temperature. High speed variables are piston positions (easily convertible to volume) and chamber pressure. Gas mixtures are created in a heated mixing tank. Liquid fuel is first added volumetrically to a tank at vacuum, and then gases are added via partial pressure to achieve the desired inert mixture and equivalence ratio (Φ). The gas mixing code accounts for

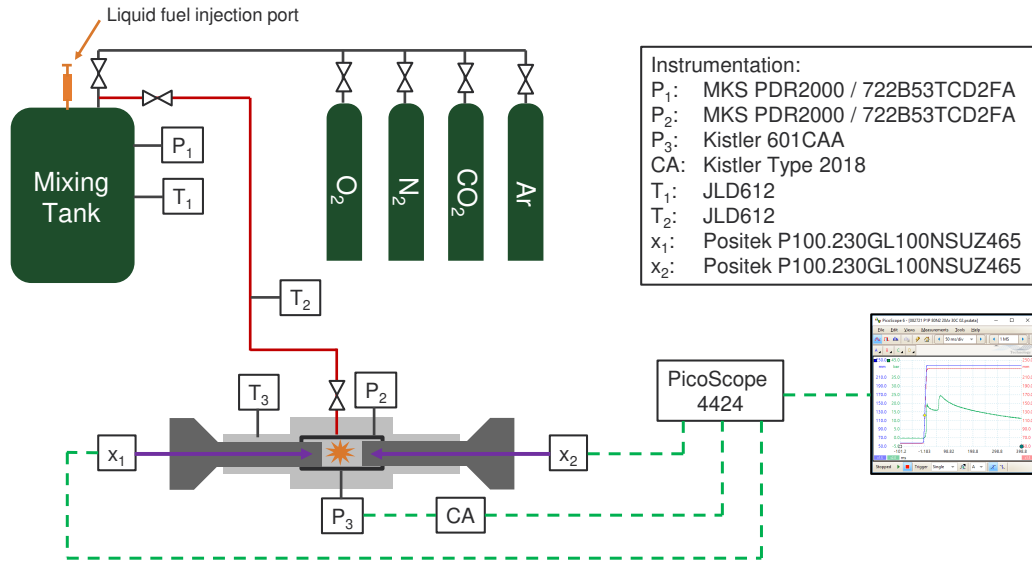


Figure 4.1: RCM system schematic

temperature changes during the filling process to reduce errors in mixture composition. A system schematic in Figure 4.1 details the instrumentation used.

For spark ignition testing, a laser spark was used. Use of a focused laser spark as an ignition source is reviewed by Phuoc et al. [115] and Morsy et al. [116], and has some advantages and disadvantages. A major advantage is the lack of physical objects in the core of the compressed gas, as would be the case for electrodes or a spark plug – this allows for improved visibility of the gas and flame expansion. However, initial flame kernels from laser sparks are not spherical; two counter-rotating regions on opposite sides of the laser path are the initiation regions for combustion. In some cases, a third lobe is also observed on the laser path; this is documented but the physics are less well understood [115]. In the tests here, this asymmetric flame initiation is observed, but in most cases rapidly transitions to mildly wrinkled spheroids and does not cause significant difficulty in measurement of flame speed, although as will be shown, lower temperature flames may retain the lobed asymmetry. In lean and rich combustion, laser ignition has been shown to have similar ignition energy requirements to electric sparks, but at near-stoichiometric conditions, it has been shown to require higher energy input for ignition [115]. The laser ignition system used on the CSU RCM consists of a Quantel Q-smart laser,

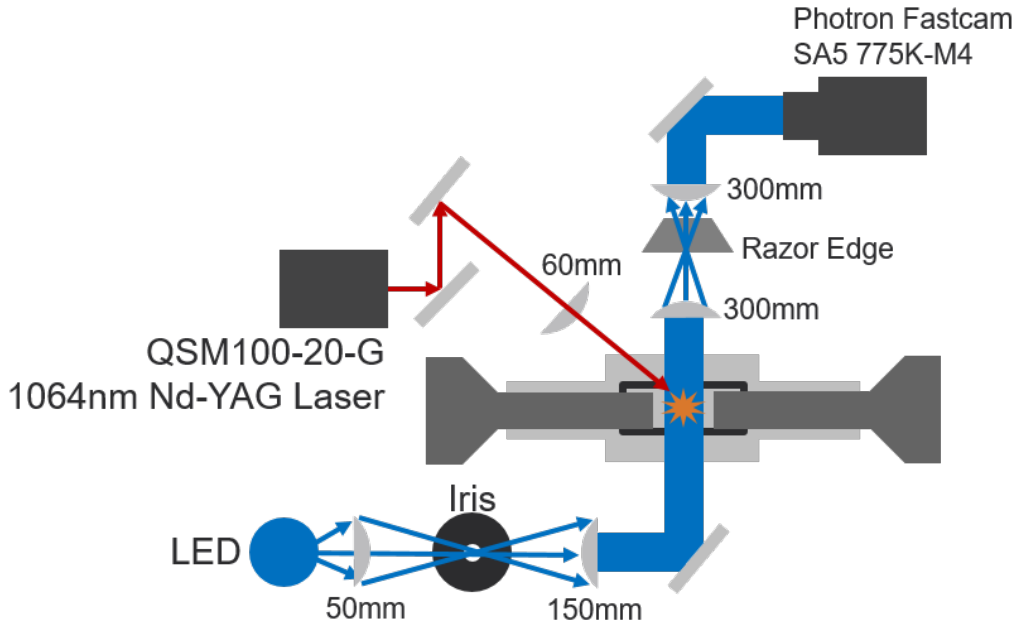


Figure 4.2: Schlieren optical schematic

model QSM100-20-G, focused down to a point in the center of the chamber with a 60mm focal length plano-convex lens. For flame measurements, an optical system is required. A chamber with large (26 mm visible diameter) windows was used, and an LED light source used for Schlieren imaging following the schematic in Figure 4.2. The camera used is a Photron Fastcam SA5, model 775K-M4, set at 42000 fps and 512x320 resolution (equivalent to 10.8 pixel/mm in this particular setup). Figure 4.3 shows a sample flamefront from this method, showing the initial asymmetric flame kernel and subsequent development to an approximately spherical flame.

4.1.2 Cooperative Fuels Research Engine

To directly quantify knock tendency, a CFR engine is used. The ASTM standards for Research Octane Number and Motor Octane Number (RON and MON) are followed [117, 118], with a modification to the knock index measure, as the standard analog detonation meter was replaced with a high-rate pressure transducer for measuring in-cylinder conditions. A fast Fourier transform (FFT) of the pressure curve is instead used for determining knock, where the FFT

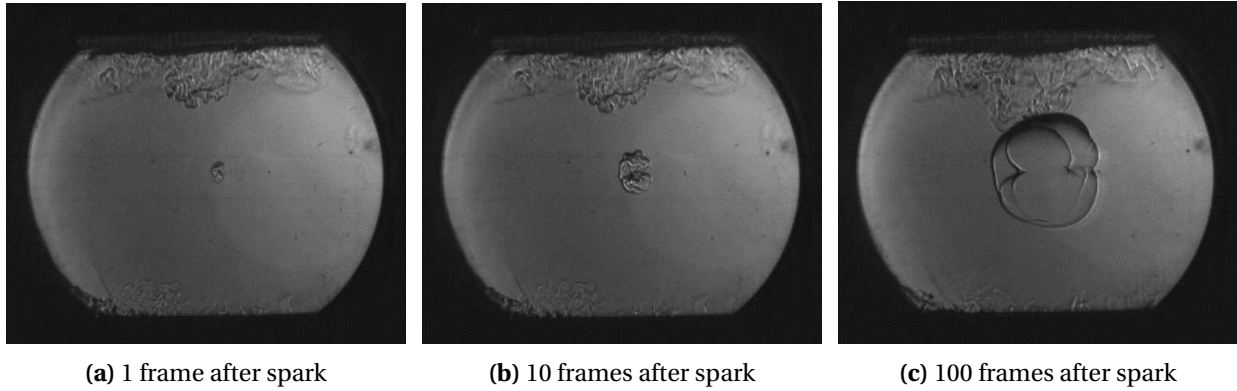


Figure 4.3: Representative Schlieren images of flamefront at 1, 10, and 100 frames (0.024, 0.24, and 2.4 ms) after the laser spark, from stoichiometric iP-1-iP in N₂.

value for a given reference fuel is used as the knock index in ON calculation. A KI real-time readout range of approximately 800-1800 was targeted, where the target fuel should knock at approximately 1200-1400, with the lower and upper brackets filling out the range.

The CFR engine is a single-cylinder engine with a variable compression ratio, which allows for control of the level of end-gas autoignition (EGAI, or knock) due to the change in compressed temperature from the variable compression ratio. The cylinder geometry is simple, with two valves (single inlet, single exhaust), flat piston face and head face, and two small ports on the upper cylinder head and wall for the pressure transducer (or in ASMTM standard configuration, detonation meter) and for the horizontally-mounted spark plug. The bore diameter is 82.6 mm, with a displacement of 0.611 L. Fuel flow is controlled via a single-jet carburetor selectable for three different sample fuels, with air-fuel ratio controlled via a column-height system and measured with a Motec oxygen sensor. Intake air is heated for the MON test via an inline heater downstream of the carburetor; for RON, the high altitude requires a low intake temperature of 11.5°C, which is achieved through the simple expedient of testing in the winter. A future improvement may be the addition of an inline chiller to allow D2699 tests to be run in summer. Spark timing is controlled via a Woodward controller, and is set to -13°ATDC (after top dead center) for RON testing, or a variable setting depending on CR for MON testing. Engine speed is controlled via a variable frequency drive AC motor which also absorbs the power generated during the test. High-speed pressure and piston position data are taken every 0.1° and



Figure 4.4: CSU CFR Engine

recorded via LabView. Low-speed (2 Hz) data are taken for intake air temperature (for RON) or mixture temperature (for MON), AFR, intake pressure, RPM, and coolant temperature.

4.1.3 Analysis Methods

RCM Autoignition Analysis

RCM high-speed and low-speed data are analyzed in MATLAB to identify TDC conditions and autoignition events. Some prior code from A. Zdanowicz was used as the skeleton for this analysis, but significantly modified and rewritten for this work.

Output data from the PicoScope is saved as a CSV file and imported into MATLAB. Piston positions are extracted and converted to volume. Pressure data is filtered at two separate levels with low-pass Butterworth filters. A higher passband filter is used to identify TDC location with minimal phase shift or loss of resolution, and a lower passband filter applied for the actual analysis to reduce noise. Time is offset to $TDC = t_0$. TDC conditions are calculated using the adiabatic core hypothesis, where the initial temperature is set, and then at each timestep ($\Delta = 5.0 \times 10^{-7}$) the new temperature is calculated from the ΔP across that timestep. γ is recalculated

at each timestep. The polynomials for gases – Ar, N₂, O₂, and CO₂ – are calculated from the polynomials in Lawrence Livermore’s n-Heptane v3.1 mechanism [119]. Polynomials for OMEs are either taken from literature (available for E-1-E from Li et al. [120]), or generated via group contribution methods from the MIT Reaction Mechanism Generator (RMG) [121]. The MIT RMG calculation of thermodynamic polynomial coefficients was compared to the polynomials in Li and found to be within 5% for 600 K - 1000 K, indicating acceptable accuracy of RMG for the undocumented fuels.

In the first set of RCM tests, highly dilute conditions were used (12:1 inert:O₂ ratio), which produced low dP/dt , and thus necessitated a slightly different definition of the start of autoignition. Typically, RCM IDT is defined either by the inflection point in the pressure rise from ignition, where IDT is assigned either as the time of the inflection, or the time of the root of the tangent to the pressure at this inflection point [122]. For high dP/dt , this method produces IDT which are essentially indistinguishable, however, for low dP/dt , the root of the tangent can occur well before the time when pressure rise begins, or the inflection point itself well after. Thus, we use a method where the tangent to the inflection point is intersected with the (horizontal by definition) tangent to the local minimum in pressure before pressure rise. This is similar to a method often applied to OH* measurements for IDT [123], however, here it is applied to pressure rather than OH*. For high dP/dt , there is little difference between this and the common methods, while for lower dP/dt , this method sits in between the two. As two-stage ignition was observed at low temperatures, this method had to be applied twice in these cases. A sample pressure trace showing this methodology is proved in Figure 4.5.

As the compression temperature at TDC is calculated from the pressure trace, assuming an isentropic core [111], the method of pressure trace filtration can affect the peak (TDC) temperature and pressure. The variance was found to be approximately +/-5 K and +/-0.1 bar within the range of half power frequencies that produce an accurate, low-noise pressure curve from a low-pass filter. The compression stroke produced the target pressures to an average of 20.1 bar with 1.55% (0.311 bar) standard deviation. Initial temperatures were measured via a thermocouple

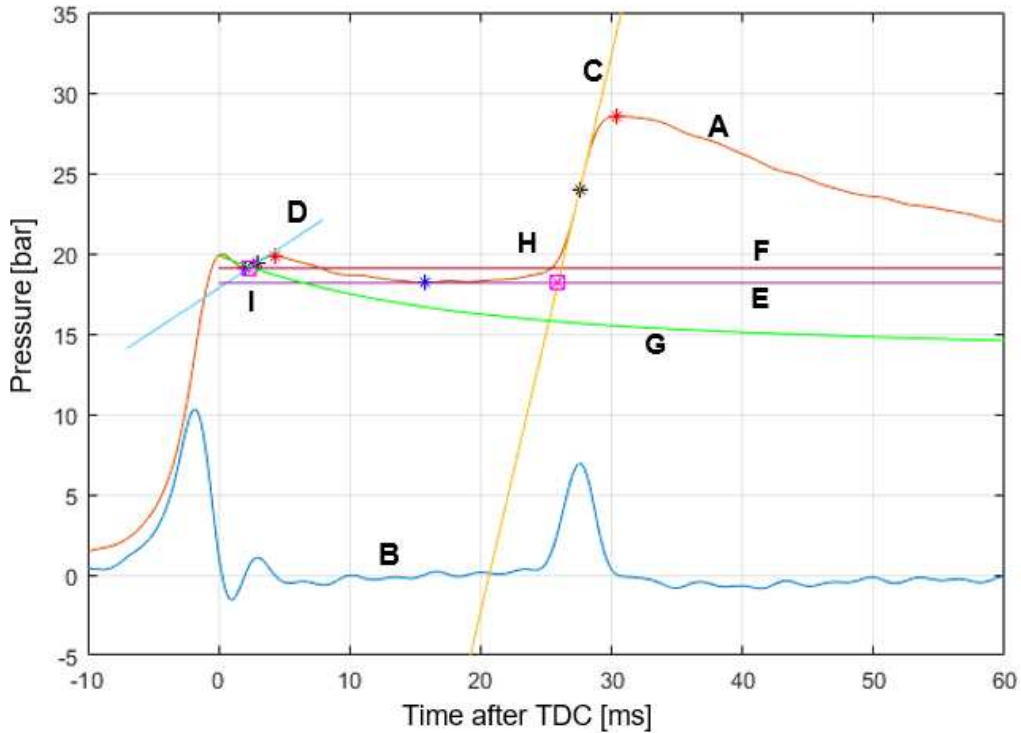


Figure 4.5: Example algorithm for solving IDT with a low dP/dt . *Line A:* Filtered pressure trace. *Line B:* Gradient of pressure. *Line C:* Tangent to pressure at maximum gradient (primary event). *Line D:* Tangent to pressure at maximum gradient (first stage event). *Line E:* Tangent to local minimum pressure (between first and primary event). *Line F:* Tangent to local minimum pressure (between TDC and first event). *Line G:* Nonreactive pressure curve, calculated from double-exponential function fitted to normalized and scaled average of three nonreactive pressure traces for the appropriate gas mixture. *Point H:* Intersection of Line C and Line E. Defines primary ignition delay. *Point I:* Intersection of Line D and Line F. Defines first stage ignition delay. For single-stage ignition, lines D and F and point I are not calculated, and Line E occurs between TDC and primary ignition.

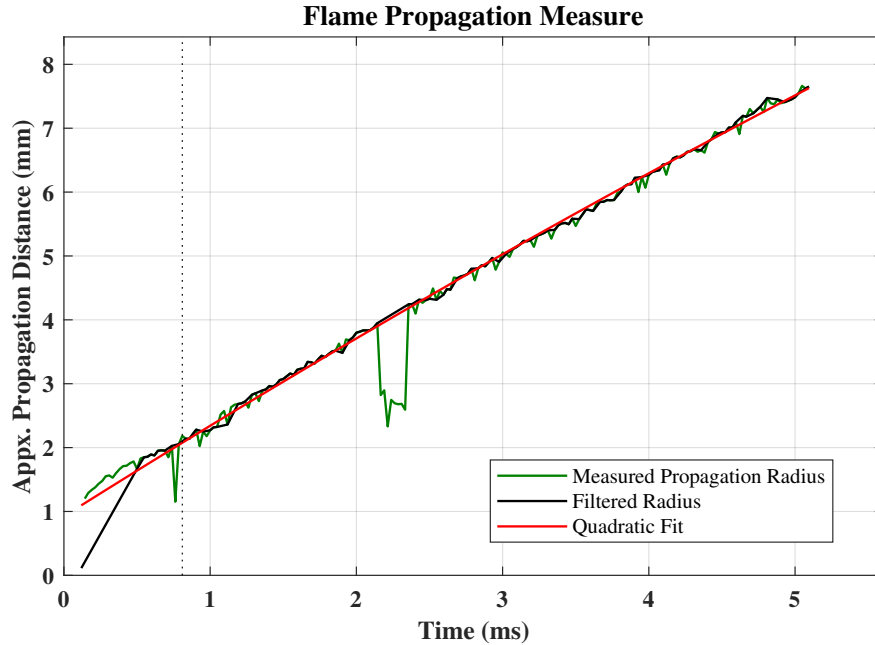
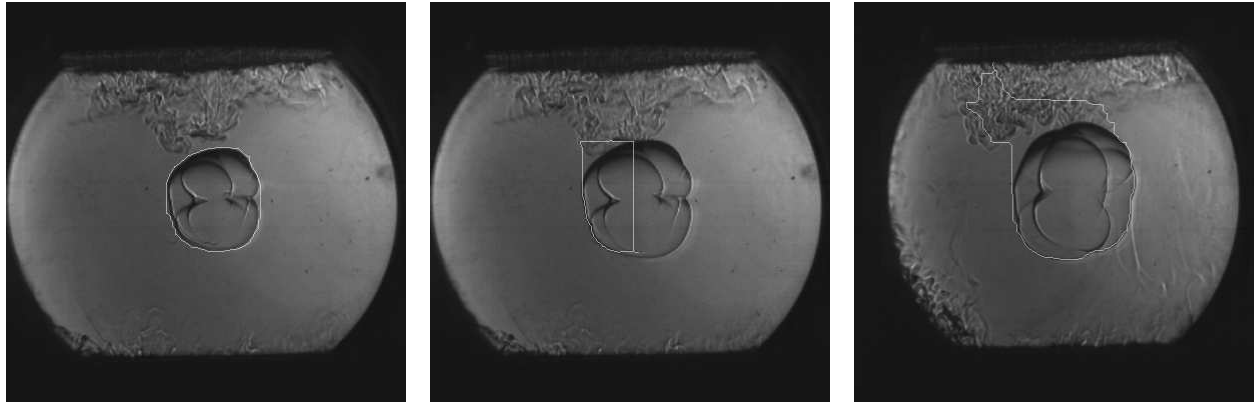


Figure 4.6: Measured flame propagation rates for a sample DIPM flame.

to an accuracy of ± 1 K, which transforms to ± 3.55 K for an average effective compression ratio of 10 (see Table S1 for these values) in a 40% N_2 / 60% Ar bath gas environment (the highest γ gas mixture used). Combining errors, the pressure is accurate to ± 0.327 bar, and the temperature to ± 6.13 K. Using sample E-1-E pressure traces at 720 K and 915 K (2 stage and single stage ignition), testing the range of reasonable filtering techniques provided a range of $\pm 7\%$ for first stage IDT and $\pm 5\%$ for primary IDT. Temperature errors of ± 6.13 K at 720 K and 915 K produce IDT errors of $\pm 6\%$ and $\pm 1\%$, respectively. Combining these errors, we expect an accuracy of $\pm 11\%$ for IDT measurements.

RCM Spark Ignition Analysis

Flame speeds are calculated from the spark-ignited flame images, using the methods of Zdanowicz et al. [124]. The flame radius change over time is measured and approximated to a spherical flame, and then a second-order polynomial fit is applied to the radius function. Figure 4.6 shows a sample output of this function, where the radius is measured, noise filtered out, and a quadratic fit applied from which the flame speed and stretch rates are calculated. Fig-



(a) Good flamefront identification of approximately spherical flame (b) Poor flamefront identification, missing a large part of the flame (c) Turbulence interference with flamefront identification

Figure 4.7: Representative Schlieren images of flamefronts where the calculator effectively and ineffectively identifies the flamefront, and where interference from piston face turbulence cannot be separated from the flame. From stoichiometric DIPM in N_2 .

Figure 4.7a-Figure 4.7c show varying degrees of accuracy in identification of the flamefront; most image sets for spherical flames are processed as Figure 4.7a, but many datasets had some individual images with inferior identification that is filtered out as shown in Figure 4.6. Highly aspheric flames were most likely to have poor identification of the flamefront or interference from piston face turbulence.

Flame stretch is calculated using both the linear approximation and the Kelley and Law non-linear approximation [125]. As unburned flame speed calculation is typically performed via a calculation of the density ratio of burned and unburned gases [124], a functional mechanism is required for this density ratio. No mechanism is available for DIPM, so the unburned gas density ratio is calculated via linear interpolation of LHV vs. density ratio between iC8 (as calculated via the Kelley reduced mechanism [126]) and M-1-M (from Li mechanism [120]). The density ratios of these two fuels, with very different energy release, is nonetheless quite similar at comparable temperature and stoichiometry.

Knock onset is calculated from the pressure trace of the spark-ignited events, using the apparent heat release rate method [124]:

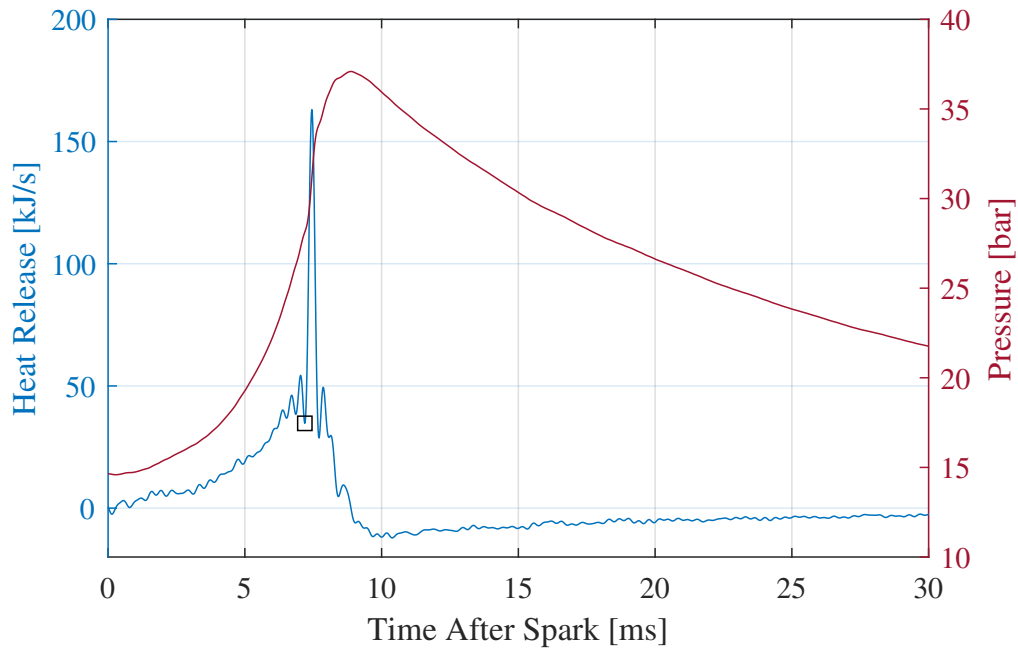


Figure 4.8: Knock indication in AHRR trace from a high temperature iP-1-iP sample SI test

$$AHRR = \frac{dQ}{dt} = \frac{1}{\gamma - 1} V \frac{dP}{dt} \quad (4.1)$$

An under-filtered pressure trace is used to calculate AHRR, without correction for heat loss to the wall. The maximum AHRR is compared to the previous local minimum, where for knocking combustion, a significant difference can be observed (Figure 4.8, Figure 4.9). This method was applied to randomly selected samples from each test condition and a comparison criterion selected which identified knock and onset time; knocking cases all had max AHRR >2x the prior local minimum for these test conditions. This criterion was verified against randomly selected individual cases of each test condition and effectively selected the cases and onset time where knock could be observed in the high-speed video.

CFR Engine Analysis

The standard method of evaluating fuel knock tendency is the CFR engine. In the typical application, the CFR engine will have a detonation meter installed, and knock is evaluated by the reading (from 0-100, typically) on this meter. The CSU CFR replaces this detonation meter

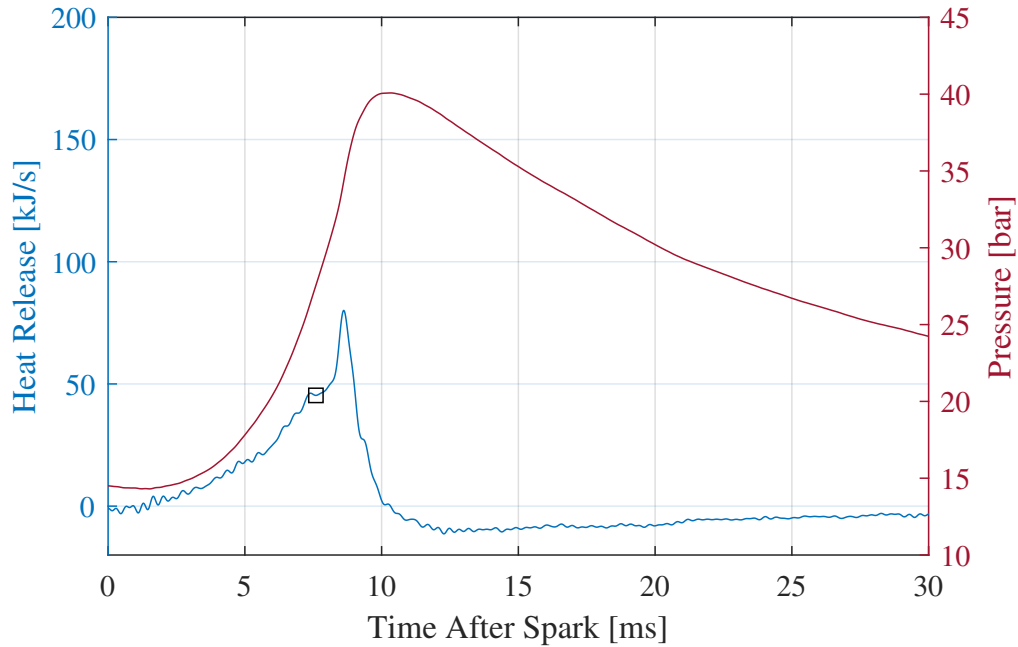


Figure 4.9: No knock indication in AHRR trace from a high temperature iC8 sample SI test

with a pressure transducer for evaluation of high-speed in-cylinder conditions. As a result, the methods provided in ASTM D2699 and D2700 [117, 118] are not directly applicable. In this work, we measure ON via a FFT of the cylinder pressure trace. Higher knock will appear as high-frequency, high-magnitude oscillation in the pressure trace, yielding a high FFT value. The knock index KI used in the ASTM standards is replaced with the arithmetic mean of the FFT of a given number of cycles, where the n highest FFT cycles are averaged. At this point, this can be called the modified KI and the standard bracketing method used: based upon the live readout of KI (in LabView, this is presented as the sum of the past 200 cycle FFT), primary reference fuels are assembled from iC8 and nC7 to provide KI which bracket above and below the KI of the target fuel. These PRFs have octane number (both RON and MON) defined by the volume percent of iC8, e.g. 93 vol% iC8 / 7 vol% nC7 is RON = MON = 93. This allows the calculation of ON via linear interpolation:

$$ON_{target} = \frac{ON_{lower}(KI_{upper} - KI_{target}) + ON_{upper}(KI_{target} - KI_{lower})}{KI_{upper} - KI_{lower}} \quad (4.2)$$

If the combustion stability (as defined by the CoV of IMEP) is comparable for the target fuel and upper and lower bracket PRFs, the calculated target ON is effectively independent of the number of cycles n used in the average of FFT to yield KI. If one of the fuels, most particularly the target, has poor combustion stability and subsequent higher CoV than the other fuels, the calculation of ON becomes highly dependent on n . In this work, n is varied from 100 to 5000, and the reported ON is determined via weighting by $1/n$ to apply the strongest weight to the highest knocking cycles, which are most determinate of the actual ON of the fuel.

4.2 Pre-Vaporized Ignition of E-1-E, E-2-E, P-1-P, and iP-1-iP

The majority of the content of this section has been published in the 39th Proceedings of the Combustion Institute as “Pre-vaporized ignition behavior of ethyl-and propyl-terminated oxymethylene ethers”, DOI: 10.1016/j.proci.2022.08.065. Reprinted with permission from Proceedings of the Combustion Institute. Copyright 2022 Elsevier.

4.2.1 Candidate Fuels & Chemical Preparation

Four OMEs were selected for this analysis, each representing a unique modification in the structure of the OME. The structures and calculated bond energies for these molecules are presented in Figure 4.10. Here we label each of the carbons for ease of discussion, starting with the end group carbon closest to the ether oxygen labeled as α , and so forth. For all OMEs presented, all carbons between the ether moieties are labeled δ for consistency.

The simplest OME tested in this study is E-1-E, the ignition and kinetics of which have been previously studied, providing a basis for comparison to our results [37, 46, 83, 130]. P-1-P is a fuel which, to my knowledge, has not been studied for its ignition or fuel characteristics in any previously published work; this fuel is used to consider the effects of lengthening the alkyl terminations. The fuel-relevant properties of E-2-E have been studied prior by Lautenschutz [30], but no kinetics or ignition delay experiments have been performed. Finally, iP-1-iP is a new, unstudied molecule, representing a change from a linear OME structure analogous to normal

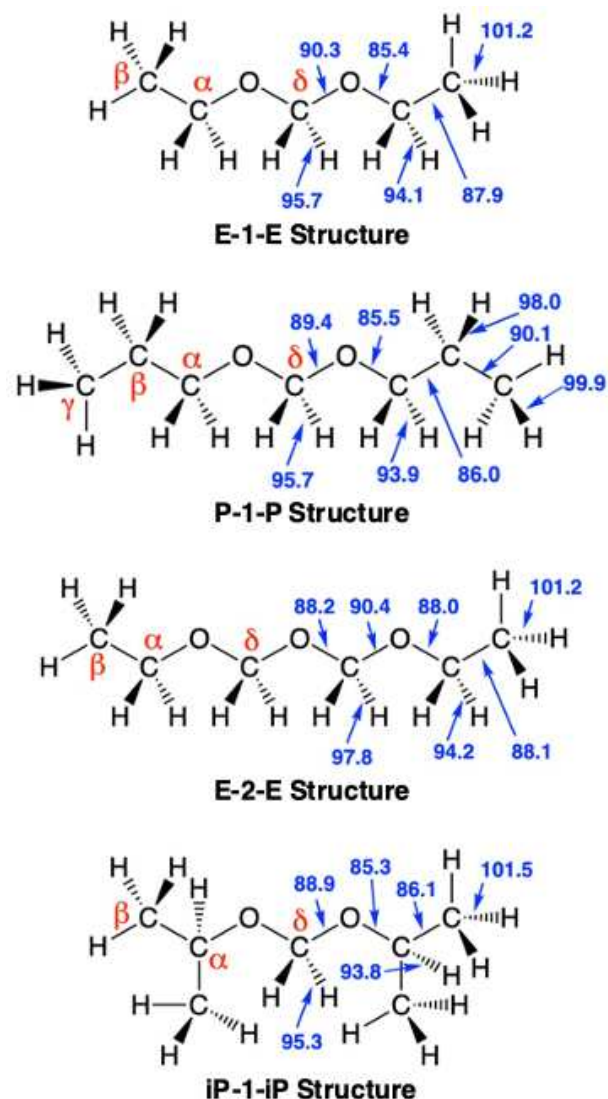


Figure 4.10: OME Structures: Red greek letter indicate carbon labels. Blue numbers indicate bond dissociation energies in kcal/mol from [127–129]

alkanes, to a branched OME structure analogous to iso-alkanes. Each of these molecules have similar bond dissociation energies (BDEs) for equivalent bonds as shown in units of kcal/mol in Figure 4.10. All BDE values were obtained using the ALFABET tool from the National Renewable Energy Laboratory (NREL) [127–129]. When available, density functional theory values were preferred over machine learning values.

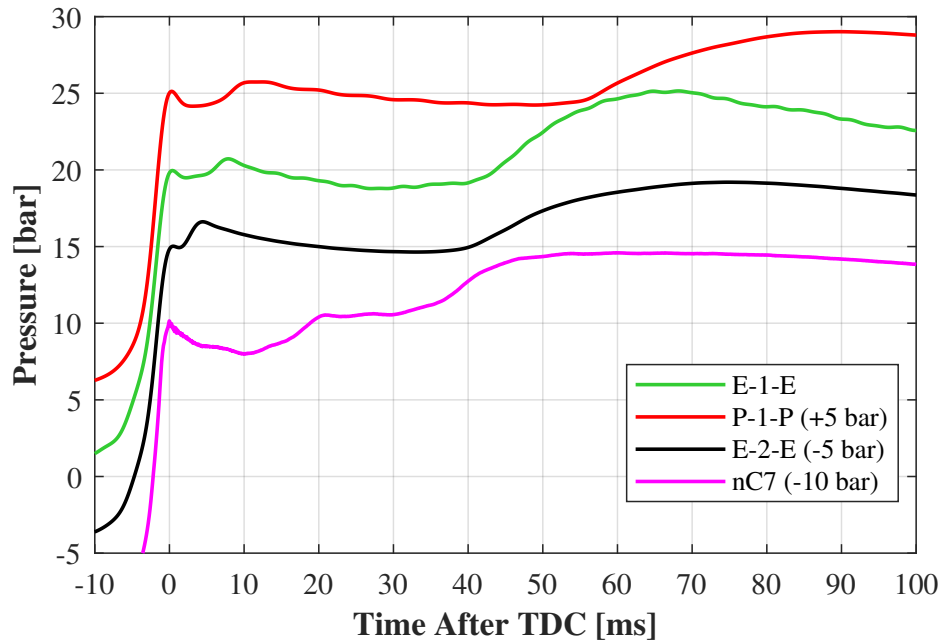


Figure 4.11: Pressure traces for representative tests at 700K and 20 bar compressed pressure, $\Phi= 1.0$, 12:1 inert:O₂. (note that pressure offsets have been applied to prevent overlap)

4.2.2 Results

The observed ignition behavior of the OMEs generally fell into three categories: at lower temperatures, the linear OMEs (E-1-E, E-2-E, and P-1-P) demonstrated multi-stage ignition with relatively low pressure gradients (see Figure 4.11). As the temperature increased, the first stage ignition disappeared, resulting in single stage ignition with a faster rate of pressure rise. Finally, the branched OME (iP-1-iP) only ever demonstrated single stage ignition; further, this fuel was incapable of ignition at the 20 bar compressed pressure used in earlier tests. At 30 bar, high temperatures were required to initiate ignition and the IDT fell rapidly with increasing temperature afterward.

The primary IDT for all of the tests at 20 bar where ignition occurred (tests at temperatures too low for ignition were performed, but are not shown here) is shown in Figure 4.12. First stage IDT, when observed, are shown in Figure 4.14. In Figure 4.13, the calculated IDT of n-heptane [119] using Chemkin simulation provides a reference to a more well-studied fuel; similarly, Figure 4.15 includes calculated iso-octane IDT [132]. Additionally, Figure 4.13 contains simula-

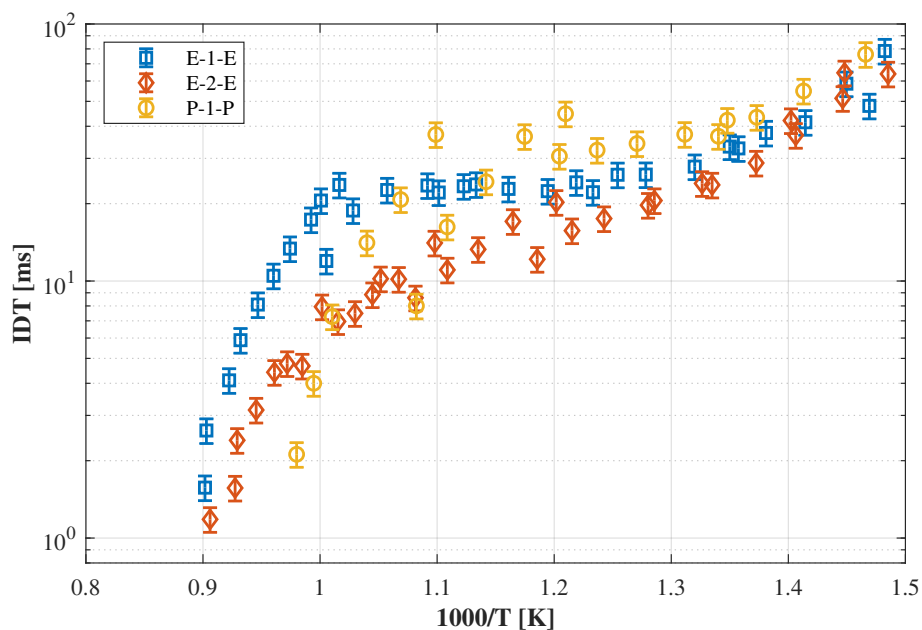


Figure 4.12: Calculated primary IDT of linear OMEs at 20 bar compressed pressure, $\Phi=1.0$, 12:1 inert:O₂

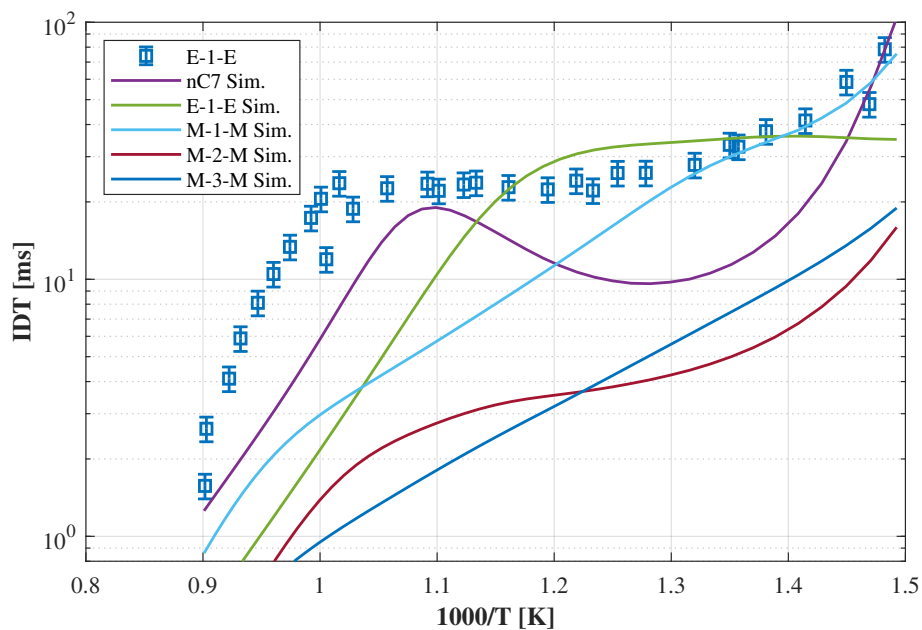


Figure 4.13: Calculated primary IDT of E-1-E with various mechanisms of nC7 and OMEs at 20 bar compressed pressure, $\Phi=1.0$, 12:1 inert:O₂ [44, 46, 47, 119, 131]

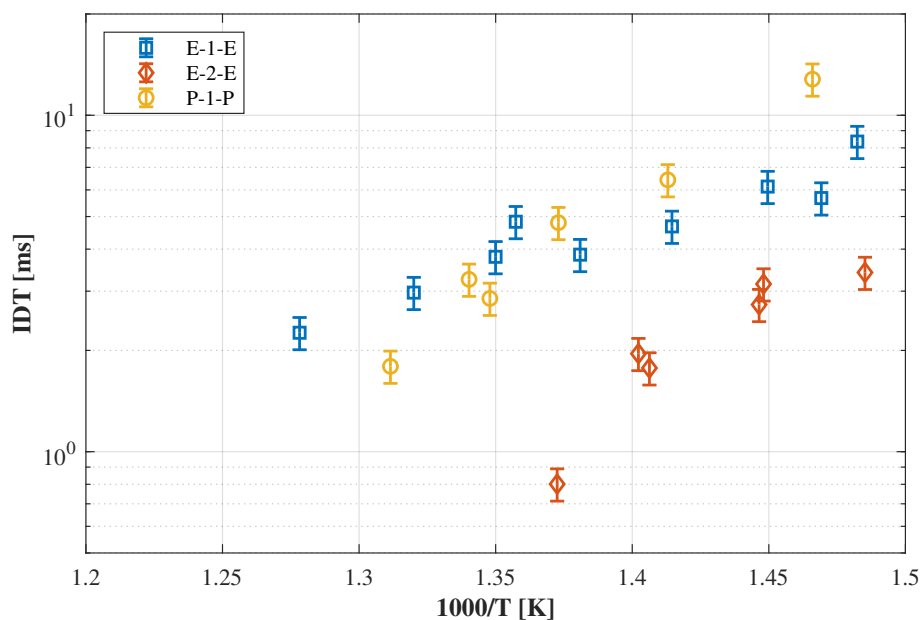


Figure 4.14: Calculated first stage IDT of linear OMEs at 20 bar compressed pressure, $\Phi = 1.0$, 12:1 inert:O₂

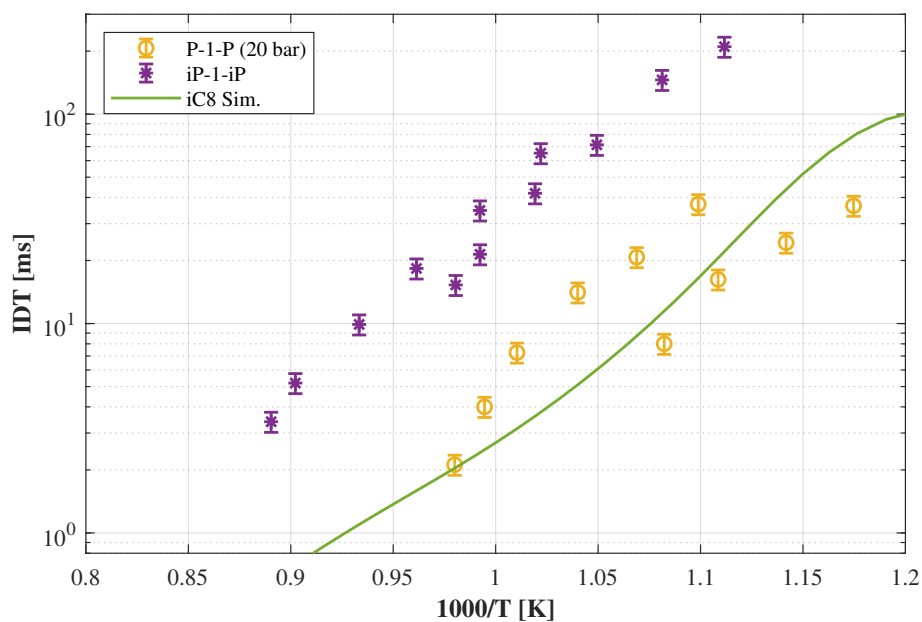


Figure 4.15: Calculated IDT of iP-1-iP at 30 bar compressed pressure, $\Phi = 1.0$, 12:1 inert:O₂ compared with P-1-P at 20 bar and simulation of iC8 via LLNL v3.0 mechanism [132]

tions of M-1-M [120], M-2-M [43], M-3-M [131], and E-1-E [47] from literature to show where the measured values compare to kinetic mechanisms for other, primarily methyl-terminated, OMEs. We consider the chemical basis of observed behavior later in this section; however, on a broad scale there are some basic observations. First, we observe that all of the tested linear OMEs show strong nonlinear temperature dependencies, but not true negative temperature coefficient behavior as seen with n-heptane. Secondly, iP-1-iP behaves similar to iso-octane without apparent nonlinearity, but has delayed ignition.

Prior literature, e.g. [133], notes that discontinuities in IDT curves may occur with changes in diluent gas composition, particularly with increasing argon concentration, where ignition slows for a given temperature condition due to thermal effects. We note some of this behavior in our data, most apparently for the P-1-P at just above $1000/T = 1.1$; for E-1-E and E-2-E these effects are observable but less apparent as they occur in a region where the IDT is nearly unaffected by the temperature and thus thermal effects will produce less noticeable changes in IDT. Prior literature studying fuels with established chemical mechanisms, e.g. [114, 134], have noted that at higher temperatures and shorter IDTs, the effects on IDT of radical formation during the compression stroke may not be negligible. Consequently, we caution the reader that the reported high-temperature IDT may be shorter than would occur if TDC conditions were achieved instantaneously without facility effects, and simulations of these conditions should include the compression stroke.

As a primary point of comparison, we will first consider the behavior of E-1-E, as its ignition has been characterized; we direct the reader to [46, 47, 83] for detailed discussion of the kinetics of this fuel. Here, E-1-E shows a wide region (750 - 1000 K) where IDT is essentially independent of temperature. Lehrheuer et al. [37] observed similar behavior in prior RCM testing of this fuel at these dilute conditions (we note that their observed IDT is faster as their tests were performed at 30 bar compressed pressure); similarly, kinetic modeling by Li et al. [46] shows a small temperature-independent region, although their modeling is primarily performed with standard air (3.76:1 inert to oxygen ratio).

Effect of Extending the Oxymethylene Chain

Using E-1-E as a reference, it can be observed that adding an additional oxymethylene unit (E-1-E \rightarrow E-2-E) advances the ignition at moderate to high temperatures (although it is worth noting that at low temperatures, <750 K, E-1-E and E-2-E have comparable IDT), and advances the temperature where IDT begins to rapidly decrease. This behavior is similar to that observed by Cai et al. [131] when transitioning between methyl-terminated OMEs of various oxymethylene chain lengths, although one can note from the above work that this reduction appears to have a diminishing effect as the chain length continues to increase, with the largest change occurring with an increase from one to two oxymethylene units. Additionally, as shown in Fig. 4.11, at low temperatures, the first stage ignition of E-2-E is faster by a few milliseconds - not a large change in comparison to the primary IDT, but roughly twice as fast as E-1-E for the first stage only. A test of n-heptane at comparable conditions shows that the n=1 OMEs have similar first stage ignition timing to n-heptane, while the all of the OMEs have slower primary ignition at these low-temperature conditions.

In their analysis of diethoxymethane decomposition, Jacobs et al. [47] found that as temperature was increased, the diethoxymethane radical formed after H-abstraction from the central methylene group (analogous to the δ -E-1-E radical) and rapidly β -scissioned to form ethyl formate rather than react bimolecularly with O₂ to form a peroxy radical, essentially inhibiting hydroxyl formation and retarding ignition. Notably, the reaction rates for the decomposition of δ -E-1-E used in their model were the highest pressure rates from Kroger et al. [83] and may be too fast by as much as a factor of 20 for the 10 bar IDT experimental conditions, potentially exaggerating the observation. Li et al. [46] similarly noted the importance of the δ -E-1-E radical on inhibiting ignition at higher temperatures, though they attributed the effect to the lesser number of unique peroxy radicals that can be formed as compared to the other diethoxymethane radicals. Similar arguments may be made to explain the faster reactivity of E-2-E. Fig. 4.10 shows that the C-O bond attached to α -carbon is slightly stronger for E-2-E (2.6 kcal/mol), which would slow β -scission of the δ -E-2-E radical and provide more opportunity for ROO for-

mation. Furthermore, the symmetry of E-1-E is broken with the addition of another methylene group. The extended chain would allow for 5 unique QOOH products to be made from the δ -E-2-E ROO, which would increase possible reaction paths leading to OH-radical production.

At low temperatures, Li et al. [46] and Jacobs et al. [47] both conclude that reactions of the α -E-1-E ROO and β -E-1-E ROO radicals are the primary drivers of ignition. Cai et al. [131] confirmed that this remains true for n=2 methyl-terminated OMEs. Thus, the additional central H-atom sites would not be expected to affect the low-temperature IDT, as observed in Fig. 4.12. However, the first stage IDT for low temperature reactions does decrease with the oxymethylene addition (see Fig. 4.14). Merchant et al. [135] note the first stage IDT can be directly attributed to generation of ketohydroperoxides (KHPs) in the low temperature ignition regime. In order for KHPs to form, ROO must isomerize to QOOH, undergo a second O₂ addition to form OOQOOH, and finally undergo an internal H-atom abstraction before decomposing to form a KHP. Comparing the BDEs for E-1-E and E-2-E in Fig. 4.10 highlights why E-2-E has a faster first stage IDT. With the addition of another oxymethylene unit, the influence of the O-atoms on neighboring bonds is enhanced, slightly increasing the C-O bond strengths. This creates a stabilizing effect, slowing down β -scission to increase likelihood of O₂ addition to the E-2-E radicals. Paired with the previously discussed increased number of possible QOOH configurations for E-2-E, which in turn, increases the number of possible second O₂ addition sites, E-2-E is more likely to form KHPs, enhancing first stage IDT.

Effect of Lengthening the Terminating Alkyl Groups

Again referencing E-1-E as a base, the shift to P-1-P demonstrates the effect of extending the alkyl termination groups by one additional methylene per side. In this case, the larger molecule shows similar trends to E-1-E, but at lower temperatures (up to approximately 900 K) is less reactive, and transitions towards rapid ignition at lower temperatures (around 1000 K compared to 1100 K for the E-1-E), leading to a smaller region of temperature independence than E-1-E. The rapid ignition at high temperatures speeds up to the point that above 1000 K, P-1-P reacts an order of magnitude faster than E-1-E, and slightly faster than E-2-E. Despite observable dif-

ferences in the primary IDTs for E-1-E and P-1-P, the first stage ignition of both fuels have quite similar behavior.

To understand the variations in ignition behavior with the increase of the end group alkyl chain length, we consider the differences in H-abstraction kinetics between methyl ethyl ether (MEE) and methyl propyl ether (MPE). MEE and MPE are similar to E-1-E and P-1-P respectively, terminating the molecule at the first oxymethylene group. In a theoretical kinetics study of HO₂ + various ethers, Mendes et al. [136] calculated the reaction rates for abstraction at each unique H-atom site in MEE and MPE. At low temperatures (up to 500 K), 99% of all H-abstraction from the C₂ and C₃ end groups occurs on the α -carbon, and the total rates for H-abstractions at all sites on the C₂ and C₃ end groups are similar (within a factor of 1.5 with DEE abstraction occurring slightly faster). It is reasonable to expect that abstraction at the α -carbon on E-1-E and P-1-P would dominate at low temperatures, and the resultant fuel radicals would combine with O₂ to form α -ROO radicals. It is facile for the α -ROO radicals to form 6-membered ring transition states to internally abstract an H-atom. For E-1-E, a 6-centered transition state is formed to abstract the weakened δ -hydrogen, and would be expected to be the only competitive route. P-1-P has two 6-centered transition state options: internal abstraction of the δ -hydrogen similar to E-1-E, or to abstract the stronger (4.2 kcal/mol stronger) γ -hydrogen, which is unlikely to occur. Given the similar chemistry for low-temperature oxidation of E-1-E and P-1-P, it is unsurprising that first stage ignition behavior and low-temperature primary IDTs are similar.

As temperature increases, so do the deviations between the IDTs of E-1-E and P-1-P. E-1-E H-abstraction reactions increase in total rate, but continue to occur >97% at the α -hydrogen site. Thus, the E-1-E oxidation mechanism is unchanged with temperature, though temperature can affect subsequent branching of the ROO/QOOH/OOQOOH radical cascade to HO₂ and OH. For P-1-P, the chemistry begins to change around 1000 K, at which point only 87% of abstraction occurs at the α -hydrogen site, with the balance occurring at the β -hydrogen site. This opens a second possible OOQOOH pathway, in which the expected second O₂ addition site is still expected to be the δ -carbon. With the relocation of one peroxy group one atom further from

the oxymethylene backbone, the subsequent β -C-O bond would be expected to be weakened, promoting faster decomposition to reactive radicals. This may account for the rapid increase in P-1-P reactivity but warrants further study to confirm the role of β -hydrogen abstraction on IDTs.

Effect of Branching Terminating Alkyl Groups

The final molecule to consider is the branched OME, iP-1-iP. For this, we will compare to linear P-1-P, which shares the same chemical composition but with a different structure. In this case, iP-1-iP did not react at all in the measured time frame (400 ms after TDC) under the original test conditions of 20 bar compressed pressure, even at temperatures exceeding 1000 K. Therefore, to get reliable ignition, the pressure was increased to 30 bar, and even at these elevated pressure conditions, measurable ignition still did not occur until 900 K. However, upon reaching a point where ignition occurs, the IDT advanced rapidly, decreasing two orders of magnitude from more than 200 ms to slightly more than 3 ms in a very small temperature range, as seen in Fig. 4.15. No multi-stage ignition behavior occurred with this molecule at any test condition, although the ignition required temperatures outside of the multi-stage region for P-1-P.

To explain this behavior, we compare the ignition of P-1-P and iP-1-iP to previously published work by Johnson et al. [137], who studied the ignition of n-propanol and isopropanol in a shock tube at 1 atm and found that isopropanol has a longer IDT than n-propanol. However, the somewhat increased IDT for isopropanol is not enough to explain the disparate IDT behavior of P-1-P and iP-1-iP. A theoretical study on H-abstractions of n-propanol and isopropanol by OH may further clarify this behavior. Guo et al. [138] showed that for n-propanol, abstraction at the α -carbon is preferred at all temperatures above room temperature. The equivalent H-atoms in P-1-P would be either the α -hydrogens or potentially the δ -hydrogens. Both resultant radicals can readily accept addition of O₂, promoting low-temperature ignition kinetics. In contrast, Guo et al. [138] showed that for isopropanol, abstraction at the the α -carbon is only preferred below \sim 1000 K (above \sim 1000 K methyl group abstraction is preferred). This has significant consequences for iP-1-iP ignition. Even more so than isopropanol, the α -hydrogens in

iP-1-iP are crowded. O₂ would be unlikely to add at the α -site; β -scission to less reactive products such as acetone, formaldehyde, and propene is preferred. The result would be an arresting of the ROO cascade necessary for ignition at low temperatures.

As temperature increases, the abstraction at the β -carbon sites becomes more important. At 900 K, Guo et al. [138] observed ~40% of all abstraction from isopropanol occurs at the terminal methyl sites. Similarly for iP-1-iP, abstraction at the terminal methyl sites is expected to become significant at ~900 K, creating β -iP-1-iP radicals which are unencumbered enough to accept the addition of O₂. These ROO radicals can then begin the ROO cascade required for ignition, and hence, this phenomenon explains the lack of observed ignition until ~900 K in this work.

4.3 iP-1-iP as a Spark Ignition Fuel

Following the dilute autoignition experiments showing the low reactivity of iP-1-iP, it was decided to pursue more investigation of iP-1-iP as a SI fuel, with more study on engine-relevant RCM IDT and spark-ignited tests. The similarity in physical properties to iC8, as well as the low ICN of 11, are all indicative of a possible application of iP-1-iP in gasoline engines, either neat or as a soot reduction additive. Additional iP-1-iP was synthesized in quantity to allow this testing. In the first case, autoignition IDT tests were performed again, focusing on iP-1-iP and iC8, with a temperature sweep at 5:1 inert:O₂ ratio. While not standard air, this approximates a 25% EGR blend, the highest typically used in SI engines [139, 140] but still engine relevant. This allowed sufficiently slow IDT to get good resolution in results, as the accuracy of RCM ignition suffers with short IDT due to facility effects [111, 114]. Following this, the laser ignition system was used to simultaneously measure flame speeds and evaluate knock fraction. Finally, iP-1-iP was evaluated in a CFR engine to compare its real engine performance to reference fuels and determine octane numbers and suitability for use in modern SI engines.

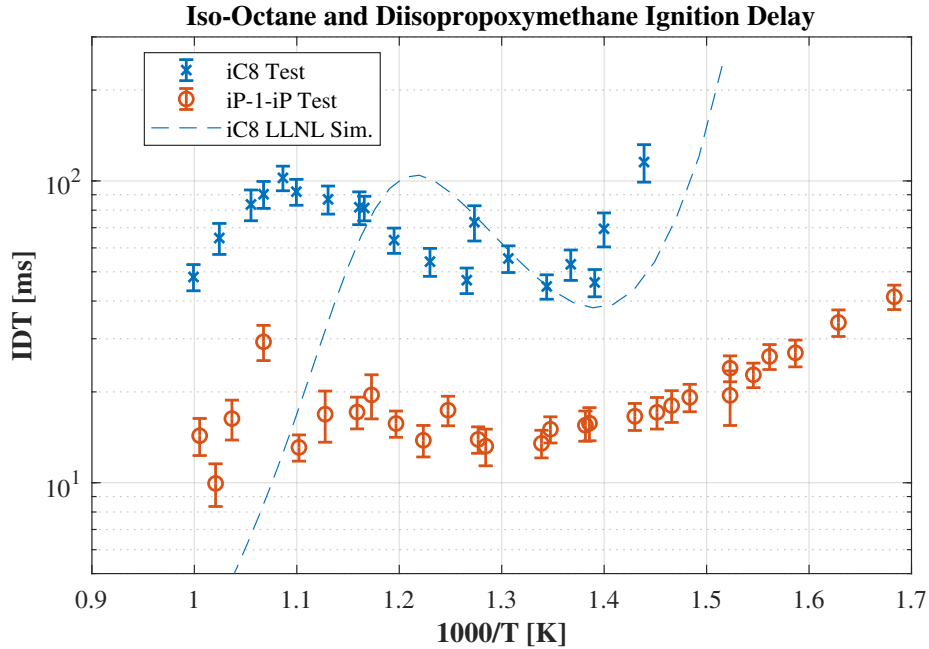


Figure 4.16: IDT of iC8 and iP-1-iP at 20 bar compressed pressure, $\Phi=1.0$, 5:1 inert:O₂.

4.3.1 RCM Autoignition

Autoignition tests were performed across a temperature range from $1000/T = 1.7 - 1.0$, which includes the region where negative temperature coefficient (NTC) behavior is expected from iC8. The gas composition was 5:1 inert:oxygen ratio (this approximates a 25% EGR ratio, on the higher end of SI EGR investigated in literature [140]), with stoichiometric fuel. Inert compositions were varied through blends of CO₂, N₂, and Ar to produce various TDC temperatures. The results of this testing are shown in Figure 4.16. In this testing, iP-1-iP ignited reliably through the entire temperature range; iC8 did not ignite below $1000/T = 1.45$. First stage ignition behavior was observed for both fuels, but had low dP/dt and could not be reliably calculated with the data filtration methods used. However, from observation of pressure traces, it was noted that at any given temperature, iP-1-iP had faster first stage IDT in addition to overall IDT.

Other oxymethylene ethers have been shown to have a region where temperature dependence of IDT decreases or becomes essentially temperature-independent [37, 131, 141], but none of the OMEs tested in literature demonstrated experimentally validated strong NTC behavior (the mechanism of Li et al. shows NTC behavior with extremely lean cases [46], how-

ever, this part of the kinetic model was not validated experimentally). Here, iP-1-iP is shown to have slight NTC in a similar temperature region ($1000/T = 1.3 - 1.1$) to iC8; this is the first time NTC has been documented for an OME, which indicates that the kinetics of iP-1-iP oxidation in the moderate temperature regime depart from those of the more commonly studied (primarily methyl-terminated) OMEs. In Section 4.2.2, it is proposed by analogy to iPrOH that the high-temperature kinetics of iP-1-iP may be dominated by competition between H-abstraction from the central vs. end carbons of the isopropyl group, however, iPrOH ignition studies have typically been performed at temperatures higher, and timescales longer, than those used here, thus this analogy has limited applicability [137, 142, 143]. Dedicated modeling efforts may be needed to explain this departure from typical OME behaviors.

The data shown in this chart offer some contrast to the earlier measurements of iP-1-iP, where it was observed that at high temperatures and high dilution (12:1), iP-1-iP ignited slower than a simulation of iC8 (Section 4.2.2). In this further study, we observe the opposite; iP-1-iP ignites 5-10x faster than iC8 for comparable conditions. Additionally, measurements of ICN place iC8 and iP-1-iP at nearly identical reactivity using the AFIDA device (ASTM D8183 [70]). This discrepancy deserves additional discussion. In the case of the prior RCM work (see Figure 4.15), it should be noted that the apparent slope of the iP-1-iP high-temperature curve is slightly higher than that of iC8 and crossover is possible at higher temperatures; further, while iC8 changes with pressure and inert dilution are well understood, iP-1-iP has only been studied at high-T/high-dilution and these moderate-T/moderate-dilution conditions, with no further work to fill in the possible gaps between these; it is certainly plausible that iP-1-iP IDT advances with lower dilution more rapidly than iC8. Further work would be required to verify this. Additionally, the earlier work tested iP-1-iP against an iC8 simulation; no physical tests were performed. A simulation of the iC8 tests performed here (Figure 4.16) indicates that the magnitude of the ignition times are in line with each other, however, the temperatures are different, with a “stretch” visible in the data. The simulated ignitions reach the peak of the NTC region and resume the decrease at a lower temperature than calculated in these tests; if similar discrepancies

exist for the earlier iP-1-iP testing, this would bias the iC8 simulation to appear more reactive than iP-1-iP at the high temperature conditions.

The discrepancy between ICN measurements (very similar) and the high degree of difference in reactivity seen here is somewhat easier to address. Firstly, it should be noted that at very low CN, the correlations curves for the AFIDA are very flat; small changes in ICN require large changes in IDT [71]; additionally, the method is only calibrated for $ICN > 35$. Per ASTM D8183 [70], the injection is set as a fixed-duration injection from a pressure-controlled fuel rail. Taking the densities of the two fuels into account (see Section 3.2.5), and treating the injector as a basic orifice where mass flow scales with the square root of density, it is reasonable to assume that 9% more fuel (by mass) will be injected into the chamber with iP-1-iP than iC8. Per Luecke et al., the AFIDA injects 0.117 iC8 g per injection [144]; with this assumption, a single iP-1-iP injection should use 0.128 g fuel. Considering the chamber conditions of the AFIDA [70, 71] and the stoichiometry of the two fuels, it can be determined that iC8 operates with a global equivalence ratio $\Phi = 0.62$, while iP-1-iP is leaner at $\Phi = 0.47$. This leaning effect would be expected to delay ignition for iP-1-iP, explaining in part the discrepancy between similar ICNs and quite different stoichiometric RCM ignitions, while the flat correlation curve serves to solidify the differences.

As iP-1-iP is investigated here as a candidate for gasoline addition, it may be necessary to match reactivity to iC8 behavior using a blend of iP-1-iP with a very low reactivity fuel; iPrOH is a clear candidate as it is already required for iP-1-iP production, and has high octane numbers (RON = 112, MON = 97, R+M/2 = 105 [145]). Neat iPrOH and 25%, 50% and 75 mol% blends in iP-1-iP were tested for the N_2 bath gas (approximately 750 K, in the NTC region for iC8 and iP-1-iP). Neat and 75 mol% iPrOH did not ignite at these conditions within the measurable range of this RCM (approximately 400 ms after TDC duration), while the higher iP-1-iP concentration blends bracketed the performance of iC8 in these conditions. First stage ignition of iP-1-iP was suppressed with iPrOH addition, where the presence of 25 mol% iPrOH delayed first stage ignition to similar timing to iC8 and reduced the dP/dt , while for 50 mol% iPrOH, no first stage

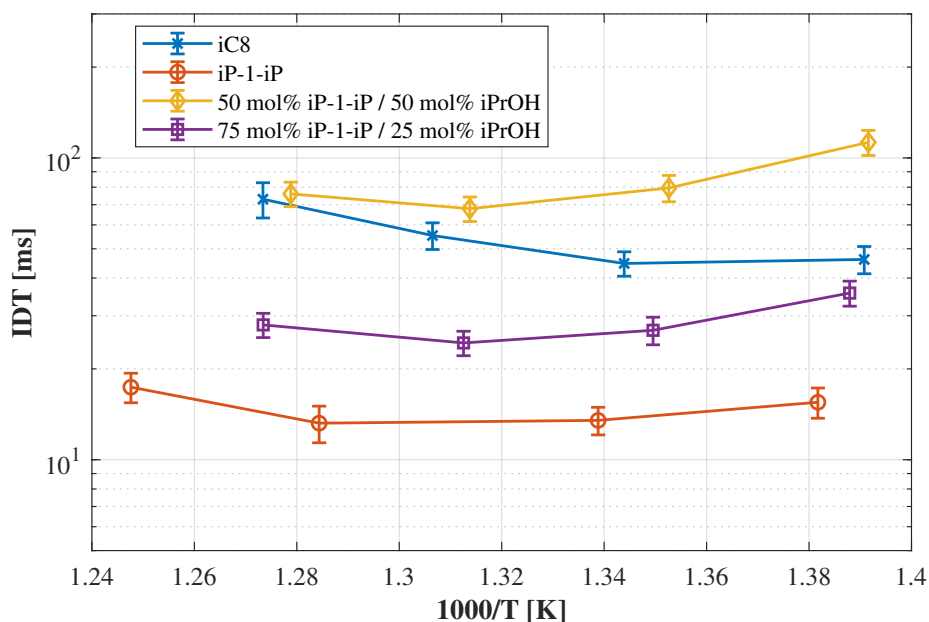


Figure 4.17: IDT of isooctane, iP-1-iP, and 50 mol% and 75 mol% iP-1-iP/iPrOH blends in 5:1 nitrogen / oxygen gas mix.

ignition is observed. Sample pressure traces at approximately $1000/T = 1.34$ are provided in Figure 4.18 showing the change in ignition as the reactivity is decreased via iPrOH blending.

4.3.2 RCM Spark Ignition

To consider the effects of a iP-1-iP flame in a spark-ignited environment, a limited range of spark ignition tests were performed to interrogate flame speeds and knock onset compared to isooctane. A lower TDC pressure of 15 bar was used to allow time for flame propagation without autoignition; during the duration of the flame measurement, approximately 5 bar increase is observed (about 20% of total pressure rise from heat release), which will have some slowing effect on the flame, as increasing pressure has an inverse effect on flame speed. As shown above in Figure 4.3a-Figure 4.3c, the laser spark was able to create approximately spherical flames in the RCM under moderate to high temperatures, however, at lower temperature, the flame shape was often highly aspheric and the flame speed measurement suffers as a result; in lean or very low temperature cases, the processor was unable to provide any reliable measurement of flame

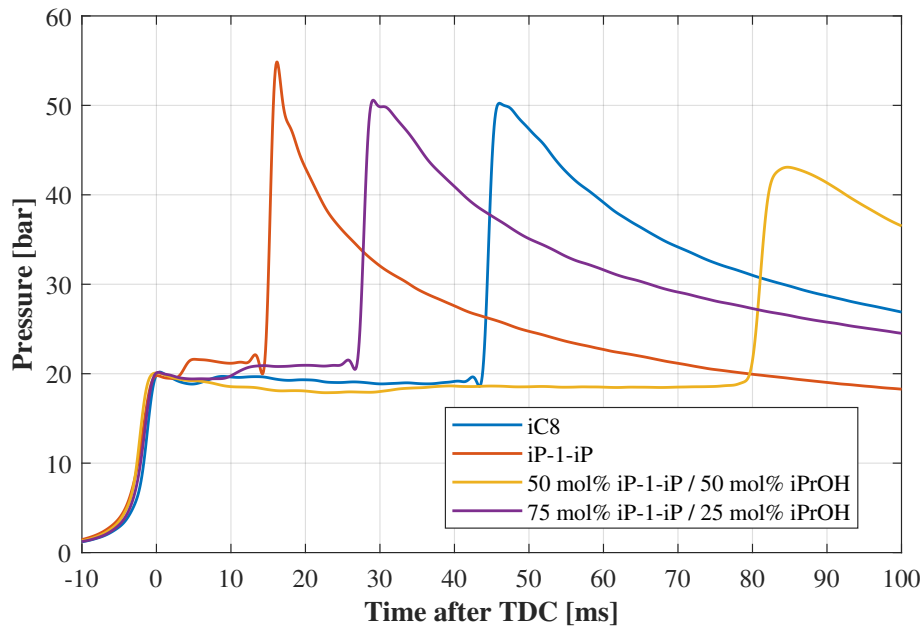


Figure 4.18: Sample pressure traces of isooctane, iP-1-iP, and 50 mol% and 75 mol% iP-1-iP/iPrOH blends in 5:1 nitrogen / oxygen gas mix. Noise at the base of the ignition event pressure rise is a filter artifact and is not present in the measured traces.

speed due to low propagation rates resulting in extreme interference from piston face turbulent vortices. In none of the cases are the flames truly spherical laminar flames and the flame speeds should not be assumed to be accurate to at 1-D laminar flame, however, the turbulent conditions and non-ideal expansion are nonetheless of relevance to engine operation.

Figure 4.20 shows the comparison of iC8 and iP-1-iP at engine-relevant temperatures. Within the error of this calculation, there is no apparent difference in flame speed between iC8 and iP-1-iP. At the $1000/T = 1.4$ condition, rich and lean tests were also performed. In the rich case, the iC8 flame speed is nearly identical to lean, and iP-1-iP had a small but non-negligible increase, from 33.1 ± 3.7 cm/s to 37.9 ± 4.9 cm/s (Table 4.1). The lean cases fell into the category of highly aspheric flames which the calculator could not extract a flame speed from, however, using the AHRR calculation, the time to end of combustion was identical within experimental error (36.0 ± 3.73 ms and 34.0 ± 3.50 ms for iC8 and iP-1-iP, respectively), indicating that at this lean condition, the flame speeds were once again comparable. A lower temperature test at $1000/T = 1.48$ also created aspheric flames which could not be measured, however, the iP-1-iP knocked

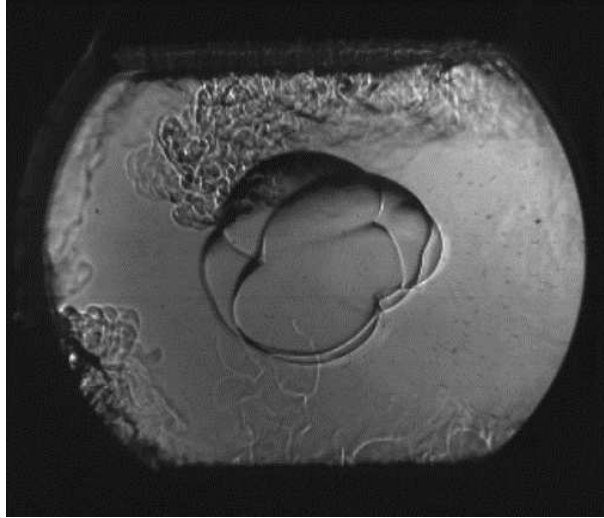


Figure 4.19: Aspheric flame from low temperature / low flame speed - 300 frames / 7.14 ms after spark

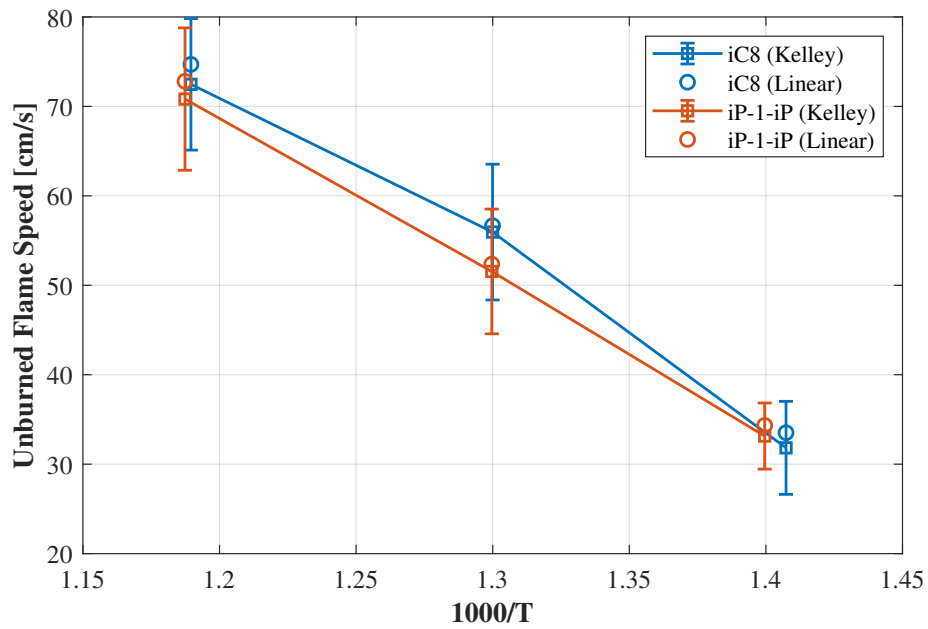


Figure 4.20: Comparison of unburned gas flame speeds of isooctane and iP-1-iP at engine-relevant temperatures, $P = 15$ bar, $\Phi = 1.0$. Square markers indicate Kelley stretch correction calculations, while circular markers indicate linear stretch correction.

Table 4.1: Flame speeds and density ratios at 15 bar TDC pressure as calculated for all tests (n/a indicates aspheric flames which could not be processed for speed).

Condition	iC8		iP-1-iP	
	Unburned Speed [cm/s]	ρ_u/ρ_b	Unburned Speed [cm/s]	ρ_u/ρ_b
1000/T = 1.5, Φ = 1.0	n/a	3.62	n/a	3.71
1000/T = 1.4, Φ = 0.7	n/a	2.84	n/a	2.92
1000/T = 1.4, Φ = 1.0	31.8	3.44	33.1	3.53
1000/T = 1.4, Φ = 1.3	32.3	3.38	37.9	3.52
1000/T = 1.3, Φ = 1.0	55.9	3.24	51.5	3.33
1000/T = 1.2, Φ = 1.0	72.4	3.05	70.8	3.12

Table 4.2: Comparison of knock effects on iP-1-iP compared to iC8 at similar conditions.

Condition	End of Comb. [ms]		Reduction in Comb. Duration	Heat Release During Knock
	iC8	iP-1-iP		
1000/T = 1.5, Φ = 1.0	36.8	25.6	30.6%	46% \pm 6.4
1000/T = 1.4, Φ = 0.7	36.0	34.0	5.5%	No Knock
1000/T = 1.4, Φ = 1.0	18.0	14.5	19.0%	24% \pm 4.2
1000/T = 1.4, Φ = 1.3	16.7	10.6	36.5%	62% \pm 4.6
1000/T = 1.3, Φ = 1.0	13.8	12.8	7.3%	37% \pm 4.2
1000/T = 1.2, Φ = 1.0	10.3	9.16	11.3%	40% \pm 1.6

at this condition and so end of combustion timing cannot be used as a reasonable comparison of flame propagation.

Knocking was observed for all iP-1-iP spark ignition tests except the lean condition at 1000/T = 1.4, and accounted for an average of 42% of the calculated heat release using the knock onset calculation noted in 4.1.3. No knocking was observed in any iC8 tests. Table 4.2 describes the knock conditions of each test case, where the reduction in combustion duration is measured as the reduction in time for dP/dt to become negative (end of heat release) for iP-1-iP vs iC8. The rich case demonstrated very strong knock compared to the stoichiometric cases, with more than half of the heat release occurring after knock onset. Three of the stoichiometric cases have, within experimental error, approximately 40% of the heat release occurring after knock onset; it is not clear why the heat release post-knock is much lower for the 1000/T = 1.4 test case. The heat release after knock onset tracks with changes in IDT, however, this is counter-intuitive, as

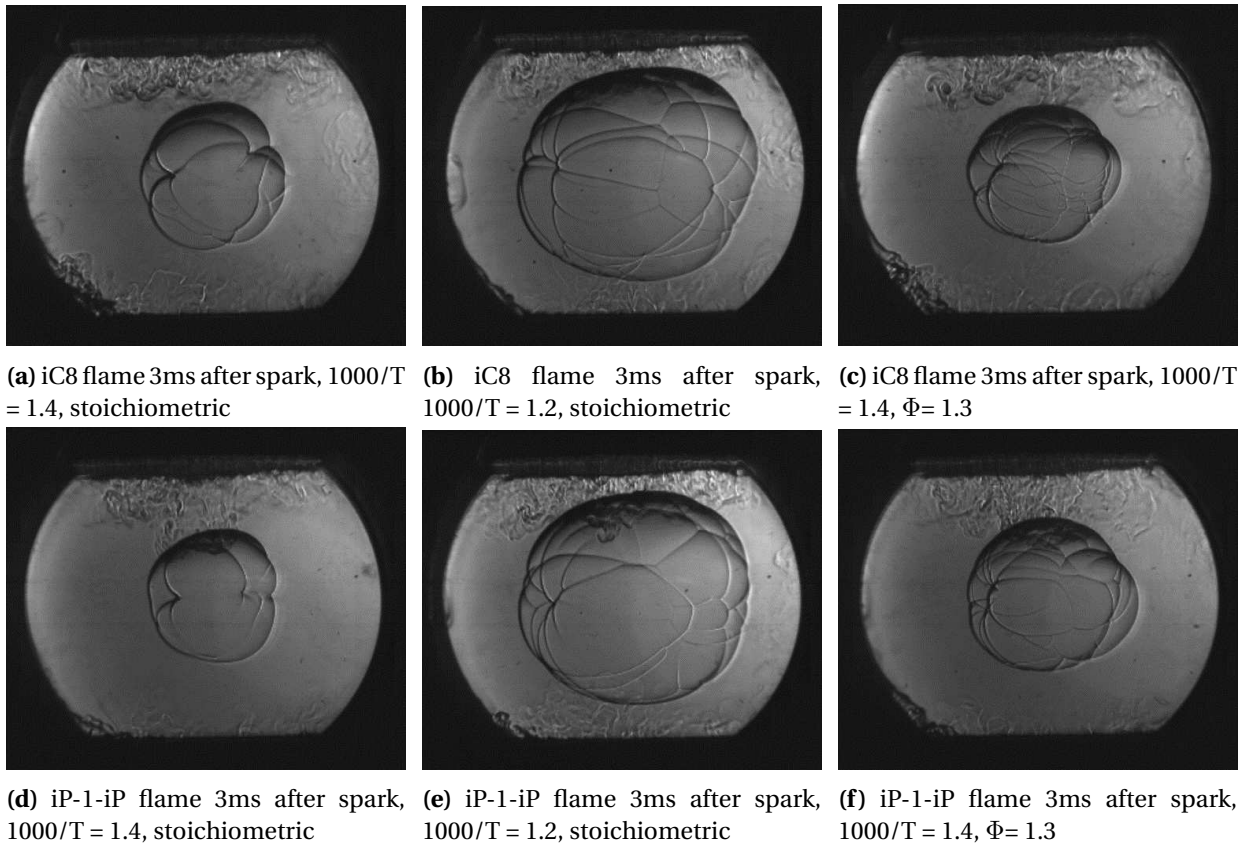


Figure 4.21: Representative Schlieren images of flamefronts 3 ms after spark, showing flame wrinkling at various conditions.

the cases with lower IDT should reasonably have higher, not lower, knock tendencies. Further study would be warranted to determine the causes of this unusual behavior.

Flame wrinkling at the tested conditions is slightly but noticeably higher for the iC8 than iP-1-iP flames, with minimal flame wrinkling at lower temperatures and equivalence ratios, but more prevalent at high temperature or rich conditions; see Figure 4.21a-Figure 4.21f. Flame wrinkling occurs when the Lewis number $Le = \alpha/D$ departs from 1, that is, when heat transfer from the flame into the reactants and reactant diffusion into the flame are unbalanced. The higher concentration of fuel in the rich combustion condition will contribute to a lower D due to lower diffusivity of the larger molecules, causing higher wrinkling. The minor wrinkling of the flame does not create flamefronts which significantly deviate from the spherical-flame simplification used in the flame speed calculation. Additionally, as the flame images show, interactions

Table 4.3: Octane number of iP-1-iP and 85 vol% iP-1-iP / 15 vol% iPrOH (iP-1-iP/85), expected accuracy ± 0.5 ON, except iP-1-iP RON, which was not a stable combustion condition and RON could not be accurately identified.

Fuel	RON	MON	(R+M)/2
iP-1-iP	49.9 (49.0-63.5)	67.9	58.9
iP-1-iP/85	92.5	86.1	89.3

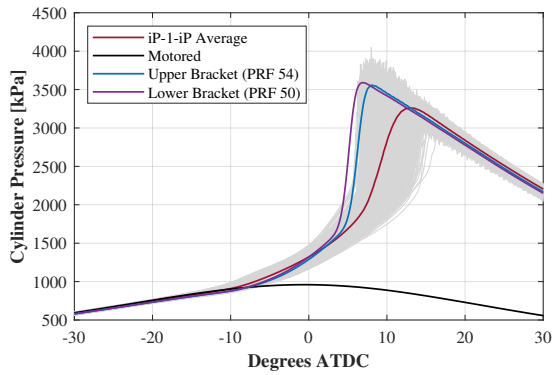
of the flamefront with the turbulence created at the piston face is minimal and does not appear to affect the spherical-flame simplification. As these vortices appear only in the center of the image, rather than around the full circumference, it is assumed that these are formed at the center of the piston face, as opposed to roll-up vortices that can be formed around the circumference of non-creviced pistons.

4.3.3 CFR Engine

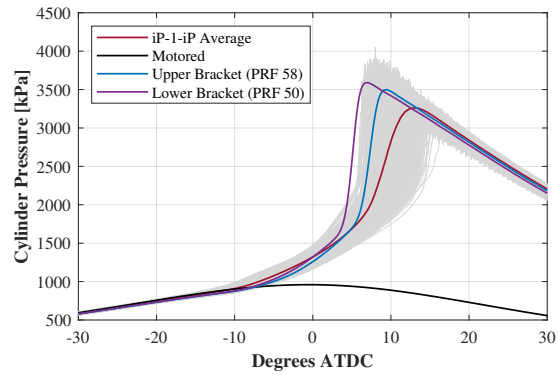
Tests on neat iP-1-iP and a iP-1-iP/iPrOH blend were performed in the CFR engine to determine RON and MON of these fuels and evaluate engine behaviors while operating with these oxygenated fuels. As both iP-1-iP and the blended fuel were expected to produce $ON < 100$, only nC7 / iC8 primary reference fuels (PRFs) were used in the ON bracketing methods – no toluene standardization fuel or tetraethyllead was required. Table 4.3 describes the measured ON. The fuel blend, iP-1-iP/85, is a blend of 85 vol% iP-1-iP and 15 vol% iPrOH. This was selected via interpolation between the iP-1-iP/iPrOH blends tested for IDT in the RCM, where a 30-35 mol% blend of iPrOH should approach iC8 IDT. Conversion of 30 mol% to vol% would indicate a desired 16 vol%, which was rounded to 15 vol% for simplicity in fuel blending.

Neat iP-1-iP is, as expected from its higher reactivity than iC8, is a low-ON, high-knock fuel, and is unsuitable on its own for use in modern SI engines. iP-1-iP/85 provides ON that approximates common commercial mid-grade gasoline, which has ON (as measured by (R+M)/2) of 89-90.

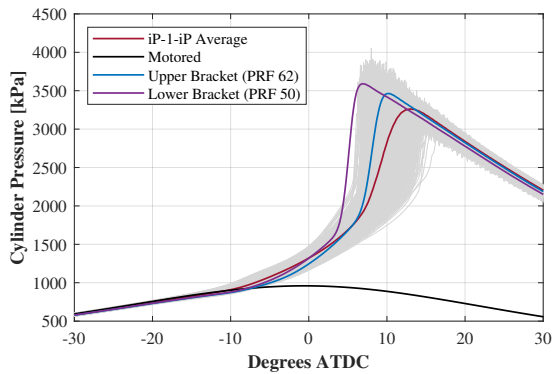
iP-1-iP displays a negative octane sensitivity $S = -18$, where $S = RON - MON$, which is typically a feature of fuels with NTC behavior, which includes many non-cyclic alkanes, and occurs



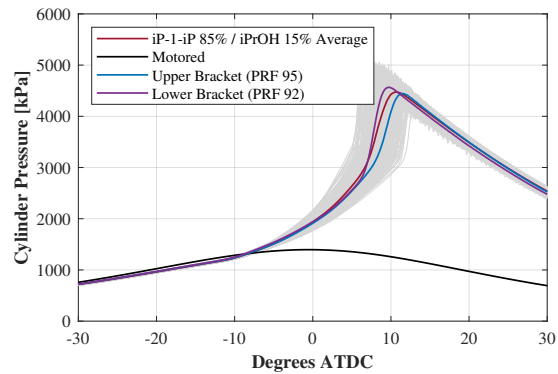
(a) iP-1-iP RON test, with PRF 50 and PRF 54 bracketing fuels



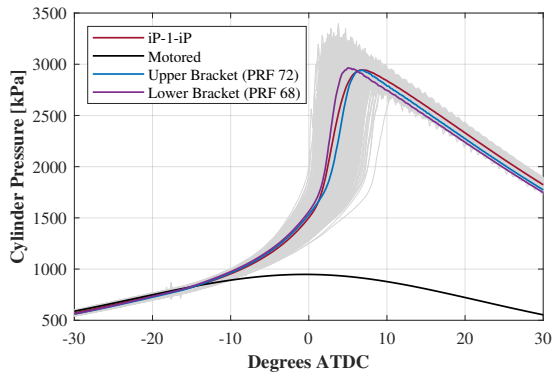
(b) iP-1-iP RON test, with PRF 50 and PRF 58 bracketing fuels



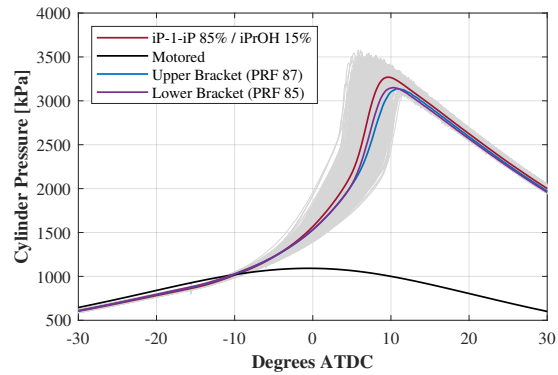
(c) iP-1-iP RON test, with PRF 50 and PRF 62 bracketing fuels



(d) iP-1-iP/85 RON test, with PRF 92 and PRF 95 bracketing fuels



(e) iP-1-iP MON test, with PRF 68 and PRF 72 bracketing fuels



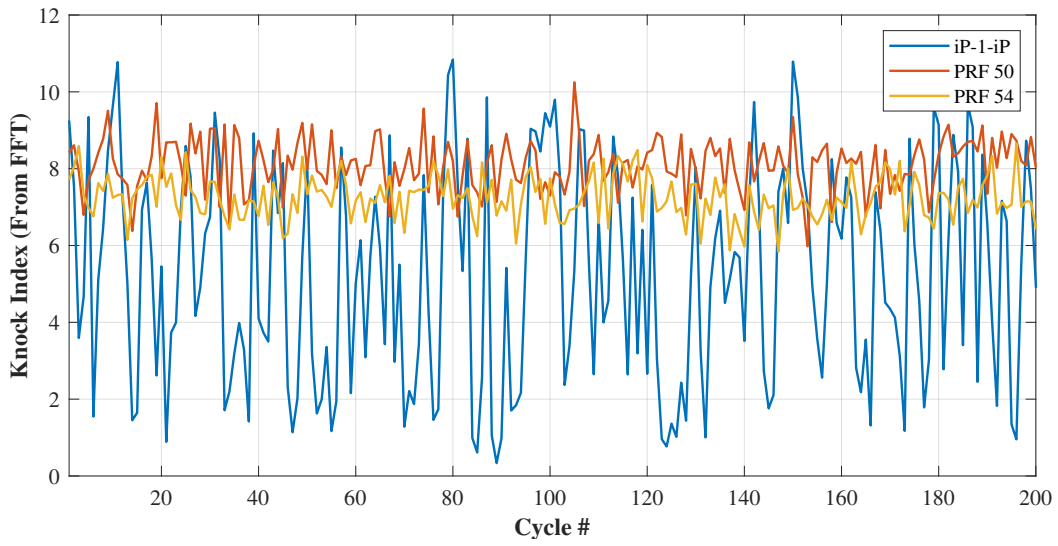
(f) iP-1-iP/85 MON test, with PRF 85 and PRF 87 bracketing fuels

Figure 4.22: iP-1-iP sample cycles from CFR tests

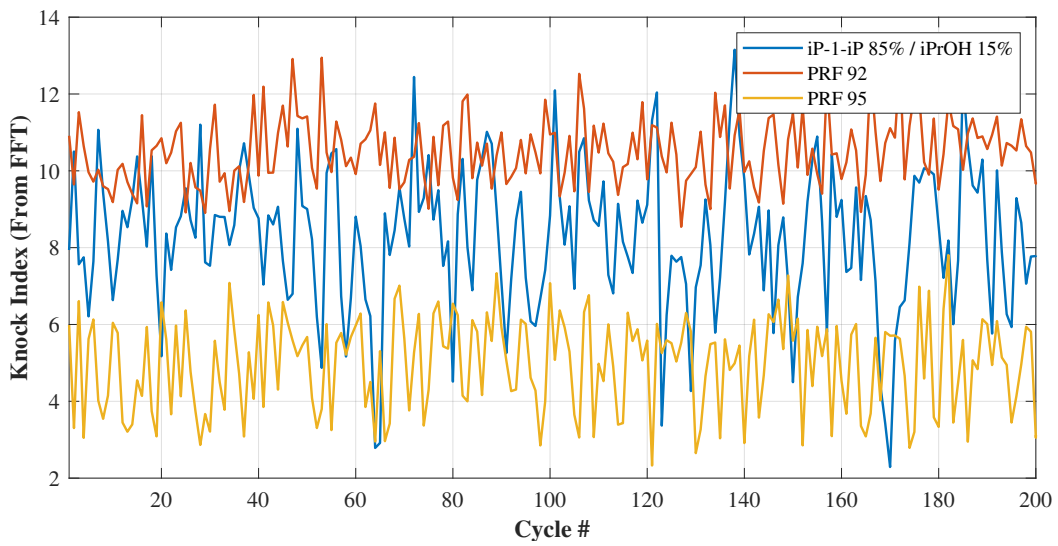
if the RON test occurs at a temperature/pressure point which lands near the local minimum IDT in the low-temperature region, while the subsequent MON test can occur on the increasing (NTC) region [146]. The RON test is a lower-temperature test than MON; using motored pressure traces and assuming a specific heat ratio of the fuel/air mixture of approximately 1.3, the iP-1-iP RON TDC temperature should be approximately 500 K, while the MON test has a TDC temperature of approximately 670 K. This further confirms the trend seen in Fig. 4.16, where iP-1-iP is found to be the first OME with confirmed NTC behavior.

A notable feature of the neat iP-1-iP ON testing is the extreme instability of the combustion. Figure 4.24 shows the KI of the individual cycles from the first 200 cycles of each test; it can be seen that the iP-1-iP RON test has extreme cycle-to-cycle variation. Most of the test runs had coefficients of variance in peak pressure and IMEP which were nearly invariant with respect to fuel, so the knock index is independent of the number of cycles sampled, from the 100 highest-knock (by FFT value) cycles, up to all of the 5000 saved cycles. For iP-1-iP in the RON operating condition, the CoV in peak pressure is approximately 3.9%, roughly 4x higher than the 0.9% of the PRFs used for comparison. Thus, taking the 100 highest knock cycles yields a RON of 49.0, while all 5000 provides a much higher RON of 63.5. The other cases (iP-1-iP/85 RON, both MON) yield very similar results, $ON \pm 0.5$, without regard to the number of cycles selected for calculation as the KI, and the next highest difference in CoV of IMEP is the iP-1-iP/85 RON, where the iP-1-iP was 1.5x higher than the upper bracket. To account for the variance when calculating ON, a weighted average ON was calculated, where weights were applied as $1/n$, thus the highest knock cycles have the strongest effect on ON calculation.

It is not immediately clear why this behavior appears limited to the iP-1-iP RON test only. The most likely cause is insufficient evaporation. For the iP-1-iP/85 RON test, a higher compression ratio was used, resulting in higher compressed temperature. Due to the high elevation and subsequent low intake pressure, ASTM D2699 corrects for this by requiring a lower intake temperature – 11.5°C – than the standard 52°C. At the lower compression for iP-1-iP compared to iP-1-iP/85, the compressed temperature is 500 K vs 550 K; this may be insufficient for com-

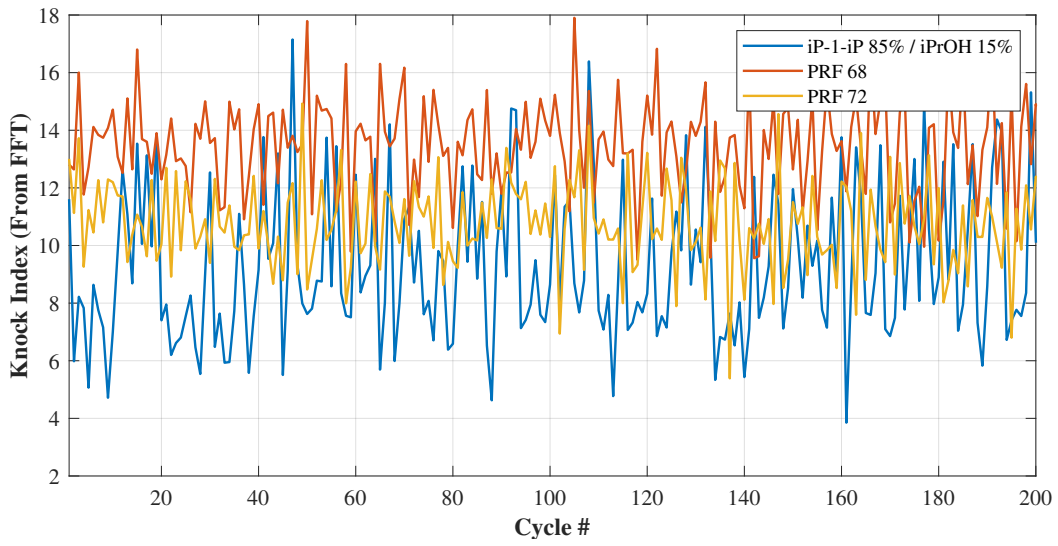


(a) KI from cycles 1-200 of iP-1-iP RON test, with PRFs 50, 54, 58, and 62

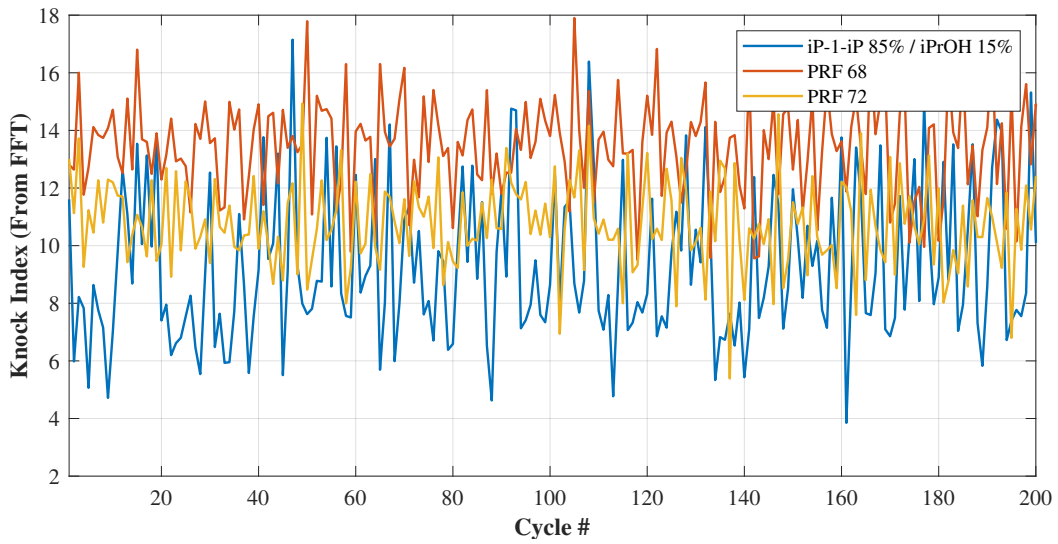


(b) KI from cycles 1-200 of iP-1-iP/85 RON test, with PRF 92 and PRF 95

Figure 4.23: KI comparison across 200 cycles for different CFR tests



(a) KI from cycles 1-200 of iP-1-iP MON test, with PRF 68 and PRF 72



(b) KI from cycles 1-200 of iP-1-iP/85 MON test, with PRF 85 and PRF 87

Figure 4.24: KI comparison across 200 cycles for different CFR tests

plete evaporation and mixing, resulting in a more stratified charge, possibly with some liquid droplets, for iP-1-iP specifically. This may contribute to the higher variance in knock at this condition. To correct for this, tests may need to be run by an external laboratory at lower elevation, where the intake temperature can be higher to promote full evaporation.

4.3.4 Chemical Origins of iP-1-iP NTC

No chemical kinetic modeling was performed for this work, however, past work on iP-1-iP, iPrOH, and other OMEs, particularly diethoxymethane, can provide insight into the chemical origin of the unique NTC of iP-1-iP. The established general cause of NTC in typical alkanes is a competition between ROO• branching pathways and alkene formation after an initial H abstraction, where at higher temperatures ROO• decomposes to R• and O₂ rather than permitting a chain-branching process, while the alkene pathway is a chain propagation pathway through the less reactive HO₂• which results in slower ignition but is favored at higher temperatures [146, 147]. Further, the lower reactivity of branched alkanes compared to linear alkanes stems from the higher energy barriers for internal isomerization to a •ROOH structure, required for further O₂ addition and subsequent OH• formation and chain branching.

The current frontier of chemical kinetics for oxymethylene ethers is the extended-alkyl OME diethoxymethane, C₂H₅OCH₂OC₂H₅, which has two published comprehensive (inclusive of low temperature chemistry) kinetic mechanisms, from Li et al [46] and Jacobs et al. [47]. Both Li and Jacobs demonstrate that the ROO• pathways are equally relevant for oxymethylene ethers, with internal isomerization as an important step much like alkanes. Li et al. show a number of different possible transition states for the internal isomerization process, and show that there are four likely transition states arising from radicals originating with H abstraction from either the primary or secondary carbons in the ethyl groups, while abstraction from the carbon in the oxymethylene group has only two probable transition states. Jacobs also shows various pathways for the three different initial radicals, wherein the internal isomerizations and subsequent

•OOQOOH formation dominate at low to moderate temperatures, again consistent with alkane behavior.

In prior work, the authors discuss probable chemical causes of the lower reactivity of iP-1-iP compared to linear OMEs such as E-1-E or iP-1-iP's linear counterpart, P-1-P. Guo et al. studied the abstraction behaviors of n- and iso-propanol, and note that at low temperatures, the α carbon (connected to the OH group) is the primary abstraction source for temperatures below approximately 1000 K [138]; from this, we postulated that this behavior is similar to abstraction from iP-1-iP, wherein the highly crowded nature of this preferred abstraction site reduces overall reaction rates by inhibiting O₂ addition and subsequent reaction cascade. Further, Li et al. and Jacobs et al., as discussed above, show that there are limited transition states available for RO₂ cascades when the initial abstraction from an OME occurs from the central (oxymethylene) carbon. When combined with limited H abstraction and O₂ addition on the isopropyl alkyl group, generally lower reaction rates are to be expected at both low and high temperatures. Further, Jacobs demonstrates a higher probability of RO₂ reactions with HO₂ at low temperatures from this central abstraction radical, consuming a radical rather than branching or propagating. These combined behaviors may be the basis for the observed low reactivity and NTC behavior of the iP-1-iP molecule compared to linear OMEs. Dedicated modeling efforts would be required to verify these proposals.

Chapter 5

Conclusions

In the course of this work, many different OMEs have been used, synthesized, and studied for fuel and combustion related purposes. At a high level, the most important conclusion is this: OMEs as a class are generally excellent fuels or additives for the purpose of reducing soot production with respect to total combustion energy. The exact selection of an OME for a given purpose will be very context-dependent, and there are some fuel applications where the properties of OMEs outside of their soot reduction potential preclude their usage in certain applications.

5.1 Summary of Findings

Several types of OMEs were synthesized during this work. In the case of formation of a simple, $n=1$ OME, there are two pathways for production. In the first, M-1-M is reacted with an higher alcohol X-OH in a trans-acetalization reaction to form a target X-1-X, along with a partially-exchanged asymmetric OME M-1-X, with MeOH as an additional reaction product. This method, of course, cannot be used to form M-1-M; this must be made in the second pathway. The second path is an acetalization reaction, where an alcohol X-OH is reacted with a formaldehyde source to produce X-1-X and water. Both reactions can be performed in acidic environments; in this work we use ion exchange resin Amberlyst 15 as the catalyst. Both reactions can be performed at moderate temperatures, with Pathway 1 being successfully performed between 40°C-80°C, while Pathway 2 was performed at 60°C-100°C, where the 40°C case was insufficient to fully decompose trioxane to formaldehyde. The first pathway has fast reaction rates, but is hindered by low molar production of the target X-1-X, which is produced at approximately 10 mol% of the equilibrium concentration, while the partially exchanged product M-1-X occurs at twice this fraction, at a 2:1 X-OH : M-1-M stoichiometric ratio in the reactants. The second pathway has lower reaction rates, but shows higher mol fraction yields of the target

product at 2:1 X-OH : CH₂O reactant stoichiometry. The usefulness of this pathway is offset by the necessary production of water, and the equilibrium presence of formaldehyde, which is not fully consumed. For use as fuels, both must be treated, via distillation or otherwise, to remove undesired components. Production of extended-chain OMEs can occur at similar moderate conditions in the same acidic catalyzed environment. Chain extension occurs through the addition of CH₂O groups to X-n-X to produce X-(n+1)-X, where the equilibrium yield of various chain lengths is exponentially decreasing with increasing n. At the conditions used for OME production here (80°C and 0.64 min⁻¹), the yields of various lengths was largely similar across the the various alkyl groups, where $n=1$ accounted for half of the products, $n=2$ less than 25%, $n=3$ slightly greater than 10%, and so on. As the property testing identified B-(2-4)-B as an ideal diesel substitute, a large quantity of this mixture was synthesized via the chain extension method for engine testing and external laboratory validation.

Sixteen different OMEs were tested on a broad range of fuel-relevant properties. Some of these have had a subset of the tested properties already documented in literature, but a variety of untested OMEs along with new tests and properties for previously documented OMEs greatly expand the available data on the fuel properties of extended OMEs. The Indicated Cetane Number, a crucial measure for CI fuels, is tested, and it is shown that for US and EU compatibility (ICN>51 for EU), all OMEs other than M-1-M and iP-1-iP are acceptable. Further, B-n-B is shown to have ICN independent of n , a useful characteristic which should improve ignition uniformity across various blend ratios. A blend study of B-1-B in diesel shows that B-1-B follows a known trend wherein ether blending has a nonlinear effect on ICN with respect to blend ratio, suppressing ICN to slightly (<5%) below a linear prediction. As is expected of oxygenated fuels, all OMEs showed reduced LHV compared to diesel, with the lower oxygen content OMEs performing the best. The soot reduction potential of methyl-terminated OMEs is well documented in literature; here it is shown that, even when corrected for LHV, higher alkyl OMEs, including the worst performer, iB-1-iB, are a significant improvement over diesel. The flash point of OMEs is most strongly linked to molecular weight; many lighter OMEs have FP too low for safe diesel

use, however, heavier alkyl groups and longer chain lengths improve flash point to safe levels for diesel use. The density and viscosity of OMEs followed the general trend of lower viscosity and higher density than diesel; the lower viscosity can promote droplet breakup in sprays and the higher density can offset slightly the lower LHVs of OMEs. No apparent trend in oxidative stability is seen for end groups, however, longer end groups tend to promote higher autooxidative stability. One of the largest differences between various alkyl groups arises in the water solubility. M-n-M OMEs have a significant weakness in their very high water solubility, here is determined to be on the order of 300-500g/L depending on n ; extending the alkyl groups produces order-of-magnitude reductions with each extension of alkyl group, to the point where B-n-B has water solubility approximately 0.2-0.3 g/L, of the same order of magnitude to diesel (about 0.1 g/L). This could have significant impacts on environmental effects due to the improved ability to isolate and clean up spills, compared to M-n-M. Another known weakness of OMEs is their high absorption into common elastomers and polymers, which could have deleterious effects on engine and fuel sealing systems. Tests with $n=1$ OMEs show that silicone is equally affected by OMEs with various end groups, while nitrile rubber shows somewhat reduced absorption with longer end groups, and FKM (“Viton”) showed significant decrease in absorption with longer end groups. Polyether-ether-ketone, a common hard polymer for valve seats, was shown to be entirely resistant to OME absorption or surface degradation. Nitrile appears to leach into OMEs, causing discoloration in all tests.

For external verification of the applicability of the chosen blend, 30 vol% of a 200°C-300°C distillation cut of B-n-B (approximately B-(2-4)-B) in cert diesel was sent to an external laboratory (FOI Laboratories, Vancouver, WA) to be tested with a battery of tests for ASTM D975 compliance. It is shown that this blend meets all ASTM D975 standards except for lubricity, where the lubricity is lower than required. A sample of this fuel blend was left in a flask for six months and shown to be fully miscible, with no apparent phase separation.

Engine testing of heavier, butyl- and propyl-terminated OMEs in a Deere Tier 3 4.5L CI engine indicate good drop-in operability of these fuels, with the engine performing at similar effi-

ciency to diesel with no changes to the engine maps. Combustion timing was similar between diesel and OMEs, with comparable CA10 and CA50 timing, and the CA90 timing dependent on LHV. Fuel consumption naturally increased with the lower LHV of OMEs and OME blends, but lower CO emissions indicated superior combustion efficiency. PM_{2.5} emissions were significantly reduced compared to diesel for all OME blends, and the typical PM/NO_x tradeoff was broken, where the PM emissions decrease (as a %) was significantly stronger than the NO_x increase.

Fundamental combustion tests were performed for a subset of the OMEs in a rapid compression machine, and one (iP-1-iP) was also tested in a CFR engine for SI engine applicability. E-1-E, E-2-E, P-1-P, and iP-1-iP were tested in highly dilute conditions (12:1 inert:O₂, selected for consistency with past dilute OME literature), where it was shown that the three linear OMEs had qualitatively similar ignition behavior, at similar orders of magnitude to n-heptane, but without NTC. Instead, they showed regions of decreased dependence of ignition delay on temperature, verging on complete temperature independence. The three linear OMEs also demonstrated first stage ignition behavior, consistent with literature on E-1-E. In this test, iP-1-iP was unable to ignite in the measured duration (400 ms) at the 20 bar target pressure; increase to 30 bar provided high-temperature ignition at similar IDT to P-1-P at 20 bar. Comparison with a simulation of isooctane at similar conditions indicated lower reactivity than isooctane. This, combined with an exceptionally low ICN of 11, led to an investigation of iP-1-iP at several conditions to probe its potential applicability as a SI fuel. An autoignition sweep at more engine-relevant conditions (5:1 inert ratio, approximately equivalent to 25% EGR) of iP-1-iP and iC8 indicates that at these conditions, iP-1-iP has 5-10x shorter IDT than iC8. Blending with iPrOH, a necessary step in the synthesis, was able to match iC8 ignition. Laser-ignited flame speeds showed essentially identical flame speeds for the two fuels, albeit with knock detected for all but the lean iP-1-iP cases, with iC8 not knocking at all during the laser spark tests. Finally, CFR engine testing was performed to evaluate the octane numbers of iP-1-iP; it shows poor ON with a pump rating (R+M)/2 of 65.4 and a negative sensitivity, consistent with the observed NTC be-

havior of this fuel. 15 vol% iPrOH in iP-1-iP was able to produce a mid-grade pump rating of 89.3, acceptable for current SI engines. The NTC behavior and low reactivity relative to other OMEs is postulated to arise from low probability of O₂ addition to the α C of the alkyl group, leading to RO₂ cascading only from the central carbon on the oxymethylene group.

5.2 Limitations and Areas for Future Work

This work has several limitations, which may lead to potential areas of future work for extension of the study here. The limitations arise primarily as a result of the broad-based nature of this study, which probes a large number of fuel-relevant properties and behaviors of OMEs, but does not drill down into the deep detail of any one particular behavior. In particular, chemical kinetics is an area where significant work could be done, both for synthesis and for combustion. It is shown here that OMEs can be produced for laboratory-scale property and engine testing using reasonably simple equipment and inexpensive catalysts and reactants, however, the focus of synthesis lay in supporting the property and combustion characterization, leaving an opening for future work investigating the detailed kinetics of different catalysts, reactant combinations, and model types to account for various inhomogeneities. Similarly, while much fundamental combustion studies provided some data to collaborators at CU Boulder, the actual quantum chemistry calculations required to model these new fuels and their reactions is well outside the scope of this work and requires specific skills which would be best left to a future dissertation dedicated to these calculations. Additionally, the laboratory-scale nature of the work presented here does not necessarily reflect how industrial production or use of OMEs would occur, e.g. removal of formaldehyde from equilibrium products is not likely to be performed via hand-mixing of a buffer solution and subsequent phase separation in a funnel. Pilot-scale models of real systems would more accurately demonstrate the potential industrial feasibility.

In addition to the possible work described above to rectify some of the limitations of this work, new work to build upon this study could encompass a number of options, but of particular interest is continuing the fundamental combustion studies to work with more OME

molecules. B-1-B, for example, was excluded from the RCM studies due to its low vapor pressure and subsequent risk of condensation in fill lines or on internal RCM surfaces. Higher-temperature mixing and improved fill lines could reduce this risk and allow more testing; also flame speeds could be evaluated for more fuels at a wider and higher resolution temperature range. iP-1-iP is on its own not an appropriate gasoline, but it is proposed to be a potential soot-reduction additive for gasoline in lower quantities, or as a sensitivity reducer for higher-sensitivity fuels. This could be investigated with various gasoline surrogate blends or pump gasoline samples, and emissions monitoring could be performed to determine the PM reduction effects of low-volume blending.

5.3 Recommendations for OME Selection

One of the major takeaways of this study is that OME selection for fuel blending or direct usage is a balance of various interests, e.g. soot reduction and water solubility reduction work in direct opposition. A blend of 30 vol% B-(2-4)-B in diesel was selected as an ideal legacy-compatible mixture, as discussed above, but for other interests there may be better selections.

M-n-M has been studied throughout the literature for soot reduction; here we show that this remains the best choice for this purpose. OMEs with larger alkyl groups still show reductions in soot per energy with respect to diesel, but M-n-M effectively eliminates all soot production if used neat. If using M-n-M in an engine, however, care must be taken to use longer oligomers, as M-1-M and M-2-M pose handling risks due to low flash point and low cetane number; additionally, significant spill mitigation efforts must be made due to the very high water solubility and subsequent difficulty of spill containment. Ethyl-terminated OMEs show some improvement over methyl-terminated, but generally are not ideal for many purposes. While there is some flash point and cetane number increase, water solubility remains high, flash point of shorter chains remains low, and generally all properties are not optimized for either diesel or SI use. Propyl-terminated OMEs may be of some value as jet fuel additives if oxygenates are permitted, as their moderate molecular weights place P-n-P in the light kerosene range, and while

still too volatile for current diesel standards, better LHV and low water solubility would support their use in targeted applications. B-n-B remains the best selection for legacy compatibility due to its higher LHV, low water solubility, stable ICN across chain length, and low volatility and molecular weights in the diesel range. In summary:

- For best soot reduction: M-n-M
- For best legacy diesel engine compatibility: B-n-B
- For mobile applications where fuel capacity is a concern: B-n-B with a preference for lower n
- For lowest spill containment risk: B-n-B
- For spark ignition usage: iP-1-iP, but in limited quantity as a blendstock or in tandem with an octane booster, e.g. iPrOH

OMEs have many potential fuel applications, when selected and matched to the engine correctly. Future studies may expand on engine performance, emissions reduction, or other engine-relevant considerations as industry broadens its alternative fuels catalog.

References

- [1] J. B. Heywood, *Internal Combustion Engine Fundamentals*, 2nd Edition, McGraw-Hill Education, 2018.
- [2] International Energy Agency, *The Future of Trucks*, 2017.
- [3] C. Cunanan, M.-K. Tran, Y. Lee, S. Kwok, V. Leung, M. Fowler, A review of heavy-duty vehicle powertrain technologies: Diesel engine vehicles, battery electric vehicles, and hydrogen fuel cell electric vehicles, *Clean Technologies* 3 (2) (2021) 474–489.
- [4] M. Williams, R. Minjares, A technical summary of euro 6/vi vehicle emission standards, Tech. rep., International Council on Clean Transportation (2016).
- [5] R. Sun, I. Delidovich, R. Palkovits, Dimethoxymethane as a cleaner synthetic fuel: Synthetic methods, catalysts, and reaction mechanism, *ACS Catalysis* 9 (2) (2019) 1298–1318.
- [6] J. Masamoto, J. Ohtake, M. Kawamura, Process for producing formaldehyde and derivatives thereof, uS Patent 4,967,014 (Oct. 30 1990).
- [7] S. Satoh, Y. Tanigawa, Process for producing methylal, uS Patent 6,379,507 (Apr. 30 2002).
- [8] D. Oestreich, L. Lautenschütz, U. Arnold, J. Sauer, Reaction kinetics and equilibrium parameters for the production of oxymethylene dimethyl ethers (ome) from methanol and formaldehyde, *Chemical Engineering Science* 163 (2017) 92–104.
- [9] K.-a. Thavornprasert, M. Capron, L. Jalowiecki-Duhamel, F. Dumeignil, One-pot 1, 1-dimethoxymethane synthesis from methanol: a promising pathway over bifunctional catalysts, *Catalysis Science & Technology* 6 (4) (2016) 958–970.
- [10] N. Schmitz, J. Burger, H. Hasse, Reaction kinetics of the formation of poly (oxymethylene) dimethyl ethers from formaldehyde and methanol in aqueous solutions, *Industrial & Engineering Chemistry Research* 54 (50) (2015) 12553–12560.

- [11] N. Schmitz, F. Homberg, J. Berje, J. Burger, H. Hasse, Chemical equilibrium of the synthesis of poly (oxymethylene) dimethyl ethers from formaldehyde and methanol in aqueous solutions, *Industrial & Engineering Chemistry Research* 54 (25) (2015) 6409–6417.
- [12] X. Zhang, S. Zhang, C. Jian, Synthesis of methylal by catalytic distillation, *Chemical engineering research and design* 89 (6) (2011) 573–580.
- [13] H. Liu, E. Iglesia, Selective oxidation of methanol and ethanol on supported ruthenium oxide clusters at low temperatures, *The Journal of Physical Chemistry B* 109 (6) (2005) 2155–2163.
- [14] A. T. To, T. J. Wilke, E. Nelson, C. P. Nash, A. Bartling, E. C. Wegener, K. A. Unocic, S. E. Habas, T. D. Foust, D. A. Ruddy, Dehydrogenative coupling of methanol for the gas-phase, one-step synthesis of dimethoxymethane over supported copper catalysts, *ACS Sustainable Chemistry & Engineering* 8 (32) (2020) 12151–12160.
- [15] D. Kocis, K. Song, H. Lee, T. Litzinger, Effects of dimethoxymethane and dimethylcarbonate on soot production in an optically-accessible diesel engine, *SAE transactions* (2000) 2299–2308.
- [16] J. C. Ball, C. Lapin, J. Buckingham, E. Frame, D. Yost, J. Garbak, M. A. González D, E. Liney, M. Natarajan, J. P. Wallace III, Dimethoxy methane in diesel fuel: part 1. the effect of fuels and engine operating modes on emissions of toxic air pollutants and gas/solid phase pah, *SAE transactions* (2001) 2176–2192.
- [17] Y. Ren, Z. Huang, D. Jiang, L. Liu, K. Zeng, B. Liu, X. Wang, Engine performance and emission characteristics of a compression ignition engine fuelled with diesel/dimethoxymethane blends, *Proceedings of the Institution of Mechanical Engineers, Part D: Journal of Automobile Engineering* 219 (7) (2005) 905–914.

- [18] Y. Ren, Z. Huang, D. Jiang, L. Liu, K. Zeng, B. Liu, X. Wang, Combustion characteristics of a compression-ignition engine fuelled with diesel–dimethoxy methane blends under various fuel injection advance angles, *Applied thermal engineering* 26 (4) (2006) 327–337.
- [19] Z. Huang, Y. Ren, D. Jiang, L. Liu, K. Zeng, B. Liu, X. Wang, Combustion and emission characteristics of a compression ignition engine fuelled with diesel–dimethoxy methane blends, *energy conversion and management* 47 (11-12) (2006) 1402–1415.
- [20] R. Zhu, X. Wang, H. Miao, Z. Huang, J. Gao, D. Jiang, Performance and emission characteristics of diesel engines fueled with diesel-dimethoxymethane (dmm) blends, *Energy & Fuels* 23 (1) (2009) 286–293.
- [21] R. Zhu, X. Wang, H. Miao, Z. Huang, Combustion and particulate emission characteristics of a diesel engine fuelled with diesel—dimethoxymethane blends, *Proceedings of the Institution of Mechanical Engineers, Part D: Journal of Automobile Engineering* 224 (4) (2010) 521–531.
- [22] B. Deepanraj, G. Sankaranarayanan, N. Senthilkumar, M. Pugazhivadivu, Influence of dimethoxymethane addition on performance, emission and combustion characteristics of the diesel engine, *International Journal of Ambient Energy* 38 (6) (2017) 622–626.
- [23] K. Bhaskar, L. Sassykova, M. Prabhakar, S. Sendilvelan, Effect of dimethoxy-methane (c3h8o2) additive on emission characteristics of a diesel engine fueled with biodiesel, *International Journal of Mechanical and Production Engineering Research and Development* 8 (1) (2018) 399–406.
- [24] W. Qian, H. Huang, M. Pan, R. Huang, J. Wei, J. Liu, Analysis of morphology, nanostructure, and oxidation reaction of soot particulates from ci engines with dimethoxymethane–diesel blends under different loads and speeds, *Fuel* 278 (2020) 118263.

- [25] M. Pan, W. Qian, Y. Wang, C. Wu, H. Huang, Effect of dimethoxymethane (dmm) additive on combustion and emission characteristics under different working conditions in ci engines, *Fuel* 284 (2021) 119304.
- [26] C. J. Baranowski, A. M. Bahmanpour, O. Kröcher, Catalytic synthesis of polyoxymethylene dimethyl ethers (ome): A review, *Applied Catalysis B: Environmental* 217 (2017) 407–420.
- [27] R. Wang, Z. Wu, Z. Qin, C. Chen, H. Zhu, J. Wu, G. Chen, W. Fan, J. Wang, Graphene oxide: an effective acid catalyst for the synthesis of polyoxymethylene dimethyl ethers from methanol and trioxymethylene, *Catalysis Science & Technology* 6 (4) (2016) 993–997.
- [28] Q. Wu, M. Wang, Y. Hao, H. Li, Y. Zhao, Q. Jiao, Synthesis of polyoxymethylene dimethyl ethers catalyzed by brønsted acid ionic liquids with alkanesulfonic acid groups, *Industrial & Engineering Chemistry Research* 53 (42) (2014) 16254–16260.
- [29] J. Burger, E. Ströfer, H. Hasse, Chemical equilibrium and reaction kinetics of the heterogeneously catalyzed formation of poly (oxymethylene) dimethyl ethers from methylal and trioxane, *Industrial & Engineering Chemistry Research* 51 (39) (2012) 12751–12761.
- [30] L. Lautenschütz, D. Oestreich, P. Seidenspinner, U. Arnold, E. Dinjus, J. Sauer, Physicochemical properties and fuel characteristics of oxymethylene dialkyl ethers, *Fuel* 173 (2016) 129–137.
- [31] M. Drexler, P. Haltenort, T. A. Zevaco, U. Arnold, J. Sauer, Synthesis of tailored oxymethylene ether (ome) fuels via transacetalization reactions, *Sustainable Energy & Fuels* 5 (2021) 4311–4326.
- [32] A. Omari, B. Heuser, S. Pischinger, C. Rüdinger, Potential of long-chain oxymethylene ether and oxymethylene ether-diesel blends for ultra-low emission engines, *Applied Energy* 239 (2019) 1242–1249.

- [33] J. Burger, M. Siegert, E. Ströfer, H. Hasse, Poly(oxymethylene) dimethyl ethers as components of tailored diesel fuel: Properties, synthesis and purification concepts, *Fuel* 89 (11) (2010) 3315–3319.
- [34] M. M. Maricq, R. E. Chase, D. H. Podsiadlik, W. O. Siegl, E. W. Kaiser, The effect of dimethoxy methane additive on diesel vehicle particulate emissions, *SAE transactions* (1998) 1504–1511.
- [35] K. D. Vertin, J. M. Ohi, D. W. Naegeli, K. H. Childress, G. P. Hagen, Methylal and methylal-diesel blended fuels for use in compression-ignition engines, Tech. rep., SAE International (2000).
- [36] D. Pélerin, K. Gaukel, M. Härtl, E. Jacob, G. Wachtmeister, Potentials to simplify the engine system using the alternative diesel fuels oxymethylene ether ome1 and ome3-6 on a heavy-duty engine, *Fuel* 259 (2020) 116231.
- [37] B. Lehrheuer, F. Hoppe, K. A. Heufer, S. Jacobs, H. Minwegen, J. Klankermayer, B. Heuser, S. Pischinger, Diethoxymethane as tailor-made fuel for gasoline controlled autoignition, *Proceedings of the Combustion Institute* 37 (4) (2019) 4691–4698.
- [38] T. Langhorst, O. Toedter, T. Koch, B. Niethammer, U. Arnold, J. Sauer, Investigations on spark and corona ignition of oxymethylene ether-1 and dimethyl carbonate blends with gasoline by high-speed evaluation of OH^* chemiluminescence, *SAE International Journal of Fuels and Lubricants* 11 (1) (2018) 5–20.
- [39] C. A. Daly, J. M. Simmie, P. Dagaut, M. Cathonnet, Oxidation of dimethoxymethane in a jet-stirred reactor, *Combustion and flame* 125 (3) (2001) 1106–1117.
- [40] V. Dias, J. Vandooren, Experimental and modeling studies of $C_2H_4/O_2/Ar$, $C_2H_4/methylal/O_2/Ar$ and $C_2H_4/ethylal/O_2/Ar$ rich flames and the effect of oxygenated additives, *Combustion and Flame* 158 (5) (2011) 848–859.

- [41] W. Sun, G. Wang, S. Li, R. Zhang, B. Yang, J. Yang, Y. Li, C. K. Westbrook, C. K. Law, Speciation and the laminar burning velocities of poly(oxymethylene) dimethyl ether 3 (pomdme3) flames: An experimental and modeling study, *Proceedings of the Combustion Institute* 36 (1) (2017) 1269–1278.
- [42] T. He, Z. Wang, X. You, H. Liu, Y. Wang, X. Li, X. He, A chemical kinetic mechanism for the low-and intermediate-temperature combustion of polyoxymethylene dimethyl ether 3 (pode3), *Fuel* 212 (2018) 223–235.
- [43] K. De Ras, M. Kusenbergh, J. W. Thybaut, K. M. Van Geem, Unraveling the carbene chemistry of oxymethylene ethers: Experimental investigation and kinetic modeling of the high-temperature pyrolysis of ome-2, *Proceedings of the Combustion Institute* (2022).
- [44] K. De Ras, M. Kusenbergh, G. Vanhove, Y. Fenard, A. Eschenbacher, R. J. Varghese, J. Aerssens, R. Van de Vijver, L.-S. Tran, J. W. Thybaut, K. M. Van Geem, A detailed experimental and kinetic modeling study on pyrolysis and oxidation of oxymethylene ether-2 (ome-2), *Combustion and Flame* 238 (2022) 111914.
- [45] K. P. Shrestha, S. Eckart, S. Drost, C. Fritsche, R. Schießl, L. Seidel, U. Maas, H. Krause, F. Mauss, A comprehensive kinetic modeling of oxymethylene ethers (omen, n= 1–3) oxidation-laminar flame speed and ignition delay time measurements, *Combustion and Flame* 246 (2022) 112426.
- [46] R. Li, J. M. Herreros, A. Tsolakis, W. Yang, Chemical kinetic modeling of diethoxymethane oxidation: A carbon-neutral fuel, *Fuel* 291 (2021) 120217.
- [47] S. Jacobs, M. Döntgen, A. B. S. Alqaity, R. Hesse, S. Kruse, J. Beeckmann, L. C. Kröger, P. Morsch, K. Leonhard, H. Pitsch, K. A. Heufer, A comprehensive experimental and kinetic modeling study of the combustion chemistry of diethoxymethane, *Energy & Fuels* 35 (19) (2021) 16086–16100.

- [48] S. Fisher, R. Kunin, Routine exchange capacity determinations of ion exchange resins, *Analytical chemistry* 27 (7) (1955) 1191–1194.
- [49] R. Kunin, E. Meitzner, J. Oline, S. Fisher, N. Frisch, Characterization of amberlyst 15. macroreticular sulfonic acid cation exchange resin, *Industrial & Engineering Chemistry Product Research and Development* 1 (2) (1962) 140–144.
- [50] Y. Zhang, L. Ma, J. Yang, Kinetics of esterification of lactic acid with ethanol catalyzed by cation-exchange resins, *Reactive and Functional Polymers* 61 (1) (2004) 101–114.
- [51] G. Yadav, M. Thathagar, Esterification of maleic acid with ethanol over cation-exchange resin catalysts, *Reactive and Functional polymers* 52 (2) (2002) 99–110.
- [52] J. Mitchell, J. Broyan, K. Pickering, N. Adam, M. Casteel, M. Callahahn, C. Carrier, Ion exchange technology development in support of the urine processor assembly precipitation prevention project for the international space station, in: *42nd International Conference on Environmental Systems*, 2012, p. 3427.
- [53] N. V. Vlasenko, Y. N. Kochkin, A. P. Filippov, T. G. Serebrii, P. E. Strizhak, Adsorption–desorption of ethanol on sulfonated resin catalysts for ethyl-tert-butyl ether synthesis, *Adsorption Science & Technology* 35 (7-8) (2017) 630–640.
- [54] S. Bajracharya, B. van den Burg, K. Vanbroekhoven, H. De Wever, C. J. Buisman, D. Pant, D. P. Strik, In situ acetate separation in microbial electrosynthesis from co₂ using ion-exchange resin, *Electrochimica Acta* 237 (2017) 267–275.
- [55] J. Guilera, E. Ramírez, C. Fité, J. Tejero, F. Cunill, Synthesis of ethyl hexyl ether over acidic ion-exchange resins for cleaner diesel fuel, *Catalysis Science & Technology* 5 (4) (2015) 2238–2250.
- [56] G. He, F. Dai, M. Shi, Q. Li, Y. Yu, Hydrolysis of methylal catalyzed by ion exchange resins in aqueous media, *Russian Journal of Physical Chemistry A* 92 (5) (2018) 889–895.

- [57] M. K. Hazra, J. S. Francisco, A. Sinha, Gas phase hydrolysis of formaldehyde to form methanediol: impact of formic acid catalysis, *The Journal of Physical Chemistry A* 117 (46) (2013) 11704–11710.
- [58] D. L. Bartholet, M. A. Arellano-Treviño, F. L. Chan, S. Lucas, J. Zhu, P. C. St. John, T. L. Alleman, C. S. McEnally, L. D. Pfefferle, D. A. Ruddy, B. Windom, T. D. Foust, K. F. Reardon, Property predictions demonstrate that structural diversity can improve the performance of polyoxymethylene ethers as potential bio-based diesel fuels, *Fuel* 295 (2021) 120509.
- [59] M. Ortiz, A. Irabien, Kinetic analysis of liquid-phase depolymerization of trioxane from programmed temperature data, *Journal of thermal analysis* 32 (5) (1987) 1333–1344.
- [60] J. Voggenreiter, A. Ferre, J. Burger, Scale-up of the continuous production of poly (oxymethylene) dimethyl ethers from methanol and formaldehyde in tubular reactors, *Industrial & Engineering Chemistry Research* 61 (28) (2022) 10034–10046.
- [61] I. Agirre, M. Güemez, A. Ugarte, J. Requieres, V. Barrio, J. Cambra, P. Arias, Glycerol acetals as diesel additives: Kinetic study of the reaction between glycerol and acetaldehyde, *Fuel processing technology* 116 (2013) 182–188.
- [62] M. A. Arellano-Treviño, D. Bartholet, A. T. To, A. W. Bartling, F. G. Baddour, T. L. Alleman, E. D. Christensen, G. M. Fioroni, C. Hays, J. Luecke, J. Zhu, C. S. McEnally, L. D. Pfefferle, K. F. Reardon, T. D. Foust, D. A. Ruddy, Synthesis of butyl-exchanged polyoxymethylene ethers as renewable diesel blendstocks with improved fuel properties, *ACS Sustainable Chemistry & Engineering* 9 (18) (2021) 6266–6273.
- [63] P. Kluschke, T. Gnann, P. Plötz, M. Wietschel, Market diffusion of alternative fuels and powertrains in heavy-duty vehicles: A literature review, *Energy Reports* 5 (2019) 1010–1024.

- [64] A. I. Osman, N. Mehta, A. M. Elgarahy, A. Al-Hinai, A. H. Al-Muhtaseb, D. W. Rooney, Conversion of biomass to biofuels and life cycle assessment: a review, *Environmental Chemistry Letters* 19 (6) (2021) 4075–4118.
- [65] M. F. Ibrahim, S. W. Kim, S. Abd-Aziz, Advanced bioprocessing strategies for biobutanol production from biomass, *Renewable and Sustainable Energy Reviews* 91 (2018) 1192–1204.
- [66] A. Pugazhendhi, T. Mathimani, S. Varjani, E. R. Rene, G. Kumar, S.-H. Kim, V. K. Pon-nusamy, J.-J. Yoon, Biobutanol as a promising liquid fuel for the future-recent updates and perspectives, *Fuel* 253 (2019) 637–646.
- [67] D. Parra, J. Izquierdo, F. Cunill, J. Tejero, C. Fite, M. Iborra, M. Vila, Catalytic activity and deactivation of acidic ion-exchange resins in methyl tert-butyl ether liquid-phase synthesis, *Industrial & engineering chemistry research* 37 (9) (1998) 3575–3581.
- [68] M. D. Argyle, C. H. Bartholomew, Heterogeneous catalyst deactivation and regeneration: A review, *Catalysts* 5 (1) (2015) 145–269.
- [69] J. T. Scanlon, D. E. Willis, Calculation of flame ionization detector relative response factors using the effective carbon number concept, *Journal of Chromatographic Science* 23 (8) (1985) 333–340.
- [70] ASTM International, ASTM D8183-18 Standard Test Method for Determination of Indicated Cetane Number (ICN) of Diesel Fuel Oils using a Constant Volume Combustion Chamber—Reference Fuels Calibration Method, 2018.
- [71] Comparing Cetane Number Measurement Methods, Vol. ASME 2020 Internal Combustion Engine Division Fall Technical Conference of Internal Combustion Engine Division Fall Technical Conference, v001T02A009.
- [72] ASTM International, ASTM D240-19 Standard Test Method for Heat of Combustion of Liquid Hydrocarbon Fuels by Bomb Calorimeter, 2019.

- [73] ASTM International, ASTM D93-20 Standard Test Methods for Flash Point by Pensky-Martens Closed Cup Tester, 2020.
- [74] ASTM International, ASTM D7042-21a Standard Test Method for Dynamic Viscosity and Density of Liquids by Stabinger Viscometer (and the Calculation of Kinematic Viscosity), 2021.
- [75] ASTM International, ASTM D6378-20 Standard Test Method for Determination of Vapor Pressure (VPX) of Petroleum Products, Hydrocarbons, and Hydrocarbon-Oxygenate Mixtures (Triple Expansion Method), 2020.
- [76] ASTM International, ASTM D7545-14(2019)e1 Standard Test Method for Oxidation Stability of Middle Distillate Fuels—Rapid Small Scale Oxidation Test (RSSOT), 2019.
- [77] C. S. McEnally, L. D. Pfefferle, Improved sooting tendency measurements for aromatic hydrocarbons and their implications for naphthalene formation pathways, *Combustion and Flame* 148 (4) (2007) 210–222.
- [78] M. J. Montgomery, D. D. Das, C. S. McEnally, L. D. Pfefferle, Analyzing the robustness of the yield sooting index as a measure of sooting tendency, *Proceedings of the Combustion Institute* 37 (1) (2019) 911–918.
- [79] C. S. McEnally, Y. Xuan, P. C. S. John, D. D. Das, A. Jain, S. Kim, T. A. Kwan, L. K. Tan, J. Zhu, L. D. Pfefferle, Sooting tendencies of co-optima test gasolines and their surrogates, *Proceedings of the Combustion Institute* 37 (1) (2019) 961–968.
- [80] J. Zhu, F. L. Chan, T. D. Foust, S. Lucas, L. D. Montgomery, M. J. and Pfefferle, K. F. Reardon, B. C. Windom, C. S. McEnally, Poly(oxymethylene) ethers: Potential diesel fuels with low sooting tendencies, in: *In 2020 AIChE Annual Meeting, Virtual, 2021*, p. 364d, DOI: 10.6084/m9.figshare.13516859.v1.
- [81] R. Stephenson, J. Stuart, M. Tabak, Mutual solubility of water and aliphatic alcohols, *Journal of chemical and engineering data* 29 (3) (1984) 287–290.

- [82] ASTM International, ASTM D1160-18 Standard Test Method for Distillation of Petroleum Products at Reduced Pressure, 2018.
- [83] L. C. Kröger, M. Döntgen, D. Firaha, W. A. Kopp, K. Leonhard, Ab initio kinetics predictions for h-atom abstraction from diethoxymethane by hydrogen, methyl, and ethyl radicals and the subsequent unimolecular reactions, *Proceedings of the Combustion Institute* 37 (1) (2019) 275–282.
- [84] J. Yanowitz, M. A. Ratcliff, R. L. McCormick, J. D. Taylor, M. J. Murphy, Compendium of experimental cetane numbers, Tech. Rep. NREL/TP-5400-67585, National Renewable Energy Laboratory (2017).
- [85] A. Nicolle, N. Naser, T. Javed, N. Rankovic, S. M. Sarathy, Autoignition characteristics of ethers blended with low cetane distillates, *Energy & Fuels* 33 (7) (2019) 6775–6787.
- [86] S. M. Lopes, R. Furey, P. Geng, Calculation of heating value for diesel fuels containing biodiesel, *SAE International Journal of Fuels and Lubricants* 6 (2) (2013) 407–418.
- [87] M. Gülüm, A. Bilgin, Density, flash point and heating value variations of corn oil biodiesel–diesel fuel blends, *Fuel Processing Technology* 134 (2015) 456–464.
- [88] S. Bezergianni, A. Dimitriadis, Comparison between different types of renewable diesel, *Renewable and Sustainable Energy Reviews* 21 (2013) 110–116.
- [89] S. McAllister, J.-Y. Chen, A. C. Fernandez-Pello, *Fundamentals of combustion processes*, Vol. 302, Springer, 2011.
- [90] M. Härtl, P. Seidenspinner, E. Jacob, G. Wachtmeister, Oxygenate screening on a heavy-duty diesel engine and emission characteristics of highly oxygenated oxymethylene ether fuel ome1, *Fuel* 153 (2015) 328–335.

- [91] D. Deutsch, D. Oestreich, L. Lautenschütz, P. Haltenort, U. Arnold, J. Sauer, High purity oligomeric oxymethylene ethers as diesel fuels, *Chemie Ingenieur Technik* 89 (4) (2017) 486–489.
- [92] Y. R. Tan, M. L. Botero, Y. Sheng, J. A. Dreyer, R. Xu, W. Yang, M. Kraft, Sooting characteristics of polyoxymethylene dimethyl ether blends with diesel in a diffusion flame, *Fuel* 224 (2018) 499–506.
- [93] C. H. Cho, K. R. Han, C. H. Sohn, F. M. Haas, Sooting propensity estimation of jet aviation fuel surrogates and their n-alkane components by the virtual smoke point method, *Energy & Fuels* 34 (11) (2020) 15072–15076.
- [94] M. Frenklach, A. M. Mebel, On the mechanism of soot nucleation, *Physical Chemistry Chemical Physics* 22 (9) (2020) 5314–5331.
- [95] J. Zhu, Sooting tendencies and soot formation pathways of alternative fuels and compounds, Ph.D. thesis, Yale University (2023).
- [96] National Fire Protection Association, NFPA 30 Flammable and Combustible Liquids Code, 2020.
- [97] A. H. Lefebvre, V. G. McDonell, *Atomization and sprays*, CRC press, 2017.
- [98] S. J. M. Algayyim, A. P. Wandel, Macroscopic and microscopic characteristics of biofuel spray (biodiesel and alcohols) in ci engines: A review, *Fuel* 292 (2021) 120303.
- [99] J. Hayashi, H. Watanabe, R. Kurose, F. Akamatsu, Effects of fuel droplet size on soot formation in spray flames formed in a laminar counterflow, *Combustion and Flame* 158 (12) (2011) 2559–2568.
- [100] National Institute of Standards and Technology, Methylal phase change data, <https://webbook.nist.gov/cgi/cbook.cgi?ID=C109875&Units=SI&Mask=4#Thermo-Phase>.

- [101] National Institute of Standards and Technology, Methane, diethoxy- phase change data, <https://webbook.nist.gov/cgi/cbook.cgi?ID=C462953&Units=SI&Mask=4#Thermo-Phase>.
- [102] National Institute of Standards and Technology, Heptane phase change data, <https://webbook.nist.gov/cgi/cbook.cgi?ID=C142825&Units=SI&Mask=4#Thermo-Phase>.
- [103] National Institute of Standards and Technology, Decane phase change data, <https://webbook.nist.gov/cgi/cbook.cgi?ID=C124185&Units=SI&Mask=4#Thermo-Phase>.
- [104] National Institute of Standards and Technology, Dodecane phase change data, <https://webbook.nist.gov/cgi/cbook.cgi?ID=C112403&Units=SI&Mask=4#Thermo-Phase>.
- [105] W. W. Focke, I. Van der Westhuizen, X. Oosthuysen, Biodiesel oxidative stability from rancimat data, *Thermochimica Acta* 633 (2016) 116–121.
- [106] M. Alves-Fortunato, A. Baroni, L. Neocel, M. Chardin, M. Matrat, C. Boucaud, M. Mazarin, Gasoline oxidation stability: Deposit formation tendencies evaluated by petrooxy and autoclave methods and gdi/pfi engine tests, *Energy & Fuels* 35 (22) (2021) 18430–18440.
- [107] L. Botella, F. Bimbela, L. Martín, J. Arauzo, J. L. Sánchez, Oxidation stability of biodiesel fuels and blends using the rancimat and petrooxy methods. effect of 4-allyl-2, 6-dimethoxyphenol and catechol as biodiesel additives on oxidation stability, *Frontiers in chemistry* 2 (2014) 43.
- [108] J. Schröder, K. Görsch, Storage stability and material compatibility of poly (oxymethylene) dimethyl ether diesel fuel, *Energy & Fuels* 34 (1) (2019) 450–459.

- [109] M. Kass, M. Wissink, C. Janke, R. Connatser, S. Curran, Compatibility of elastomers with polyoxymethylene dimethyl ethers and blends with diesel, Society of Automotive Engineers Technical Paper Series 1 (01) (2020).
- [110] ASTM International, ASTM D975-21 Standard Specification for Diesel Fuel, 2021.
- [111] C.-J. Sung, H. J. Curran, Using rapid compression machines for chemical kinetics studies, *Progress in Energy and Combustion Science* 44 (2014) 1–18.
- [112] S. S. Goldsborough, S. Hochgreb, G. Vanhove, M. S. Wooldridge, H. J. Curran, C.-J. Sung, Advances in rapid compression machine studies of low-and intermediate-temperature autoignition phenomena, *Progress in Energy and Combustion Science* 63 (2017) 1–78.
- [113] R. K. Hanson, D. F. Davidson, Recent advances in laser absorption and shock tube methods for studies of combustion chemistry, *Progress in Energy and Combustion Science* 44 (2014) 103–114.
- [114] G. Mittal, M. Chaos, C.-J. Sung, F. L. Dryer, Dimethyl ether autoignition in a rapid compression machine: Experiments and chemical kinetic modeling, *Fuel Processing Technology* 89 (12) (2008) 1244–1254, dimethyl Ether Special Section.
- [115] T. X. Phuoc, Laser-induced spark ignition fundamental and applications, *Optics and Lasers in Engineering* 44 (5) (2006) 351–397.
- [116] M. H. Morsy, Review and recent developments of laser ignition for internal combustion engines applications, *Renewable and Sustainable Energy Reviews* 16 (7) (2012) 4849–4875.
- [117] ASTM International, ASTM D2699-22a Standard Test Method for Research Octane Number of Spark-Ignition Engine Fuel, 2022.
- [118] ASTM International, ASTM D2700-22b Standard Test Method for Motor Octane Number of Spark-Ignition Engine Fuel, 2022.

- [119] M. Mehl, W. J. Pitz, C. K. Westbrook, H. J. Curran, Kinetic modeling of gasoline surrogate components and mixtures under engine conditions, *Proceedings of the Combustion Institute* 33 (1) (2011) 193–200.
- [120] N. Li, W. Sun, S. Liu, X. Qin, Y. Zhao, Y. Wei, Y. Zhang, A comprehensive experimental and kinetic modeling study of dimethoxymethane combustion, *Combustion and Flame* 233 (2021) 111583.
- [121] C. W. Gao, J. W. Allen, W. H. Green, R. H. West, Reaction mechanism generator: Automatic construction of chemical kinetic mechanisms, *Computer Physics Communications* 203 (2016) 212–225.
- [122] P. Zhang, I. G. Zsély, V. Samu, T. Nagy, T. Turányi, Comparison of methane combustion mechanisms using shock tube and rapid compression machine ignition delay time measurements, *Energy & Fuels* 35 (15) (2021) 12329–12351.
- [123] S. Wang, D. F. Davidson, R. K. Hanson, Chapter 3 - shock tube techniques for kinetic target data to improve reaction models, in: T. Faravelli, F. Manenti, E. Ranzi (Eds.), *Mathematical Modelling of Gas-Phase Complex Reaction Systems: Pyrolysis and Combustion*, Vol. 45 of *Computer Aided Chemical Engineering*, Elsevier, 2019, pp. 169–202.
- [124] A. Zdanowicz, J. Mohr, J. Tryner, K. Gustafson, B. Windom, D. B. Olsen, G. Hampson, A. J. Marchese, End-gas autoignition fraction and flame propagation rate in laser-ignited primary reference fuel mixtures at elevated temperature and pressure, *Combustion and Flame* 234 (2021) 111661.
- [125] A. P. Kelley, C. K. Law, Nonlinear effects in the extraction of laminar flame speeds from expanding spherical flames, *Combustion and Flame* 156 (9) (2009) 1844–1851.
- [126] A. P. Kelley, W. Liu, Y. Xin, A. Smallbone, C. Law, Laminar flame speeds, non-premixed stagnation ignition, and reduced mechanisms in the oxidation of iso-octane, *Proceedings of the Combustion Institute* 33 (1) (2011) 501–508.

- [127] P. C. S. John, Y. Guan, Y. Kim, S. Kim, R. S. Paton, Prediction of organic homolytic bond dissociation enthalpies at near chemical accuracy with sub-second computational cost, *Nature Communications* 11 (2020) 2328.
- [128] P. C. S. John, Y. Guan, Y. Kim, B. D. Etz, S. Kim, R. S. Paton, Quantum chemical calculations for over 200,000 organic radical species and 40,000 associated closed-shell molecules, *Scientific Data* 7 (2020) 244.
- [129] P. C. St. John, Y. Guan, Y. Kim, B. D. Etz, S. Kim, R. S. Paton. BDE Estimator, available at <http://bde.ml.nrel.gov/> [online].
- [130] C. Zhang, J. He, Y. Li, X. Li, P. Li, Ignition delay times and chemical kinetics of diethoxymethane/o₂/ar mixtures, *Fuel* 154 (2015) 346–351.
- [131] L. Cai, S. Jacobs, R. Langer, F. vom Lehn, K. A. Heufer, H. Pitsch, Auto-ignition of oxymethylene ethers (omen, n = 2–4) as promising synthetic e-fuels from renewable electricity: shock tube experiments and automatic mechanism generation, *Fuel* 264 (2020) 116711.
- [132] M. Mehl, H. J. Curran, W. J. Pitz, C. K. Westbrook, Chemical kinetic modeling of component mixtures relevant to gasoline, in: 4th European Combustion Meeting, 2009.
- [133] J. Würmel, E. Silke, H. Curran, M. Ó Conaire, J. Simmie, The effect of diluent gases on ignition delay times in the shock tube and in the rapid compression machine, *Combustion and Flame* 151 (1) (2007) 289–302.
- [134] J. Ezzell, D. Wilson, C. Allen, On the influence of initial conditions and facility effects on rapid compression machine data, *Fuel* 245 (2019) 368–383.
- [135] S. S. Merchant, C. F. Goldsmith, A. G. Vandeputte, M. P. Burke, S. J. Klippenstein, W. H. Green, Understanding low-temperature first-stage ignition delay: Propane, *Combustion and Flame* 162 (10) (2015) 3658–3673.

- [136] J. Mendes, C.-W. Zhou, H. J. Curran, Rate constant calculations of h-atom abstraction reactions from ethers by ho₂ radicals, *The Journal of Physical Chemistry A* 118 (8) (2014) 1300–1308, PMID: 24483837.
- [137] M. V. Johnson, S. S. Goldsborough, Z. Serinyel, P. O’Toole, E. Larkin, G. O’Malley, H. J. Curran, A shock tube study of n- and iso-propanol ignition, *Energy & Fuels* 23 (12) (2009) 5886–5898.
- [138] X. Guo, R. M. Zhang, L. G. Gao, X. Zhang, X. Xu, Computational kinetics of the hydrogen abstraction reactions of n-propanol and iso-propanol by oh radical, *Phys. Chem. Chem. Phys.* 21 (2019) 24458–24468.
- [139] H. Wei, T. Zhu, G. Shu, L. Tan, Y. Wang, Gasoline engine exhaust gas recirculation—a review, *Applied energy* 99 (2012) 534–544.
- [140] Z. Wang, H. Liu, R. D. Reitz, Knocking combustion in spark-ignition engines, *Progress in Energy and Combustion Science* 61 (2017) 78–112.
- [141] S. P. Lucas, N. J. Labbe, A. J. Marchese, B. Windom, Pre-vaporized ignition behavior of ethyl-and propyl-terminated oxymethylene ethers, *Proceedings of the Combustion Institute* (2022).
- [142] X. Man, C. Tang, J. Zhang, Y. Zhang, L. Pan, Z. Huang, C. K. Law, An experimental and kinetic modeling study of n-propanol and i-propanol ignition at high temperatures, *Combustion and flame* 161 (3) (2014) 644–656.
- [143] S. Jouzdani, A. Zhou, B. Akih-Kumgeh, Propanol isomers: Investigation of ignition and pyrolysis time scales, *Combustion and Flame* 176 (2017) 229–244.
- [144] J. Luecke, M. J. Rahimi, B. T. Zigler, R. W. Grout, Experimental and numerical investigation of the advanced fuel ignition delay analyzer (afida) constant-volume combustion chamber as a research platform for fuel chemical kinetic mechanism validation, *Fuel* 265 (2020) 116929.

- [145] T. Wallner, A. Ickes, K. Lawyer, Analytical assessment of c2–c8 alcohols as spark-ignition engine fuels, in: Proceedings of the FISITA 2012 World Automotive Congress: Volume 3: Future Automotive Powertrains (I), Springer, 2013, pp. 15–26.
- [146] W. R. Leppard, The chemical origin of fuel octane sensitivity, SAE transactions (1990) 862–876.
- [147] J. A. Miller, M. J. Pilling, J. Troe, Unravelling combustion mechanisms through a quantitative understanding of elementary reactions, Proceedings of the Combustion Institute 30 (1) (2005) 43–88.

Appendix A

List of Chemicals Used

This section provides a complete listing of chemicals used, CAS numbers when applicable, and whether they were acquired commercially or synthesized in-house.

Table A.1: Chemicals used in this research

Chemical	CAS #	Composition	Source
M-1-M	109-87-5	C ₃ H ₈ O ₂	Commercial (Fisher and/or Sigma Aldrich)
M-2-M	628-90-0	C ₄ H ₁₀ O ₃	Commercial (Astatech)
M-3-M	13353-03-2	C ₅ H ₁₂ O ₄	Oak Ridge National Lab (purified in-house)
M-4-M	13352-75-5	C ₆ H ₁₄ O ₅	Oak Ridge National Lab (purified in-house)
M-5-M	13352-76-6	C ₇ H ₁₆ O ₆	Oak Ridge National Lab (purified in-house)
E-1-E	462-95-3	C ₅ H ₁₂ O ₂	Commercial (Fisher and/or Sigma Aldrich)
E-2-E	5648-29-3	C ₆ H ₁₄ O ₃	Synthesized in-house
E-3-E	4431-82-7	C ₇ H ₁₆ O ₄	Synthesized in-house
P-1-P	505-84-0	C ₇ H ₁₆ O ₂	Commercial (Lambiotte & Cie)
P-2-P	Not registered	C ₈ H ₁₈ O ₃	Synthesized in-house
P-3-P	4478-22-2	C ₉ H ₂₀ O ₄	Synthesized in-house
B-1-B	2568-90-3	C ₉ H ₂₀ O ₂	Commercial (Lambiotte & Cie) and in-house
B-2-B	Not registered	C ₁₀ H ₂₂ O ₃	Synthesized in-house
B-3-B	Not registered	C ₁₁ H ₂₄ O ₄	Synthesized in-house
iP-1-iP	2568-89-0	C ₇ H ₁₆ O ₂	Synthesized in-house
iB-1-iB	2568-91-4	C ₉ H ₂₀ O ₂	Synthesized in-house
TXN	110-88-3	C ₃ H ₆ O ₃	Commercial (Fisher and/or Sigma Aldrich)
MeOH	67-56-1	CH ₄ O	Commercial (Fisher and/or Sigma Aldrich)
EtOH	64-17-5	C ₂ H ₆ O	Commercial (Fisher and/or Sigma Aldrich)

nPrOH	71-23-8	C ₃ H ₈ O	Commercial (Fisher and/or Sigma Aldrich)
iPrOH	67-63-0	C ₃ H ₈ O	Commercial (Fisher and/or Sigma Aldrich)
nBuOH	71-36-3	C ₄ H ₁₀ O	Commercial (Fisher and/or Sigma Aldrich)
iBuOH	78-83-1	C ₄ H ₁₀ O	Commercial (Gevo)
nPeOH	71-41-0	C ₅ H ₁₂ O	Commercial (Sigma Aldrich)
nC7	142-82-5	C ₇ H ₁₆	Commercial (Fisher and/or Sigma Aldrich)
iC8	540-84-1	C ₈ H ₁₈	Commercial (Fisher and/or Sigma Aldrich)
nC13	629-50-5	C ₁₃ H ₂₈	Commercial (Fisher and/or Sigma Aldrich)
Water	7732-18-5	H ₂ O	Commercial (LabChem) and purified in-house
NaCarb	497-19-8	Na ₂ CO ₃	Commercial (Fisher)
NaBiCarb	144-55-8	Na ₂ HCO ₃	Commercial (Fisher)

Appendix B

Operation of the B/R Instruments Spinning Band

Distillation Column

The B/R spinning band is an extremely useful tool for moderate-scale separation of fuels or chemicals, but it is charitably described as temperamental. This section will be used to provide operating instructions, troubleshooting, and general tips for operation.

Rules and Warnings

These rules are here to protect you and the column.

- DO NOT OPERATE THE COLUMN WITHOUT TRAINING AND/OR SUPERVISION. YOU WILL BREAK SOMETHING AND IT'S \$50K
- Do not perform any distillations without either the stir bar or boiling chips
- If using boiling chips, ensure that they are inert with respect to your compound, i.e. alumina chips can catalyze reactions in mixtures sensitive to acid catalysts
- If using the vacuum, do not run a distillation without the cold trap filled with a solvent and dry ice
- If using cold trap, ensure that fume hood fan is set to medium or maximum setting, and slide gate is open, to exhaust CO₂ from dry ice
- Ensure heating block is unplugged when not in use and immediately after use
- Avoid vacuum pressures below approximately 25 torr, to prevent glassware damage

Startup Procedure

- **Cold Trap Setup**

- Ensure an adequate supply of dry ice is available
- Check that the fume hood fan is on and the slide gate above the cold trap is
- Add alcohol (reagent ethanol or propanol is fine) to the cold trap up to the bottom level of the inlet hose
- Add small pieces of dry ice to the alcohol one at a time. Do not add too quickly or the rapid sublimation will cause the trap to overflow. You have enough when the “boiling” appearance settles to a slow bubble rate and the dry ice remains in the liquid for an extended duration without disappearing

- **Chiller Setup**

- Check chiller coolant level; if low, add a 50/50 mix of distilled water and ethylene glycol
- Power on with the red button on top
- Screen will read “OFF”. Press and hold the OK button to turn on; chiller will start circulating and target its last setpoint
- Set the setpoint with the up and down arrows, OK to change digits, and OK to set the new setpoint
- For most distillations, ideal setpoint is around -5°C to 5°C

- **Column Startup**

- Power on the column with the green power switch
- Controls are in the computer; this will power on with the column
- Open “Distillation”. It will ask for admin permission – allow this or it won’t work
- Column is now ready for use

- **Operations Check**

- Open “Manual Control” screen
- Click the Spinning Band checkbox. Band should activate and spin without excess noise (some noise is always present in a dry column).
- Click through the various receiver advance and retreat boxes; ensure that the receiver selector moves freely
 - * Set Reflux Valve setpoint to 100 and click/unclick the checkbox. The valve should open and close as the box is checked and unchecked.

Performing a Distillation

• Set Up a Procedure

- Open “Run Management”
- Create a new run; often it is easiest to modify an old one
- Set initial temperature ramp parameters. These will control heat rate until the first cut starts, and are based on pot (liquid) temperature, not vapor temperature
- Set the start point for Cut 1. This should be the vapor temperature of the first component.
- Add additional cuts as necessary. Typically, there should be intermediate cuts between targets if there are discrete components (i.e. mix of OMEs - unlike diesel / gasoline)
- End Cut temperature of final cut will be vapor temperature at which the distillation ends.
- Set heat rates and reflux rates of the temperature cuts
 - * Heat rate will typically need to decrease with later cuts, as there is less liquid to absorb the energy

- * Higher numbers in reflux rate increase the duration of reflux valve closure; i.e. a reflux rate of 3 indicates 3 seconds closed, 1 second open. Higher rates will increase purity of each cut but slow the distillation process
- Save the run. If entirely new, use “Create New Runtype”. It is good practice for the procedure name to include the required vacuum pressure
- Note: typically, heat rates between 20%-35% are appropriate for most fuels in this column
- Note: AET tool can be used to calculate desired cut temperatures for a given vacuum pressure

- **Run The Procedure**

- In the “Manual Control” screen, set the receiver selector to the first receiver.
- Set all glassware in place except boiling flask; attach with clamps
- Fill the appropriate boiling flask with the liquid and add a stir bar or boiling chips
- Place the boiling flask in the heating block and cover with insulation donut
- Insert flask thermocouple into well
- Plug in heating block cord
- Place heating block on lift and raise into position
 - * The correct position will be just below the bottom of the column
 - * Set the flask so that there is very slight clearance between the flask opening and the column o-ring; this allows for thermal expansion without stressing the column. The clamp will hold the flask in place as it heats
 - * Note: It is best to plug in the cord before you clamp the flask, so you do not put horizontal pressure on the base of the column
- Turn on stirrer to a minimum of 30 on the dial and verify the stir bars spins and is not hitting the thermocouple well

- Turn on vacuum controller (do not turn on pump yet)
 - * Set to Auto
 - * Enter a test pressure and hit Enter; this will typically be at least 100 torr higher than the target pressure
 - * Test pressure is to verify that everything is sealed and avoid flash boiling
- Turn on vacuum pump – pressure should decrease to setpoint and hold
 - * If valve is rapidly opening and closing, or cannot reach the setpoint, there is a leak. Check clamps, o-rings, and bleed valves
- Select “Run Method”
 - * Select the procedure you have created
 - * The software will walk through some safety checks. Pay attention to all of these.
 - * After safety checks, give file a name for future review
 - * Run the method
- On the vacuum controller, set the actual target pressure and hit Enter. Make sure there is no flash boiling at the target pressure
- Observe the column and liquid throughout the process. It should run itself, however, some manual intervention may be required.
 - * If a receiver is about to overflow before the end of a cut, the arrow button on the schematic screen will advance manually.
 - * If liquid is boiling too quickly and overflowing the cooling section or reflux valve section, decrease the heat rate and/or decrease the reflux ratio
 - * If run parameters need to be modified on the fly, change them in the Run Parameters screen (hitting Enter on the keyboard after each entry - this is important), then hit the Change button at the top
- If a short pause is needed, Pause Run will cut the heater off and turn off the band. This is not intended for more than a minute or so of break; if more time is needed,

you may need to abort, since the temperature in the heating block will continue to heat the liquid

- If the method reaches its end, it will stop itself. If you must manually stop, hit Abort Run
 - * After the method ends (automatic or aborted), immediately shut down the vacuum pump
 - * Lower the heating block slightly (to avoid horizontal stress on the column), then unplug the heating block. This is important; under some circumstances (it's not clear exactly why), the heater sometimes gets set to 1 rather than 0 (full power) when the method stops. This is a rare error but has happened occasionally and can cause serious problems.
 - * Use the bleed valve to return the column to atmospheric pressure
- Let the liquids cool, then empty and clean the receivers and flasks as needed

Shutdown Procedure

- Remove and clean flasks and receivers
- Dispose of waste from cold trap if necessary
- Close all software in the computer
- Shut down the computer with the proper Windows procedure
- After the computer is completely shut down, wait 10 seconds, then power down the column with the green switch. DO NOT use the green switch until the computer is properly and completely shut down.
- Power off the vacuum controller
- Power off the chiller. The red power switch can be used directly for this